



Johannes Nokelainen

# INTERPLAY OF LOCAL MOMENTS AND ITINERANT ELECTRONS



Johannes Nokelainen

## **INTERPLAY OF LOCAL MOMENTS AND ITINERANT ELECTRONS**

Dissertation for the degree of Doctor of Science (Technology) to be presented with due permission for public examination and criticism in the Auditorium 2310 at Lappeenranta-Lahti University of Technology LUT, Lappeenranta, Finland on the 2<sup>nd</sup> of October, 2020, at 15:00.

Acta Universitatis  
Lappeenrantaensis 919

Supervisors Associate professor Katariina Pussi  
LUT School of Engineering Science  
Lappeenranta-Lahti University of Technology LUT  
Finland

Professor Bernardo Barbiellini  
LUT School of Engineering Science  
Lappeenranta-Lahti University of Technology LUT  
Finland

Reviewers Docent Dr. Jouko Nieminen  
Department of Physics  
Tampere University  
Finland

Academy Research Fellow Dr. Ilja Makkonen  
Department of Physics  
University of Helsinki  
Finland

Opponent Professor Gregory Fiete  
Department of Physics  
Northeastern University (Boston)  
Massachusetts (USA)

ISBN 978-952-335-545-3  
ISBN 978-952-335-546-0 (PDF)  
ISSN-L 1456-4491  
ISSN 1456-4491

Lappeenranta-Lahti University of Technology LUT  
LUT University Press 2020

## **Abstract**

**Johannes Nokelainen**  
**Interplay of Local Moments and Itinerant Electrons**

Lappeenranta 2020

60 pages

Acta Universitatis Lappeenrantaensis 919

Diss. Lappeenranta-Lahti University of Technology LUT

ISBN 978-952-335-545-3, ISBN 978-952-335-546-0 (PDF),

ISSN-L 1456-4491, ISSN 1456-4491

We have studied the electronic structure of materials whose properties are driven by magnetism. This work requires research with computer simulations based on quantum mechanics laws within the density functional theory aimed to predict and to understand their complex phase diagrams with a high degree of accuracy and reliability. The applications that can emerge from our studies yield a great technological potential. Our objective is to enable technology breakthroughs that lead to changes in paradigm in novel functional materials and in quantum technologies, where quantum behavior can be controlled by using heterostructures of superconductors with magnets, insulators, semiconductors and metals.

Keywords: density-functional theory, first principles calculations, magnetism, spintronics, graphene, Heusler compounds, high-temperature superconductivity



## Acknowledgements

This work was carried out in the department of Physics at Lappeenranta-Lahti University of Technology LUT, Finland, between 2015 and 2020. First of all, thank you Prof. Katariina Pussi for introducing me to your group and for being my first supervisor. Also thank you Aki and everyone else at LUT for your company and help. During this project, I had the privilege of briefly working with Prof. Arun Bansil's group in the Northeastern University, Boston, as well as attending numerous online meetings with all of you. Thank you for help and particularly for introducing me to the field of high-temperature superconductors. Sooner or later, see you again in the same circumstances. I would like to thank Prof. Jouko Nieminen and Dr. Ilja Makkonen for your throughout efforts in the review process, which greatly improved the manuscript. Of course I would like to thank you for my family and friends for all of your support. Finally, I would like to express my gratitude to my colleague, friend and the second supervisor Bernardo. Your endless helpfulness surpassed all the requirements demanded by your role, whether it was about research, this thesis, grant applications or planning my future career. I also want to thank the Academy of Finland, Finnish Cultural Foundation and the LUT Doctoral School for financial support and the Center of Scientific Computing for the computational resources.

*Johannes Nokelainen*  
September 2020  
Lappeenranta



# CONTENTS

<b>Abstract</b>	
<b>Acknowledgements</b>	
<b>Contents</b>	
<b>List of publications</b>	<b>9</b>
<b>Nomenclature</b>	<b>11</b>
<b>1 Introduction</b>	<b>13</b>
1.1 Background . . . . .	13
1.1.1 The Physics of magnetism . . . . .	13
1.1.2 First-principles computations . . . . .	13
1.2 Objective of the work . . . . .	14
1.2.1 Spintronics in two-dimensional materials . . . . .	14
1.2.2 Exploration of Mn-rich Heusler compounds . . . . .	15
1.2.3 Study of competing phases of high-temperature superconductors . . . . .	15
<b>2 Density functional theory</b>	<b>17</b>
2.1 The quantum many-body problem . . . . .	17
2.1.1 The Hohenberg-Kohn theorems . . . . .	18
2.1.2 The Kohn-Sham construction . . . . .	19
2.1.3 The exchange-correlation energy . . . . .	20
2.1.4 The Kohn-Sham equations . . . . .	20
2.1.5 Solving the Kohn-Sham equations . . . . .	21
2.1.6 The pseudopotential approach . . . . .	22
2.1.7 The spin-orbit interaction . . . . .	23
2.2 The exchange-correlation functionals . . . . .	23
2.2.1 Jabob's ladder of density functional approximations . . . . .	23
2.2.2 The strongly constrained and appropriately normed meta-generalized gradient approximation . . . . .	24
2.2.3 On-site Coulomb interactions . . . . .	25
<b>3 Gate-tunable magnetism on graphene</b>	<b>27</b>
3.1 Introduction . . . . .	27
3.2 Theoretical considerations . . . . .	27
3.3 One carbon adatom per unit cell . . . . .	28
3.4 Interactions between adatoms . . . . .	30

3.4.1	Energetics of two-adatom configurations . . . . .	31
3.4.2	Magnetic interactions of adatoms under gate voltage . . . . .	32
3.5	Conclusion . . . . .	34
<b>4</b>	<b>Correlation in elemental manganese</b>	<b>37</b>
4.1	Introduction . . . . .	37
4.2	Results . . . . .	37
4.2.1	Mn dimer . . . . .	38
4.2.2	$\gamma$ -Mn . . . . .	39
4.2.3	Noncollinear antiferromagnetic $\alpha$ -Mn . . . . .	39
4.3	Conclusion . . . . .	42
<b>5</b>	<b>Correlation in a high-temperature superconductor</b>	<b>45</b>
5.1	Introduction . . . . .	45
5.2	Results . . . . .	46
5.2.1	Pristine Bi2201 and Bi2212 . . . . .	46
5.2.2	Doping of Bi2212 . . . . .	49
5.3	Conclusion . . . . .	52
<b>6</b>	<b>Conclusion and Outlook</b>	<b>53</b>
	<b>References</b>	<b>60</b>
	<b>Publications</b>	

## List of publications

This thesis consists of an introductory part and three original, refereed articles in scientific journals. The articles and the author's contribution in them are summarized below.

- I J. Nokelainen, I. V. Rozhansky, B. Barbiellini, E. Lähderanta and K. Pussi.** Gate-tunable magnetism of C adatoms on graphene, *Physical Review B*, **99**, pp. 035441, 2019.
- II A. Pulkkinen, B. Barbiellini, J. Nokelainen, V. Sokolovskiy, D. Baigutlin, O. Miroshkina, M. Zagrebin, V. Buchelnikov, C. Lane, R. S. Markiewicz, A. Bansil, J. Sun, K. Pussi and E. Lähderanta.** Coulomb correlation in noncollinear antiferromagnetic  $\alpha$ -Mn, *Physical Review B*, **101**, pp. 075115, 2020.
- III J. Nokelainen, C. Lane, R. S. Markiewicz, B. Barbiellini, A. Pulkkinen, B. Singh, J. Sun, K. Pussi and A. Bansil.** *Ab initio* description of the  $\text{Bi}_2\text{Sr}_2\text{CaCu}_2\text{O}_{8+\delta}$  electronic structure, *Physical Review B*, **101**, pp. 214523, 2020.

Johannes Nokelainen is the principal author of Publications I and III where he has performed all the DFT calculations and done major parts of the result analysis and writing. In Publication II he has calculated and analyzed some of the DFT results and participated in writing.



## Nomenclature

### Symbols

$e$	elementary charge
$E$	energy
$\hat{H}$	Hamiltonian
$J$	On-site exchange
$J_H$	Hund's splitting
$\mathbf{k}$	reciprocal lattice vector
$n$	electron density
$M$	magnetic moment
$Q$	electric charge
$\mathbf{r}, \mathbf{R}$	position
$R_{\text{ws}}$	Wigner-Seitz radius
$T_c$	critical superconducting temperature
$U$	Coulomb on-site correlation
$V$	potential
$V_g$	gate voltage
$\psi, \Psi$	wavefunction

### Acronyms

AFM	antiferromagnetic
ARPES	angle-resolved photoemission spectroscopy
Bi2201	$\text{Bi}_2\text{Sr}_2\text{CuO}_6$
Bi2212	$\text{Bi}_2\text{Sr}_2\text{CaCu}_2\text{O}_8$
BSCCO	Bi-Sr-Ca-Cu-O cuprate superconductor family
BZ	Brillouin zone
DFT	density functional theory
DOS	density of states
FM	ferromagnetic
GGA	generalized gradient approximation
HK	Hohenberg-Kohn
KS	Kohn-Sham
LDA	local density approximation
KED	kinetic energy density
SC	supercell
SCAN	strongly constrained and appropriately normed
SOC	spin-orbit coupling
PAW	projector augmented wave
PBE	Perdew, Burke, and Ernzerhof
RIXS	resonant inelastic X-ray spectroscopy
STM	scanning tunnelling microscopy
vdW	van der Waals
VASP	Vienna ab-initio simulation package
XC	exchange-correlation



# INTRODUCTION

## 1.1 Background

### 1.1.1 The Physics of magnetism

The spin of the electron, which can be visualized as the quantum-mechanical analogue of angular momentum of a spinning top, is the key constituent of magnetism. Each electron generates a magnetic field but most materials are non-magnetic because typically an equal amount of electrons with a given spin direction cancels the other contribution with opposite magnetic field. In magnetic materials, there is an unbalance between the internal magnetic fields. This polarization stems from quantum-mechanical interactions of the electrons, which can be divided into *exchange* and *Coulomb correlation* parts [1]. The exchange interaction is related to the Pauli exclusion principle, which states that two electrons with parallel spins can not occupy the same state, and it contributes to delocalization of the electrons. The correlation interaction can be described as an ability of collective movement of the electrons to screen the repulsive electron-electron Coulomb interactions. Exchange and correlation lead to two different mechanisms of magnetism: (1) Exchange drives the spin polarization of *itinerant* (delocalized) electrons in certain materials such as iron, leading to magnetization within the *Stoner model of ferromagnetism*. (2) Coulomb correlation enables increased localization of the electrons around the nuclei, and according to the *Heisenberg model* and the *Hund's rules* the atoms develop localized magnetic moments in systems such as transition metal impurities. However, for real magnetic materials, neither description turns out to be entirely applicable and magnetism falls somewhere on a spectrum between these two extremes. In fact, the resulting frustration of different kind of magnetic interactions often yields particularly interesting physical systems enabling novel smart materials needed in several fields of technology and engineering.

### 1.1.2 First-principles computations

Material science is in the middle of a revolution. A century of progress in physics and computing can be used to discover functional materials. The exponential growth of computer power together with the theoretical effort initiated by Walter Kohn and his co-workers, who developed practicable but accurate solutions to the equations

of quantum mechanics, has made it possible to design materials from scratch using supercomputers and first-principles law of physics. Interestingly, the density functional theory (DFT) formulated by Walter Kohn [2] has evolved from an ingenious idea into the most-widely used tool for predicting structures and electronic, optical, magnetic, and mechanical properties of materials. While DFT is in principle an exact theory, various approximations must be used to perform simulations. The only approximation in DFT is the choice of the exchange-correlation (XC) energy  $E_{xc}$  describing the quantum-mechanical entanglement between the electrons. The energy  $E_{xc}$  can be approximated with different levels of complexity. More advanced  $E_{xc}$  functionals usually bring higher accuracy, but also higher computational cost. The simplest  $E_{xc}$  approximations are local spin density approximation (LSDA) and the generalized gradient approximation (GGA) [3]. Both LSDA and GGA methods fail in describing correlation effects such as the metal-insulator transition in materials where the on-site repulsion energy plays an important role. The strongly constrained and appropriately normed (SCAN) method [4] cures many of these problems while maintaining the computational cost. The application of the SCAN to several materials is one of the key points of the present work.

## 1.2 Objective of the work

The overall goal of this work is to explore the *interplay of local moments and itinerant electrons* using DFT simulations particularly with SCAN in order to foster innovative solutions for new functional materials.

### 1.2.1 Spintronics in two-dimensional materials

The very recent, long-awaited realization of two-dimensional (2D) or atomically thin crystals with intrinsic magnetism has set off immediate and global excitement regarding prospects for new applications as well as for new fundamental understanding of nature in the quantum realm [5]. A promising route for such purpose is graphene modified by magnetic defects. In these systems the spin polarization of the defects “leaks” into the graphene sheet, and the resulting magnetic states are *in between localized and itinerant*, in accordance with the main theme of my thesis. The interactions between the magnetic defects can be either ferromagnetic (FM) or antiferromagnetic (AFM). In the case of FM coupling the magnetic moments point to the same direction, creating a net magnetic moment, whereas in the case of AFM coupling they prefer to align in opposite directions, canceling the net magnetization. Our work on this subject shows the possibility of controlling these magnetic interactions with an external gate voltage, which is one step towards the realization of a new type of a spin-field-effect transistor in which both switching and reversal of spin polarization can be realized by using gate voltage as an external knob [5]. Our work has been recently recognized in a review article by Shukla [6]. Moreover, by using the idea of tuning magnetic interactions by gate voltage, Deng *et al.* have

recently experimentally observed gate-tunable room-temperature ferromagnetism in  $\text{Fe}_3\text{GeTe}_2$  [7].

### 1.2.2 Exploration of Mn-rich Heusler compounds

Heusler alloys are magnetic compositions of the form  $X_2YZ$ , where  $X$  and  $Y$  are transition metals and  $Z$  belongs to the  $p$ -block, with the face-centered cubic crystal structure. Recently, our comparisons between GGA and SCAN for different ternary Heusler Mn alloys [8] has shown that the corrections beyond GGA are significant particularly in the case of Mn-rich compounds such as  $\text{Ni}_2\text{MnGa}$ . These results can be explained by sketching the  $3d$  manganese electrons as magnetic impurities interacting with other itinerant electrons. In order to understand the role of correlation of the Mn-rich compounds and interactions between the localized magnetic  $3d$  states on the Mn atoms, we have turned our attention on pure manganese, which is a particularly complex metallic element [9–15] with a landscape of stable crystal phases at different temperatures. Understanding the case of elemental Mn

### 1.2.3 Study of competing phases of high-temperature superconductors

In high temperature superconductors the coupling between the copper spins and the itinerant electrons in the oxygen orbitals lead to similar paradigms as in the previous cases, nevertheless the situation becomes more complex because the appearance of the superconducting state competing with many other states. Superconductivity at 4.2 kelvins has been known already since 1911, when Heike Onnes discovered it. Realization of superconductivity in room temperature is one of the most long-sought accomplishments in physics since the electric power transmission would be revolutionized. An important step towards this goal was the finding of ceramic cuprate superconductors in 1986, which extended the temperature range about 100 degrees higher. However, the theoretical description of the cuprate superconductivity is still a great puzzle. Traditionally it has been thought that superconductivity does not coexist with magnetism. An interesting novel idea is that the high-temperature cuprate superconductivity could be fundamentally related to magnetic fluctuation of the copper spins. Indeed, our simulations with the SCAN functional for bismuth-based  $\text{Bi}_2\text{Sr}_2\text{Ca}_{n-1}\text{Cu}_n\text{O}_{2n+4+x}$  (BSCCO) cuprate have shown that the copper atoms retain their magnetic moments when the material becomes superconducting. Our findings confirm the new understanding of superconductivity in copper oxides. The manipulation of spin interactions might also bring high-temperature superconductors into technology. For example, since BSCCO has extremely rich phase diagram featuring several regions with different magnetic and electronic properties, external gate voltage can be also applied to a BSCCO sample to control the different states in the phase diagram [16]. This methodology could enable a new generation of applications of superconductivity for quantum information devices by controlling superconducting parameters at the nanoscale.



# DENSITY FUNCTIONAL THEORY

In this Chapter, I discuss the fundamentals of the density-functional theory. I also review some details of implementation of DFT in the Vienna ab initio simulation package (VASP) [17, 18], which I have used for all the simulations in this Thesis.

## 2.1 The quantum many-body problem

At a fundamental level, all the basic properties of ordinary matter are a consequence of quantum mechanics in a system of electrons in a network of atomic nuclei. The quantum-mechanical wavefunction of such system depends on the positions and spins of all electrons and nuclei. However, since the mass of the nuclei is three orders of magnitude larger than those of the electrons, the nuclei are well-localized compared to the electrons. Therefore, the nuclei can be approximated as stationary classical particles that interact with the electrons only by the Coulomb force. In this approximation, the wavefunction of a  $N$ -electron system reads  $\Psi(\mathbf{x}_1, \dots, \mathbf{x}_N)$ , where  $\mathbf{x}_i$  denotes the position-spin pair  $\mathbf{x}_i = (\mathbf{r}_i, \sigma_i)$  of an individual electron.  $\Psi$  must fulfill the energy eigenvalue equation known as the *Schrödinger equation* [19]

$$\hat{H} |\Psi(\mathbf{x}_1, \dots, \mathbf{x}_N)\rangle = E |\Psi(\mathbf{x}_1, \dots, \mathbf{x}_N)\rangle, \quad (2.1)$$

$$\hat{H} = \hat{T} + \hat{V} + \hat{W}. \quad (2.2)$$

$\hat{H}$  is the *Hamiltonian* of a stationary many-body system, and it extracts the energy eigenvalue  $E$  from  $\Psi$ .  $\hat{H}$  is a sum of the *kinetic energy* of the electrons  $\hat{T}$ , the *external potential*  $\hat{V}$  and the *many-body potential*  $\hat{W}$ .  $\hat{V}$  contains the attractive Coulombic potential of the atomic nuclei and  $\hat{W}$  is composed of the Coulombic electron-electron interaction as well as more complex quantum-mechanical many-body interactions. The kinetic energy and the external potential are not spin-dependent, but the many-body potential is. For simplicity we now only consider the spatial degree of freedom and omit the spin notation;  $\mathbf{x} \rightarrow \mathbf{r}$ . The spin-dependence can be reintroduced where necessary.

### 2.1.1 The Hohenberg-Kohn theorems

The electron charge density of  $\Psi$  reads

$$n(\mathbf{r}) = N \int |\Psi(\mathbf{r}, \mathbf{r}_2, \dots, \mathbf{r}_N)|^2 d\mathbf{r}_2 \dots d\mathbf{r}_N. \quad (2.3)$$

The core of the density functional theory lies in two simple but remarkable *Hohenberg-Kohn* (HK) theorems, which uniquely relate this density to a single-particle potential  $V$  for any non-degenerate multi-particle ground state  $\Psi$ :

1. “*The ground state of any interacting many particle system with a given fixed inter-particle interaction is a unique functional of the electron density  $n(r)$* ”
2. “*The electron density that minimizes the energy of the overall functional is the true electron density corresponding to the full solutions of the Schrödinger equation*”

— Pierre Hohenberg and Walter Kohn, 1964 [20]

The first HK theorem is readily shown. As a counterexample, consider another Hamiltonian  $\hat{H}'$  (with energy  $E'$ ), which differs from the original Hamiltonian in by having different external potential;  $\hat{H} = \hat{T} + \hat{V} + \hat{W}$ , but yields the same ground state wavefunction  $\Psi$ . The subtraction of  $\hat{H}'$  from  $\hat{H}$  yields  $(\hat{V} - \hat{V}')|\Psi\rangle = (E - E')|\Psi\rangle$ . In other words, this is possible only if the potentials  $\hat{V}$  and  $\hat{V}'$  differ from each other only by a number  $(E - E')$ , but physically such potentials are equivalent. Therefore, the first Hohenberg-Kohn theorem has been proven by contradiction.

Also the second HK theorem can be justified straightforwardly. If there were two ground state wave functions  $|\Psi\rangle$  and  $|\Psi'\rangle$  that produced the same ground state density  $n(\mathbf{r})$ , then it would hold that

$$\begin{aligned} E &= \langle \Psi | \hat{H} | \Psi \rangle = \langle \Psi | \hat{H}' + \hat{V} - \hat{V}' | \Psi \rangle = \langle \Psi | \hat{H}' | \Psi \rangle + \int d\mathbf{r} n(\mathbf{r}) [\hat{V}(\mathbf{r}) - \hat{V}'(\mathbf{r})] \\ &> E' + \int d^3\mathbf{r} n(\mathbf{r}) [\hat{V}(\mathbf{r}) - \hat{V}'(\mathbf{r})], \end{aligned} \quad (2.4)$$

where one uses the fact that  $\langle \Psi | \hat{H}' | \Psi \rangle > E'$ , since  $\Psi$  is not the ground state wave function for  $\hat{H}'$ . Similarly,  $E_2 > E_1 + \int d^3\mathbf{r} n(\mathbf{r}) [\hat{V}_2(\mathbf{r}) - \hat{V}_1(\mathbf{r})]$ , and combining these two equations results in the contradiction  $E_1 + E_2 > E_1 + E_2$ . Therefore, also the second HK theorem holds. Theorems 1 and 2 form the final HK theorem:

“*The external potential  $V(\mathbf{r})$  is a unique functional of the ground state density  $n(\mathbf{r})$  and vice versa.*”

A straightforward consequence of this statement is that the ground state energy also has unique one-to-one correspondence with the ground state density, i.e., the energy is a *functional* of the ground state density;  $E = E[n(\mathbf{r})]$ . It is clear that the ground

state density  $n(\mathbf{r})$  minimizes  $E[n(\mathbf{r})]$  because of the unique relation between the ground state wavefunction and density. In this way, the  $N$ -body problem has been reduced to the determination of a three-dimensional function  $n(r)$  that minimizes the functional  $E[n(\mathbf{r})]$ . We can therefore write

$$E[n(\mathbf{r})] = \langle \Psi | \hat{T} + \hat{V} + \hat{W} | \Psi \rangle = F[n(\mathbf{r})] + \int d\mathbf{r} n(\mathbf{r}) V(\mathbf{r}), \quad (2.5)$$

$$F[n(\mathbf{r})] = \langle \Psi | \hat{T} + \hat{W} | \Psi \rangle, \quad (2.6)$$

where  $F[n]$  is an universal functional of density, but its exact mathematical form is highly nontrivial.

### 2.1.2 The Kohn-Sham construction

According to the Hohenberg-Kohn theorem condition, the ground state density is  $V$ -representable, which means that for fixed  $\hat{W}$ , each  $n(\mathbf{r})$  is characterized by an unique *single-particle* potential  $V_s(\mathbf{r})$  [21]. We consider now a Hamiltonian  $\hat{H}_s$  for which  $\hat{W} = 0$ , i.e., an auxiliary system of electron gas that is non-interacting except via the Pauli exclusion principle. Even in this case, all the possible electron densities are ground states for some  $V_s(\mathbf{r})$ . Since the particles are non-interacting, it is possible to separate the wavefunction  $|\Psi(\mathbf{r}_1, \dots, \mathbf{r}_N)\rangle$  into a Slater determinant of single-particle orbitals  $\psi_i(\mathbf{r})$  known as *Kohn-Sham orbitals* (KS orbitals), and the density of the system is simply given by a sum of their individual densities:

$$\Psi(\mathbf{r}_1, \dots, \mathbf{r}_N) = \begin{vmatrix} \psi_1(\mathbf{r}_1) & \dots & \psi_N(\mathbf{r}_1) \\ \vdots & \ddots & \vdots \\ \psi_1(\mathbf{r}_N) & \dots & \psi_N(\mathbf{r}_N) \end{vmatrix}, \quad (2.7)$$

$$\hat{H}_s(\mathbf{r}) |\psi_i(\mathbf{r})\rangle = \left[ -\frac{1}{2} \nabla_{\mathbf{r}}^2 + V_s(\mathbf{r}) \right] |\psi_i(\mathbf{r})\rangle = \epsilon_i |\psi_i(\mathbf{r})\rangle, \quad (2.8)$$

$$n(\mathbf{r}) = \sum_i^N \int d\mathbf{r} |\psi_i(\mathbf{r})|^2. \quad (2.9)$$

The above scheme, where the summation goes over  $N$  lowest-energy states, is known as the *Kohn-Sham construction*, and is the heart of the DFT. We will now discuss implementations to solving these equations. It is convenient to divide the energy functional into following parts:

$$\begin{aligned} E[n(\mathbf{r})] &= T_s[n(\mathbf{r})] + F_s[n(\mathbf{r})] \\ &= T_s[n(\mathbf{r})] + \int d\mathbf{r} V[n(\mathbf{r})]n(\mathbf{r}) + E_H[n(\mathbf{r})] + E_{xc}[n(\mathbf{r})], \end{aligned} \quad (2.10)$$

$$T_s[n(\mathbf{r})] = -\frac{1}{2} \sum_i \int d\mathbf{r} \psi_i^*(\mathbf{r}) \nabla^2 \psi_i(\mathbf{r}) \quad \text{and} \quad (2.11)$$

$$E_H[n(\mathbf{r})] = \frac{1}{2} \iint d\mathbf{r} d\mathbf{r}' \frac{n(\mathbf{r})n(\mathbf{r}')}{|\mathbf{r} - \mathbf{r}'|}. \quad (2.12)$$

In this energy partition,  $T_s[n(\mathbf{r})]$  is the kinetic energy of the free electron gas, which is not the same as the kinetic energy of the real interacting system, but in non-correlated cases roughly similar in magnitude. The rest of the energy functional,  $F_s[n(\mathbf{r})]$ , incorporates all the interactions, including the complex many-body effects. First of all,  $F_s[n]$  contains the potential energy from the original Hamiltonian and the Hartree energy  $E_H$ , which describes the classical electrostatic repulsion of the averaged charge cloud  $n(\mathbf{r})$  with itself. In the expression of  $E_H$ , the factor of 1/2 is to avoid the effect of double-counting.

### 2.1.3 The exchange-correlation energy

The last term in Eq. (2.10) is the *exchange-correlation energy*  $E_{xc}[n(\mathbf{r})]$ . It is the term that contains all the complex many-body effects arising from the many-body kinetic energy  $\hat{T}$  and many-body interaction  $\hat{W}$  terms. The exchange energy  $E_x$  describes the difference between the many-body repulsion and the classical repulsion, and it can be written down explicitly as the Hartree-Fock exact exchange functional:

$$E_x^{\text{HF}} = -\frac{1}{2} \sum_{i,j} \int_{\mathbf{r},\mathbf{r}'} \psi_i^*(\mathbf{r})\psi_j^*(\mathbf{r}') \frac{1}{|\mathbf{r}-\mathbf{r}'|} \psi_i(\mathbf{r}')\psi_j(\mathbf{r}). \quad (2.13)$$

$E_x$  stems from the antisymmetry requirement of the wave function of electrons (fermions) with respect to *exchange* of two particle indices. This requirement leads to the *Pauli exclusion principle*, which states that two electrons can not occupy the same state, and in general to the effect of *Pauli repulsion*, which is a repulsive force between electrons with parallel spins.

The *correlation* term is what is left when the  $E_x$  above is subtracted from  $E_{xc}$ . The correlation energy contains the difference between the many-body kinetic energy of the real many-body wavefunction and the single-particle kinetic energy of the KS orbitals. The correlation energy can be described as the collective ability of motion of electrons to screen and decrease the classical Coulomb interaction, hence it is also known as the *Coulomb correlation*.

### 2.1.4 The Kohn-Sham equations

The ground state of the Kohn-Sham construction can be found by determining the minimum of the energy functional Eq. 2.11. Typically, in order to achieve this, the functional derivative of  $E[n]$  with respect to density is studied. However, this procedure ignores some higher-order terms, which will be relevant for this thesis. Therefore, consider an arbitrary orthonormality-satisfying variation of  $\psi_i(\mathbf{r})$ , for which the variation in energy must vanish. The Lagrange variational principle gives

$$E' = E - \sum_{ij} \lambda_{ij} \left( \int \psi_i^*(\mathbf{r})\psi_j(\mathbf{r}) \, d\mathbf{r} - \delta_{ij} \right), \quad (2.14)$$

$$\frac{\delta E'}{\delta \psi_i(\mathbf{r})} = \frac{\delta E'}{\delta \psi_i^*(\mathbf{r})} = 0. \quad (2.15)$$

Multiplying the both sides by  $\psi_k^*$  and integrating yields the Lagrange multipliers  $\lambda_{ij}$ , and we obtain [19, 22]

$$\hat{H}_s \psi_i(\mathbf{r}) = \left[ -\frac{1}{2} \nabla_{\mathbf{r}}^2 + V_H(\mathbf{r}) + V_{\text{ext}}(\mathbf{r}) \right] \psi_i(\mathbf{r}) + \frac{\delta E_{\text{xc}}}{\delta \psi_i^*(\mathbf{r})} = \epsilon_i \psi_i(\mathbf{r}) \quad (2.16)$$

$$V_H(\mathbf{r}) = \int d\mathbf{r}' \frac{n(\mathbf{r}')}{|\mathbf{r} - \mathbf{r}'|} \quad \text{and} \quad (2.17)$$

Above  $V_H(\mathbf{r})$  is the *Hartree potential*, and the single-particle KS Hamiltonian is related to the functional derivative of the energy by the following functional derivative:

$$\frac{\delta E}{\delta \psi_i^*(\mathbf{r})} = \hat{H}_s \psi_i(\mathbf{r}). \quad (2.18)$$

If  $E_{\text{xc}}$  only depends on the density of gradient of density, this equation yields

$$\hat{H}_s \psi_i(\mathbf{r}) = \left[ -\frac{1}{2} \nabla_{\mathbf{r}}^2 + V_H(\mathbf{r}) + V_{\text{xc}}(\mathbf{r}) + V_{\text{ext}}(\mathbf{r}) \right] \psi_i(\mathbf{r}) = \epsilon_i \psi_i(\mathbf{r}), \quad (2.19)$$

$$V_{\text{xc}}(\mathbf{r}) = \frac{\delta E_{\text{xc}}[n(\mathbf{r})]}{\delta n(\mathbf{r})}, \quad (2.20)$$

where  $V_{\text{xc}}(\mathbf{r})$  is the *exchange-correlation potential*. Eq. (2.19) is the most well-known form of the KS equations and it is being employed in the majority of the DFT simulations. However, the general form of the KS equations is more complex than in Eq. (2.19). If no approximations are considered, differentiating Eq. (2.18) with the functional chain rule leads to the following form of the KS equations [22]:

$$\begin{aligned} \hat{H}_s \psi_i(\mathbf{r}) &= \left[ -\frac{1}{2} \nabla_{\mathbf{r}}^2 + V_H(\mathbf{r}) + V_{\text{ext}}(\mathbf{r}) + n(\mathbf{r}) \frac{\partial \varepsilon_{\text{xc}}}{\partial n}(\mathbf{r}) - \nabla \cdot n(\mathbf{r}) \frac{\partial \varepsilon_{\text{xc}}}{\partial \nabla n} \right] \psi_i(\mathbf{r}) \\ &\quad - \frac{1}{2} \nabla \cdot [V_{\tau}(\mathbf{r}) \nabla \psi_i(\mathbf{r})] = \epsilon_i \psi_i(\mathbf{r}), \end{aligned} \quad (2.21)$$

$$\tau(\mathbf{r}) = \sum_i^{\text{occ}} \frac{1}{2} |\nabla \psi_i(\mathbf{r})|^2, \quad (2.22)$$

$$V_{\tau}(\mathbf{r}) = \frac{\partial}{\partial \tau} n(\mathbf{r}) \varepsilon_{\text{xc}}(\mathbf{r}). \quad (2.23)$$

These generalized KS equations also involve the *Kinetic Energy Density* (KED)  $\tau(\mathbf{r})$  as well as the KED potential  $V_{\tau}(\mathbf{r})$ . These quantities contain information about the Coulomb correlation, allowing increased accuracy in the description of strongly correlated materials.

### 2.1.5 Solving the Kohn-Sham equations

The solution for the KS scheme is obtained in a *self-consistent* manner. One has to begin with an input density  $n_{\text{in}}(\mathbf{r})$ , which gives the input potential  $V_s[n_{\text{in}}(\mathbf{r})]$ . Using this potential, the KS equations are solved, yielding a new density which is furthermore used to repeat the process. Once the iteration process does not anymore

change the density significant, the convergence has been achieved and the process has been completed.

The ground state density is defined for a sum of  $N$  lowest-energy KS eigenstate densities, and this hard cutoff can lead to convergence problems. Typical examples of such situations include metals and degenerate levels in finite systems such as  $d$ -shells of magnetic ions. The standard procedure to overcome this problem is to use thermal broadening via Fermi-Dirac statistics so that  $n = \sum_i f_i |\psi_i|^2$ , where

$$f_i = \frac{1}{\exp[(\epsilon_i - \mu)/T] + 1}, \quad (2.24)$$

with a chemical potential  $\mu$  such that  $\sum_i f_i = N$ .

For practical purposes, one should express the KS eigenvalues  $\psi_i$  in an orthogonal basis set. In the solid state physics the most natural choice is the plane wave basis given the itinerant nature of the Bloch wave functions. One must set a cutoff for this basis, which is done in terms of kinetic energy of the plane waves.

### 2.1.6 The pseudopotential approach

The KS scheme, in the form presented above, does not differentiate between core or valence-like solutions. However, the core level of freedom (core electronic density  $n_c(\mathbf{r})$ ) can be eliminated from the KS equations with the *frozen core approximation*. The chemically inert core states are well-localized around the deep potentials of the nuclei and are affected by the other atoms only by comparatively weak perturbations. Therefore, the core-like solutions may be expanded into atomic orbitals, and with the variational principle one can show that the perturbation in energy becomes of second order and the KS equations can be written in terms of the valence electron density  $n_v(\mathbf{r})$  as follows [23, 24]:

$$\left\{ -\frac{1}{2}\nabla^2 + \sum_I V_I^{\text{ps}}(\mathbf{r} - \mathbf{R}_I) + V_{\text{H}}[n_v(\mathbf{r})] + V_{\text{xc}}[n_v(\mathbf{r})] \right\} \psi_{v,i}(\mathbf{r}) = \epsilon_{v,i} \psi_{v,i}(\mathbf{r}). \quad (2.25)$$

The *pseudopotential* terms  $V_I^{\text{ps}}$  centered at ions  $I$  contain all the core electron effects, including terms corresponding to the electrostatic potential and the xc potential of the core electrons. This construction involves linearization of  $V_{\text{xc}}[n_c + n_v]$ , however, also the nonlinear core corrections can be taken into account [25]. The pseudopotentials can be pre-determined element-wise, and it is also possible to generate several pseudopotentials for one element by incorporating different amount of electrons to the core, corresponding to different chemical environments. The pseudopotential method is the norm in the DFT codes. In VASP it has been included in a more general form known as projector augmented wave (PAW) [26, 27] method, where an approximative basis set has been used inside the *PAW spheres* surrounding the nuclei.

### 2.1.7 The spin-orbit interaction

The above description is based on the Schrödinger equation Eq. (2.1), meaning that it is non-relativistic. When the electrons move with velocities close to the speed of light, relativistic effects become important. This condition is fulfilled in the case of heavy elements close to the nuclei. These effects could be taken into account by using the *Dirac equation*, however, the relativistic effects can be incorporated in the Schrödinger equation with simple correction terms. One of these terms is the *spin-orbit coupling* (SOC), which is proportional to  $\bar{\sigma} \cdot \mathbf{L}$ , where  $\bar{\sigma}$  is the spin operator and  $\mathbf{L} = \mathbf{r} \times \mathbf{p}$  is the angular momentum operator. In the rest frame of the lattice, there is no magnetic field acting on the electron, but in the rest frame of the electron there is a magnetic field caused by the relativistic transformation. Therefore, the electron spin is coupled with the lattice symmetry when relativistic corrections are considered. Without SOC the electronic spins can be rotated any angle without an effect on energy, but with SOC the angular momentum of the electrons, which is different for different atomic orbitals, couples to the spin degree of freedom.

## 2.2 The exchange-correlation functionals

### 2.2.1 Jabob’s ladder of density functional approximations

DFT is in principle an exact many-body theory [2], where all the many-body effects have been incorporated into the exchange-correlation functional. Even though exchange has an exact expression in Eq. 2.13,  $E_{xc}$  as a whole can not be described analytically, but it can be approximated with several different degrees of accuracy. Increasing the accuracy of  $E_{xc}$  by adding more complicated terms is known as “climbing up the *Jacob’s ladder*” [28], which has been illustrated in Table 2.1. At the “ground level”, the quantum-mechanical many-body interactions are not taken into account, but in principle the “heaven” of chemical accuracy can be gained with infinitely complex  $E_{xc}$  description.

Table 2.1: The Jacob’s ladder of DFT.

Rung	Dependence of $E_{xc}$	Examples	Locality
5th	$n, \nabla n, \nabla^2 n, \tau, \psi^{\text{occ}}, \psi^{\text{unocc}}$	RPA	Non-local
4th	$n, \nabla n, \nabla^2 n, \tau, \psi^{\text{occ}}$	Hybrid functionals	Non-local
3rd	$n, \nabla n, \nabla^2 n, \tau$	Meta-GGAs	Semilocal
2nd	$n, \nabla n$	GGAs	Semilocal
1st	$n$	LDA	Local

At the first rung of the Jacob’s ladder, the XC energy is a functional of the averaged electron density;  $E_{xc} = E_{xc}[n(\mathbf{r})]$ . Therefore, in this case,  $E_{xc}$  is *local*. The local density approximation (LDA) for non-spin-polarized systems or local spin density approximation (LSDA) for spin-polarized systems is the simplest possible such

approximation.

$$E_{xc} = \int d\mathbf{r} \varepsilon_{xc}(n(\mathbf{r}))n(\mathbf{r}). \quad (2.26)$$

Despite its simplicity, LDA has turned out to be surprisingly successful even in the highly inhomogeneous systems such as atoms and molecules.

In the second rung of the Jacob’s ladder also the gradient of the density is taken into account with the *Generalized Gradient Approximation* (GGA). The GGA functionals are *semilocal* because the gradient of the density is involved and information of an infinitesimally small region around  $\mathbf{r}$  is required. One of the most popular and successful GGA functionals is the Perdew, Burke, Ernzerhof (PBE) formulation [3].

The third rung of the Jacob’s ladder involves higher-order corrections, and therefore the generalized KS construction given by Eqs. (2.21–2.23) has to be applied. These corrections are the Laplacian of the Kohn-Sham orbitals, i.e., the kinetic energy density  $\tau$  given by Eq.(2.22), and the Laplacian of the electron density  $\nabla^2 n(\mathbf{r})$ . Typically, meta-GGA functionals include  $\tau$  but not  $\nabla^2 n$ :  $E_{xc} = E_{xc}[n(\mathbf{r}), \nabla n(\mathbf{r}), \tau(\mathbf{r})]$ .

In higher rungs full information of the KS eigenstates are required, and the XC functionals are *non-local*. The fourth rung contains for example the hybrid functionals, where the exact exchange [Eq. (2.13)] is mixed with exchange and correlation from other sources, such as with PBE  $E_{xc}$  functional in the case of PBE0 hybrid functional. The fifth rung also considers the unoccupied KS eigenstates, and it contains for example the *Random Phase Approximation* (RPA) [19].

## 2.2.2 The strongly constrained and appropriately normed meta-generalized gradient approximation

The strongly constrained and appropriately normed (SCAN) XC-functional [4] is a recently introduced meta-GGA functional that has shown great promise in describing strongly correlated matter [29–31]. The name “strongly constrained and appropriately normed” refers to SCAN satisfying all the 17 known exact constraints for a XC functional. The SCAN XC functional is designed to have a particularly strong sensitivity to different situations with chemical bonding and correlation. This goal has been achieved by constructing it with a dimensionless but position-dependent parameter  $\alpha(\mathbf{r})$ , which describes the local amount of kinetic energy density [4, 19]:

$$\alpha(\tau) = \frac{\tau(\mathbf{r}) - \tau^W(\mathbf{r})}{\tau^{\text{unif}}}, \quad \text{where} \quad (2.27)$$

$$\tau^{\text{unif}} = \frac{3}{10}(3\pi^2)^{2/3}n^{5/3}, \quad (2.28)$$

$$\tau^W = \frac{|\nabla n(\mathbf{r})|^2}{8n(\mathbf{r})}. \quad (2.29)$$

To characterize the above equations,  $\alpha$  is the KED scaled with KEDs of analytically solvable reference situations. These cases are the KED of the uniform electron

gas ( $\tau^{\text{unif}}$ ) and the KED of the single-orbital limit ( $\tau^{\text{W}}$ ), also known as the von Weizsäcker KED [19]. In the case of highly covalent systems  $\tau$  approaches  $\tau^{\text{W}}$ , (the case without any exchange nor correlation). Therefore,  $\alpha(\tau)$  approaches 0. Slowly-varying densities of metallic systems ( $\tau \sim \tau^{\text{unif}}$ ) are characterized by  $\alpha \approx 1$ . In the limit of noncovalent bonds between closed shells  $\alpha \gg 1$ . The  $\alpha$  parameter is further used to fit SCAN to match a large database of different systems. This generalized approach improves the description of the bandstructure and in particular, the energy gaps of insulators such as for example  $\text{La}_2\text{CuO}_4$  [29].

### 2.2.3 On-site Coulomb interactions

The strong on-site Coulomb interactions are particularly difficult to incorporate into the  $E_{\text{xc}}$  within the LDA and GGA levels. The self-interaction errors affect particularly the localized  $3d$  and  $4f$  orbitals, but can be also important for localized  $p$  electrons. Corrections to these errors are possible to introduce to the KS equations by an addition of an ad hoc Hubbard-like term [32–36]. The strength of the on-site interactions are usually described by the on-site Coulomb correlation  $U$  and on-site exchange  $J$ . Different kind of DFT+ $U$  implementations exist, but in this work we have employed the simplified and rotationally invariant scheme introduced by Duradev *et al.* [34], in which a penalty functional is added to the total energy expression:

$$E_{\text{DFT}+U} = E_{\text{DFT}} + \frac{U - J}{2} \sum_{\sigma} \left[ \left( \sum_{m_1} n_{m_1, m_2}^{\sigma} \right) - \left( \sum_{m_1, m_2} \hat{n}_{m_1, m_2}^{\sigma} \hat{n}_{m_2, m_1}^{\sigma} \right) \right], \quad (2.30)$$

where  $n_{m_1, m_2}^{\sigma}$  is the on-site occupancy matrix and  $\hat{n}$  is its idempotency ( $\hat{n}\hat{n} = \hat{n}$ ), implying that its elements are either 0 or 1, i.e., the eigenstates are fully unoccupied or occupied. The penalty term effectively forces the on-site occupancy matrix in the direction of idempotency.



# GATE-TUNABLE MAGNETISM ON GRAPHENE

## 3.1 Introduction

In the Publication I, we have employed *ab initio* DFT calculations to study various magnetic carbon adatom configurations on graphene and how is it possible to tune their magnetic interactions with an external gate voltage ( $V_g$ ). Although graphene itself is non-magnetic, the carbon atoms [37–44] become magnetic when placed on it. The carbon adatom binds on the bridge site of the graphene and has only one partially filled magnetic orbital at about 0.3 eV below the graphene Dirac point. We refer to this orbital as  $\psi_{p,\perp}$  because it possesses  $p$  symmetry with its axis perpendicular to the C–C bond of the bridge site, as illustrated in Fig. 3.1(a). The adatom induces a spin polarization in the graphene sheet, see Fig. 3.1 (b). This spin polarization can be experimentally probed by using the scanning tunneling microscopy (STM), as has been demonstrated in the case of hydrogen adatoms [45]. The  $\psi_{p,\perp}$  orbital hybridizes only weakly with the orbitals of the graphene atoms. Therefore, the high DOS of the  $\psi_{p,\perp}$  state is preserved and the occupation of the  $\psi_{p,\perp}$  state is easy to modify with a small external gate voltage. For all these reasons, the C adatom represents an ideal model in describing the interplay of a localized state with the itinerant electrons of the graphene backbone.

In this Chapter, I explore the magnetic phase diagram of the carbon adatom–graphene system with DFT by calculating the strength and sign of the magnetic interactions between C adatoms, using various degrees of correlation as captured by GGA and SCAN. In particular, I show that there are FM phases for certain gate voltages. Although carbon adatoms are mobile at room temperature, some adatom configurations may be stabilized in special conditions [43].

## 3.2 Theoretical considerations

Impurities interacting with one of the two sublattices  $A$  or  $B$  of graphene has been an intensively studied field. The Lieb’s theorem [46] applies to these cases. As its consequence, two impurities interact ferromagnetically/antiferromagnetic for impurities in same/different sublattices. However, these limitations do not apply for

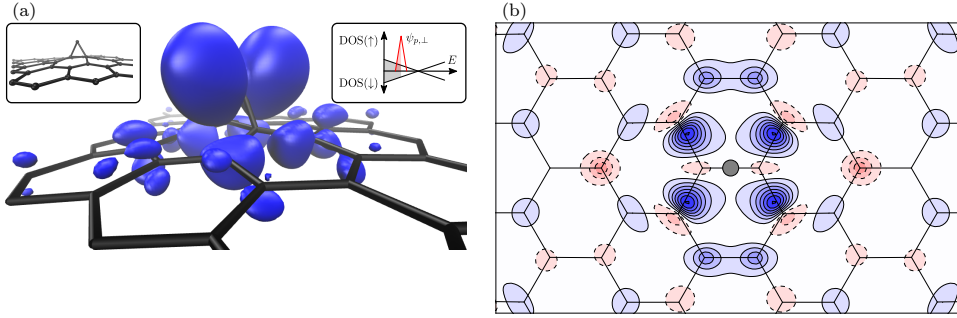


Figure 3.1: (a): Visualization of the  $\psi_{p,\perp}$  orbital by the means of a magnetization density isosurface plot. Also the  $p_z$  character on the graphene sheet can be seen. Left inset: the geometry. Right inset: schematic electronic structure of the system. (b): Magnetization density isosurface cut on the graphene plane, red corresponds to opposite spin regions. From Publication I.

bridge site adatoms such as C adatoms, since they couple with both sublattices. In this case, the Lieb's theorem does not apply, which allows ferromagnetism within the C adatom network for randomly positioned impurities.

Interactions of magnetic impurities in graphene have been extensively investigated using the Ruderman-Kittel-Kasuya-Yosida (RKKY) theory [47], where itinerant graphene states mediate an indirect exchange interaction between localized magnetic moments. However, in reality the impurity states have some spillover on the graphene plane. Consequently, hybridization appears and an impurity band forms [48]. The small coupling between the impurity states leads to a narrow band with large DOS. If  $E_F$  is inside the impurity band, ferromagnetism appears. To justify this statement, we consider the Hubbard Hamiltonian to account for the on-site electron-electron interaction:

$$H_U = \sum_i U n_{i\uparrow} n_{i\downarrow}, \quad (3.1)$$

where the summation is over graphene and the adatom sites,  $n_{i\sigma}$  is the occupation number operator for electron with spin projection  $\sigma$  at site  $i$ . The parameter  $U$  characterizes the on-site Coulomb interaction energy for the two electrons occupying carbon  $p_z$  atomic orbital. Within the mean-field approximation, the Hubbard model becomes the Stoner model [48, 49], which provides ferromagnetism when the Stoner criterion is fulfilled

$$U \cdot \text{DOS}(E_F) > 1. \quad (3.2)$$

### 3.3 One carbon adatom per unit cell

The DFT calculations were performed using VASP with the GGA (based on the Perdew-Burke-Ernzerhof (PBE) formulation [3]) and SCAN methods. The cutoff

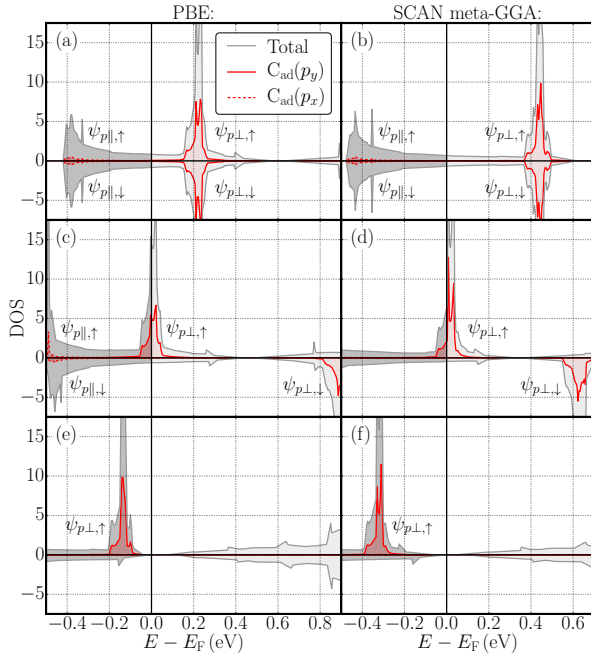


Figure 3.2: (a)–(f): DOS and C adatom PDOS for  $\Delta Q = -0.5e, 0$  and  $1e$  with GGA and SCAN. From Publication I.

energy was set to 600 eV. We have simulated the gate voltage by adding  $\Delta Q/e$  electrons to the system as well as a “jellium” background charge in order to keep the system charge neutral, similarly with previous graphene adatom studies [50–53]. For a detailed discussion of the possible error included in the addition of the background charge, see the Supplemental Material of the Publication I. The gate voltage is a function of  $\Delta Q$ , but the direct relation depends on the size of the SC and the density of states at the Fermi level. Nevertheless, obviously for example  $\Delta Q = 0$  corresponds to  $V_g = 0$ .

We first examine the effects of gate voltage on the magnetic and geometrical properties of a single C adatom on a  $4 \times 4$  graphene supercell (SCs). Because of the periodic boundary conditions, this configuration corresponds to a periodic adatom coverage. Figure 3.2 compares the partial density of states (PDOS) of this system for both the GGA and SCAN schemes and for different values of  $\Delta Q$ . These plots feature the magnetic  $\psi_{p,\perp}$  orbitals as well as the deeper non-magnetic  $\psi_{p,\parallel}$  orbitals that participate in the hybridization with the graphene sheet. Starting from  $\Delta Q = -0.5e$ , the  $\psi_{p,\perp}$  states are unoccupied and degenerate in energy. When charge is added to the unit cell, the Fermi level rises above the  $\psi_{p,\perp,\uparrow}$  state and  $\psi_{p,\perp,\uparrow}$  separates from the  $\psi_{p,\perp,\downarrow}$  state given the fulfillment of the Stoner’s criterion Eq. (3.2). Consequently, the system magnetizes, and when  $\Delta Q = 0$ , the magnetic moment per adatom is  $M = 0.38 \mu_B$  for GGA (Fig. 3.2 (c)) and  $M = 0.24 \mu_B$  for SCAN (Fig. 3.2 (d)), respectively. At  $\Delta Q = 1e$ , the  $\psi_{p,\perp}$  impurity state has been completely filled, as illustrated in Figs. 3.2 (e) and 3.2 (f), saturating the magnetization at  $1 \mu_B$ . Figure 3.3 presents the magnetization curves as a function of  $\Delta Q$ . The slope for GGA is about  $0.65 \mu_B/e$  before the  $\psi_{p,\perp}$  state becomes full at  $\Delta Q = 1e$ . Interestingly, the

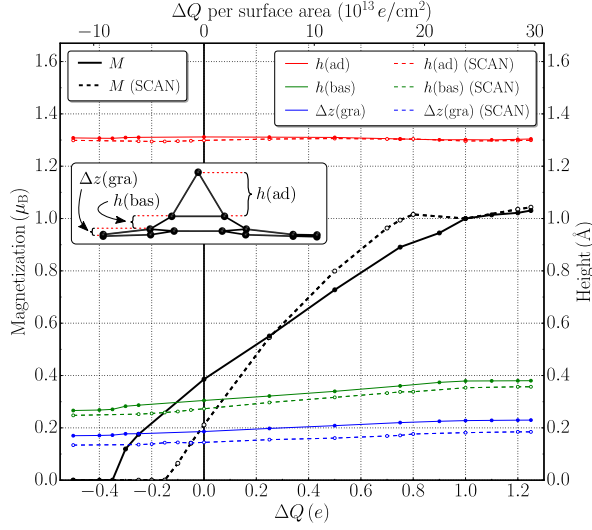


Figure 3.3: The magnetic moment of the whole SC and the structural parameters  $h(\text{ad})$ ,  $h(\text{bas})$  and  $\Delta z(\text{gra})$  for different  $\Delta Q$  values. The inset illustrates the structure (relaxed with GGA for  $\Delta Q = 1.25 e$ ) and the structural parameter definitions. From Publication I.

SCAN curve is more steep than that of GGA, with a slope as high as  $1.4 e/\mu_B$  below  $M \approx 0.5\mu_B$ . Moreover, SCAN presents a nonlinear behavior in the region below  $M \lesssim 0.2\mu_B$ , which is related to breakdown of the Stoner model.

The gate voltage also affects the geometrical properties by lifting the adatom and its basal atoms, and in general increasing the buckling of the graphene sheet around the adatom, as shown in Fig. 3.2(g). Interestingly, the almost equilateral triangle formed by the adatom and its two basal atoms keeps its shape in this process; the height of the adatom C with respect to the basal atoms [ $h(\text{ad})$ ] is about  $1.30 \text{\AA}$  for all doping values for both GGA and SCAN. More noticeable is the upwards movement of the triangle when  $\Delta Q$  is filled, which is seen by the increase of  $h(\text{bas})$  by  $0.08 \text{\AA}$  and in the increase of  $\Delta z(\text{gra})$  by  $0.04 \text{\AA}$ . The GGA and SCAN give qualitatively similar results, but the SCAN values are systematically about  $0.03 \text{\AA}$  larger for  $h(\text{bas})$  and  $0.05 \text{\AA}$  larger for  $\Delta z(\text{gra})$ . Without gate voltage,  $h(\text{bas}) = 0.27 \text{\AA}$ ,  $\Delta z(\text{gra}) = 0.15 \text{\AA}$  and the total height of the system is  $1.72 \text{\AA}$ .

The GGA binding energies of the C adatom slightly depend on the size of the used SC, with the values of  $-1.46 \text{ eV}$ ,  $-1.52 \text{ eV}$ ,  $-1.51 \text{ eV}$  and  $-1.52 \text{ eV}$  for  $3 \times 3$ ,  $4 \times 4$ ,  $5 \times 5$  and  $9 \times 9$  SCs, respectively. These values are in agreement with the earlier studies with values  $-1.46 \text{ eV}$  [54] and  $-1.63 \text{ eV}$  [38]. We also computed the binding energies for SCAN, and a slight decrease in binding energy was observed. We obtained  $-1.44 \text{ eV}$  and  $-1.46 \text{ eV}$  for  $4 \times 4$  and  $5 \times 5$  SCs, respectively.

### 3.4 Interactions between adatoms

The interactions between C adatoms were studied by placing two adatoms  $C_1^{\text{ad}}$  and  $C_2^{\text{ad}}$  in different geometrical configurations on a graphene supercell (SC). In each of these cases, we have computed two different solutions with parallel (FM)

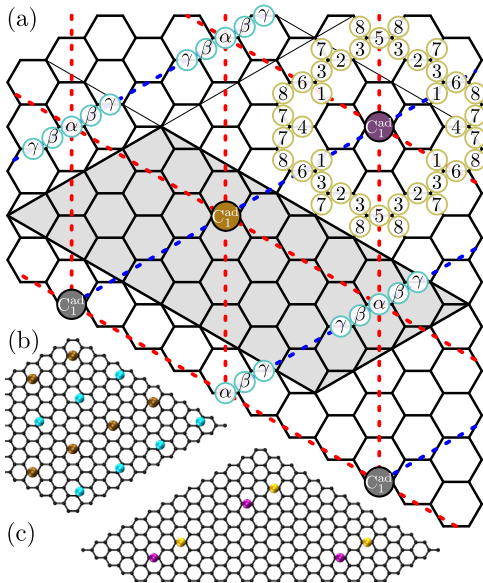


Figure 3.4: (a): The adatom pairs are defined by the purple  $C_1^{\text{ad}}$  and one of the sites from #1 to #8. The adatom arrays are defined by the ochre  $C_1^{\text{ad}}$  and one of the sites  $\alpha$ ,  $\beta$  or  $\gamma$ . The periodic images of  $C_1^{\text{ad}}$  are colored gray. The present adatom array illustration is for a  $8 \times 4$  SC. The nearest-neighbour interactions of the  $\alpha$  array are marked with dashed lines (blue/red for FM/AFM interactions). (b): The adatom array  $\beta(6 \times 3)$  array. (c): The adatom pair Conf. #6 (placed on a  $7 \times 7$  SC). From Publication I.

and antiparallel (AFM) adatom spin configurations. The energy difference  $\Delta E = E(\text{FM}) - E(\text{AFM})$  reveals the strength of the magnetic interactions. We used two different adatom configuration types. These types were *adatom array configurations*  $\alpha$ ,  $\beta$  and  $\gamma$ , intended for the study of long (7–10 Å) distance interactions, and *adatom pair configurations* #1–#8, intended for the study of interactions of shorter distances. Both configuration types are illustrated in Fig. 3.4 and further details are given in Publication I. Moreover, we considered both one-sided and two-sided adsorptions of the two adatoms.

### 3.4.1 Energetics of two-adatom configurations

We have compared the energies of the two-adatom configurations with respect to the dimerized system and with respect to the system of two isolated adatoms. This comparison provides information about the energetics of the structural deformations and the magnetic interactions. The adatoms dimerize when they get closer than what they are in the Conf. #1 (see Fig. 3.4). When the dimerization occurs, one of the atoms climbs on top the another one and the dimer migrates on a top site of the graphene sheet and loses its magnetic moment, in accordance with previous observations [55]. The dimer was found to have 5.42 eV lower energy than the lowest-energy non-dimerized structure Conf. #4 ( $7 \times 7$  SC), which in turn was found to have 314 meV lower energy than two isolated adatoms (we considered an adatom in a  $7 \times 7$  SC to be isolated). Based on these results, the attractive potential between the adatoms is strong, and low temperatures are required for its stabilization.

Table 3.1 contains the total energies of Confs. #1–#8 (see Fig. 3.4). Interestingly, the Conf. #4 has the lowest energy also for the other SC size and for both one-sided and two-sided adsorptions. This might be due to the low symmetry of this

Table 3.1: Total energy of each adatom pair configuration with respect to the dimer solution computed at  $7 \times 7$  SC determined with the formula  $E_{\text{dimer}} + E_{\text{graphene}} - 2 \cdot E_{\text{gra+adatom}}$ . In parenthesis: with respect to Conf. #4 ( $7 \times 7$  SC), which has the lowest total energy among the one-sided adsorption cases. Also the  $6 \times 3$  SC size is considered by converting the  $7 \times 7$  SC dimer and Conf. #4 energies to  $6 \times 3$  SC size by subtracting the primitive cell energy  $7 \cdot 7 - 6 \cdot 3 = 31$  times from them.

Conf.	Relative total energy (eV)		
	$7 \times 7$	$7 \times 7$ (two-sided)	$6 \times 3$
#1	5.60 (+0.183)	5.40 (−0.016)	5.64 (+0.227)
#2	5.56 (+0.139)	5.55 (+0.129)	5.70 (+0.288)
#3	5.61 (+0.196)	5.61 (+0.191)	5.75 (+0.330)
#4	5.42 (+0.000)	5.38 (−0.035)	5.48 (+0.063)
#5	5.54 (+0.125)	5.54 (+0.128)	5.63 (+0.217)
#6	5.75 (+0.337)	5.68 (+0.260)	5.75 (+0.335)
#7	5.65 (+0.233)	5.65 (+0.229)	5.70 (+0.278)
#8	5.63 (+0.217)	5.58 (+0.167)	5.71 (+0.294)

configuration, which allows symmetric displacements of the graphene atoms. In accordance with this possible explanation also another high-symmetry configuration (Conf. #5) is rather low in energy. In general, the adatom pairs with lower separations (Confs. #1 – #3) are lower in energy than the adatom pairs with higher separations (Confs. #6 – #8), in accordance with the existence of the attractive potential between the adatoms. The two-sided configuration is energetically more favorable in nearly every case, which is most likely due to smaller amount of curvature-related bending energy on the graphene sheet.

### 3.4.2 Magnetic interactions of adatoms under gate voltage

In this subsection we focus on the main results of the Publication I concerning the magnetic adatom-adatom interactions. Figures 3.5 and 3.6 contain our results on the adatom arrays and the adatom pair configurations (see Fig. 3.4). for different SC sizes. In these figures  $\overline{\Delta Q} = \Delta Q/2$  is the amount of added charge per adatom and  $\overline{M} = M(\text{FM})/2$  is the averaged magnetization per adatom of the FM solutions. The results for  $\overline{M}$  as a function of  $\overline{\Delta Q}$  are very similar to the single-adatom result of Fig. 3.3 especially for the adatom arrays (Fig. 4.2). In the case of adatom pair configurations (Fig. 4.3), there are significant fluctuations in the  $\overline{M}$  curves below  $\overline{\Delta Q}$ . This behavior is produced by the strong interactions and structural deformations due to the close proximity of the adatoms, which in some cases lift the normally low-lying  $\psi_{p,\parallel}$  orbitals to  $E_{\text{F}}$ . The  $\psi_{p,\parallel}$  thus contribute on the magnetic moments, but when the gate voltage is increased, these states are re-filled and the linear behavior of  $\overline{M}$  is recovered. At  $V_{\text{g}} = 0$  the SCAN magnetizations are smaller than for GGA, in fact for  $\alpha(6 \times 3)$   $\overline{M} = 0$ .

The magnetic interaction energy is contained in the energy difference  $\Delta E = E(\text{FM}) -$

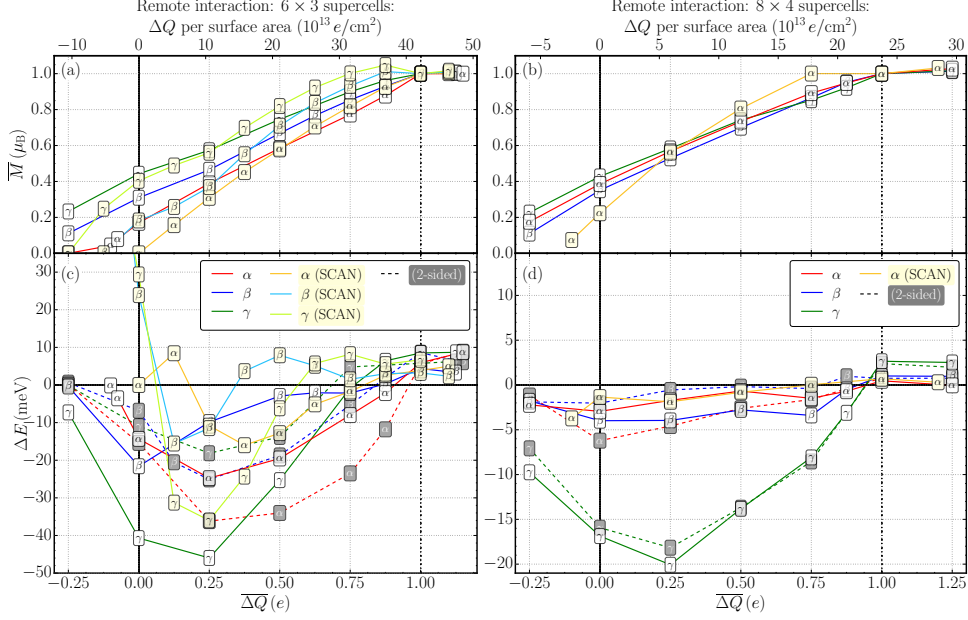


Figure 3.5: Adatom arrays: panels (a) and (b) represent  $\bar{M}$  for  $6 \times 3$  and  $8 \times 4$  SCs, respectively. Panels (c) and (d) represent  $\Delta E$  for  $6 \times 3$  and  $8 \times 4$  SCs, respectively. The solid/dashed lines and light/dark markers correspond to one-sided/two-sided adsorption of the two adatoms. From Publication I.

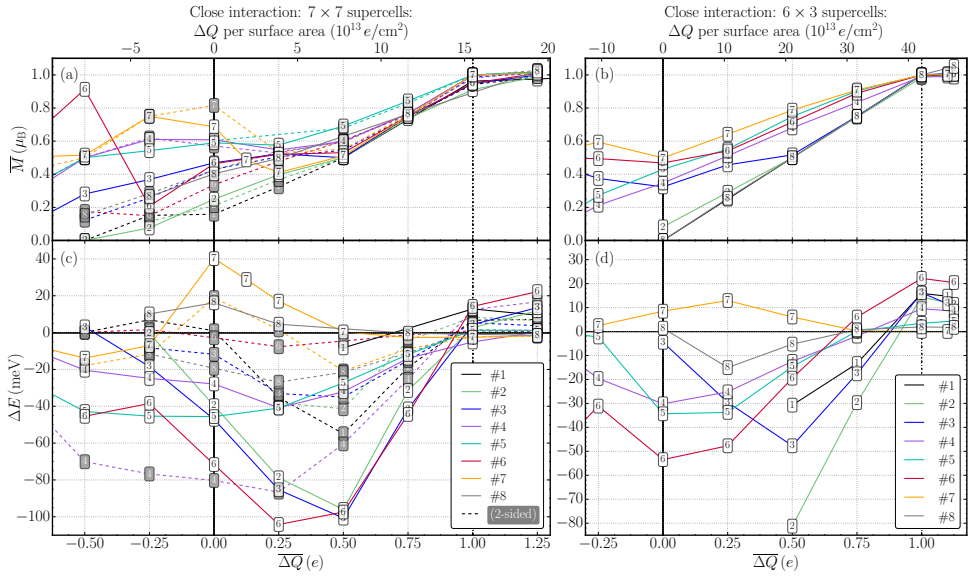


Figure 3.6: Same as Fig. 3.5 but for adatom pairs. From Publication I.

$E(\text{AFM})$ . When the impurity states are partially filled (in the case of intermediate gate voltages), clear ferromagnetic valleys are formed in each configuration. Representative maximum values for  $\Delta E$  are about  $-30 \text{ meV}$  and  $-5 \text{ meV}$  for  $6 \times 3$  and  $8 \times 4$  SCs, respectively. In the case of structures with two-sided adsorption the energy difference magnitudes are larger for  $\alpha$  but smaller for  $\gamma$ . For  $\beta$  arrays, the ferromagnetism for two-sided adsorption is clearly weaker for the  $8 \times 4$  SCs but for the  $6 \times 3$  SCs there is no clear difference in the maximum  $\Delta E$  magnitude. In general, the  $\gamma$  arrays yield the most robust ferromagnetism, especially for the  $8 \times 4$  SCs. Also the total energies are lower for the  $\gamma$  arrays. Interestingly, the most stable FM solution depends on the occupation of the  $\psi_{p,\perp}$  state. Regardless of the SC size or the XC functional, this solution corresponds to  $\overline{M} = (0.40 \pm 0.05) \mu_B$ ,  $(0.35 \pm 0.10) \mu_B$  and  $(0.55 \pm 0.05) \mu_B$  for  $\alpha$ ,  $\beta$  and  $\gamma$  arrays, respectively. These results can be understood within the Stoner model.

For low magnetizations, SCAN yields strong AFM excursions especially for  $\gamma(6 \times 3)$  and  $\beta(6 \times 3)$  but also for  $\alpha(6 \times 3)$ , meanwhile this phenomenon is completely absent in the PBE results. This can be attributed to RKKY interactions, as discussed in detail in the Publication I. When the  $\psi_{p,\perp}$  orbitals become fully occupied,  $\Delta E$  reaches AFM plateaus. In this region the impurities do not anymore interact via the Stoner's mechanism, which could be explained with another type of in this  $\overline{\Delta Q}$  region RKKY is described within the resonant RKKY model, as discussed in detail in the Publication I.

In the case of the adatom pair configurations, also the  $\Delta E$  curves feature excursions at low- $V_g$  region ( $\overline{\Delta Q} \lesssim 0.5 e$ ), which is also a consequence of the additional complications by the  $\psi_{p,\parallel}$  states. In general, the strongest FM valleys are found within the  $7 \times 7$  SC adatom pair configurations, the strongest interaction values being  $-104 \text{ meV}$  (Conf. #6).

The close interaction pairs were studied also within  $6 \times 3$  SCs. The purpose for this smaller SC was to simulate random adatom distributions on graphene by not isolating the adatom pair well. Therefore, it is expected to observe stronger ferromagnetism on these smaller SCs. However, in general the  $\Delta E$  values drop in the smaller SC. Typical values are now about  $-30 \text{ meV}$  and the largest values are  $-55 \text{ meV}$ . Evidently the larger concentration of the adatoms spreads the  $\psi_{p,\perp}$  energy band, weakening the Stoner splitting. Indeed, the  $\psi_{p,\perp}$  state widths in PDOS are increased to  $\sim 0.4 \text{ eV}$  from the value of  $\sim 0.1 \text{ eV}$  in the case of  $7 \times 7$  SC configurations. Consistently, Ref. [56] has pointed out that in the case of  $p$ -character band ferromagnetism the ferromagnetic ordering must be inhomogeneous with only a fraction of the sample magnetized.

### 3.5 Conclusion

The gate voltage can control the magnetic properties of the system composed of carbon-adatom and graphene studied in Publication I. This voltage varies the magnetic moment of the adatoms from zero to  $1 \mu_B$  by changing the occupation of the

adatom localized magnetic state. Moreover,  $V_g$  changes the magnetic interactions between FM and AFM. The AFM phase is predicted for both low and high adatom magnetic moments and the FM phase for intermediate magnetic moments. The Stoner's criterion is satisfied for the FM phase and the Fermi energy is inside the impurity band. The low-magnetization AFM phase can be rationalized within the RKKY mechanism and can be only found within the SCAN meta-GGA framework, more suitable to describe the localized impurity states. The AFM phase at high magnetic moments could be the result of an interplay between direct and RKKY interactions. Both GGA and SCAN predict strong FM phases. Despite some small differences in the magnetic properties, the role of the SCAN correction to GGA was found to be minor. Despite of the fact of carbon adatom system being difficult to stabilize, our results can be generalized to other systems with magnetic defects coupling to the both  $A$  and  $B$  graphene sublattices, or more generally to magnetic 2D materials. In particular, our results provide a theoretical proof-of-concept of a new kind of spin-field-effect transistor which can be controlled by an external gate [5, 6]. Gate-tunable room-temperature ferromagnetism has already been realized in  $\text{Fe}_3\text{GeTe}_2$  [7].



# CORRELATION IN ELEMENTAL MANGANESE

## 4.1 Introduction

In Publication II, we have used SCAN to explore the role of Coulomb correlation in elemental manganese, which is in fact one of the most complex metallic elements [9–15]. Such effects are already present in the manganese dimer ( $\text{Mn}_2$ ) and in Mn clusters, and in solid manganese these effects lead to complex interplay of localization of magnetic moments and itinerant behavior, which drives the rich phase diagram of Mn. This phase diagram yields increasingly complex structures with decreasing temperature, as illustrated in Fig. 4.1. The most complex solid phase is the low-temperature phase  $\alpha$ -Mn, possessing a sophisticated noncollinear spin texture visualized in Fig. 4.1. The unit cell of  $\alpha$ -Mn has space group  $T_d^3$  and it consists of 58 atoms that are distributed among four sublattices, and the Mn magnetic moments have different magnitudes at each sublattice. Curiously, the magnetic moments are large and almost collinear on two of the sublattices, but on the two other sublattices the magnetic moments are significantly smaller with strongly noncollinear spin alignments. large distortions in the spin angles. The magnetic nor structural properties of the  $\alpha$ -Mn phase can not be captured by LSDA nor GGA [9, 10]. To describe this complex phase, it has been needed to apply prominently strong external Hubbard  $U$  together with artificially expanded lattice [10].

In this Chapter, I discuss the role of Coulomb correlation in several phases of Mn, including the Mn dimer,  $\gamma$ -Mn and  $\alpha$ -Mn, by using SCAN and also SCAN+ $U$ , where further correlations with the external Hubbard  $U$  parameter have been introduced. Also some GGA and GGA +  $U$  calculations have been performed for reference.

## 4.2 Results

The DFT calculations were performed using VASP with the GGA (based on the Perdew-Burke-Ernzerhof (PBE) formulation [3]) and SCAN methods. The cutoff energy was set to  $\geq 550$  eV and a  $k$ -point spacing of  $< 0.02 \text{ \AA}^{-1}$  was used.

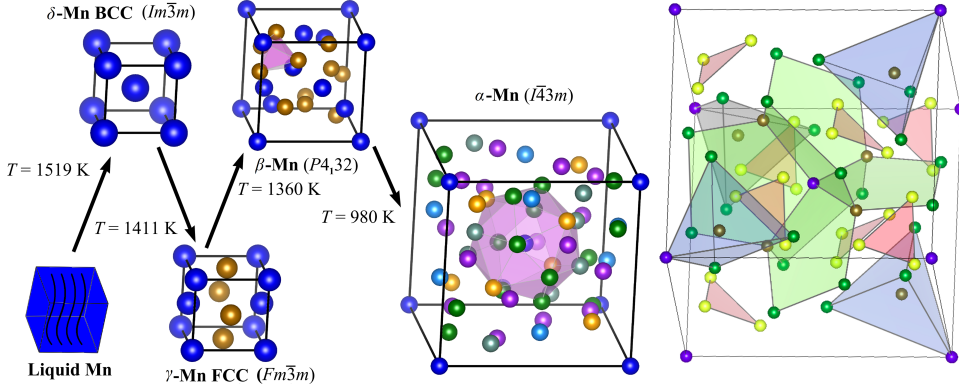


Figure 4.1: Schematic phase diagram of elemental Mn. Coloring of atoms denotes to different crystallographic sublattices. The low-temperature phase  $\alpha$ -Mn contains a 17-atom cluster (the purple polyhedron in the structure second from the right) described by Prout & Donnadiu [57]. Another illustration of  $\alpha$ -Mn is provided (on the right), where six symmetric pentagons (green) are connected to each other and to a central Mn atom. Rest of the atoms can be connected symmetrically with tetrahedra and triangles. From Publication II.

### 4.2.1 Mn dimer

The Mn dimer is an interesting and sophisticated test for correlation in Mn, despite of its simplicity. We have considered  $Mn_2$  in the GGA +  $U$  and SCAN +  $U$  schemes. Figure 4.2 shows the energy difference between the ferromagnetic and antiferromagnetic configurations as a function of the Mn–Mn bond length for several different values of  $U$ . The results for GGA +  $U$  and SCAN +  $U$  are presented in Figs 4.2 (a) and 4.2 (b), respectively. The energy differences ( $\Delta E$ ) and the equilibrium Mn–Mn distances obtained from the results of Fig. 4.2 are collected in Fig. 4.3. Huang *et al.* [32] have shown previously with their GGA +  $U$  calculations that the Mn dimer contains a significant self-interaction contribution, and our GGA +  $U$  results show similar trend: Without any correction ( $U = 0$ ) the GGA yields an FM ground state for the Mn dimer with a short (2.6 Å) bond length. However, experimentally the Mn dimer is found to assume an AFM ground state with a large (3.2 Å) bond length. Addition of the Hubbard  $U$  weakens the hybridization between  $s$  and  $d$  orbitals and restores the correct AFM ground state with a large bond length. The FM–AFM transition occurs for values slightly above  $U = 2$  eV. A similar behavior is seen in SCAN +  $U$ , except that the FM–AFM transition now occurs for values slightly above  $U = 1$  eV. In fact, an examination of the results of Figs. 4.2 and 4.3 shows more generally that SCAN (without  $U$ ) already contains an effective  $U$  of about 1 eV. Even the pristine SCAN ( $U = 0$  eV) qualitatively captures the correct double-minimum for the FM solution and the long bond length associated with the AFM solution, while the GGA for  $U = 0$  only yields short-bond-length FM and AFM solutions. Moreover, for pristine SCAN, the ordering of the long-bond-length FM and AFM solutions is correct while for GGA + ( $U = 1$  eV) the AFM solution is energetically

above the long-bond-length FM solution.

### 4.2.2 $\gamma$ -Mn

The  $\gamma$ -Mn unit cell is described as four manganese atoms arranged in the face-centered cubic (FCC) lattice. AFM order develops in  $\gamma$ -Mn with two possible spin configurations (AF1 and AF2) described in the book by Kubler [58]. According to Asada and Terakura [59], in the AF1 phase, the LSDA overbinds the Mn atoms and therefore underestimates the lattice constant and cannot predict the experimentally verified AFM ground state. Our total energy calculations within GGA and SCAN for the non-magnetic, FM, and AF1 and AF2 phases confirm that the ground state of  $\gamma$ -Mn is AF1. GGA gives an equilibrium volume corresponding to the Wigner-Seitz radius of  $R_{ws} = 2.635$  a.u.. SCAN yields  $R_{ws} = 2.732$  a.u., in better agreement with the experimental Wigner-Seitz radius of  $R_{ws} = 2.752$  a.u. [60]. The structure has a tetragonal distortion  $c/a = 0.95$  for GGA, whereas SCAN gives  $c/a = 0.98$ . The computed magnetic moments increase with the equilibrium volume, therefore GGA gives  $1.74 \mu_B$  whereas SCAN yields a larger value equal to  $3.10 \mu_B$ . To estimate the importance of corrections beyond the GGA contained in SCAN, one can compare the SCAN, GGA and GGA+ $U$  results to extract an effective  $U$  value, which reproduces the experimental equilibrium volume. We have performed this comparison, and found that  $U = 1.1$  eV. In accordance with this behavior, the  $d$ -orbital PDOS for GGA+( $U = 1.1$  eV) resembles the corresponding PDOS for SCAN, but clearly differs from plain GGA PDOS, as shown in Fig. 4.4. the equilibrium Wigner-Seitz radius is  $R_{ws} = 2.722$  a.u., the Mn magnetic moments are  $2.69 \mu_B$  and  $c/a$  is equal to 0.98. Similar results have been reported by Podloucky & Redinger [61] and Di Marco *et al.* [62, 63]. These results are also consistent with the ARPES observation of Hubbard bands [64].

### 4.2.3 Noncollinear antiferromagnetic $\alpha$ -Mn

In this subsection we focus on the main results of the Publication II concerning the complex low-temperature phase  $\alpha$ -Mn. The cohesive energy  $E_{coh}$  of  $\alpha$ -Mn as a function of  $R_{ws}$  is shown in Figure 4.5 under various approximations. We first approximate  $\alpha$ -Mn with collinear calculations, and SCAN corrects the GGA volume already within this approximation. The bulk modulus of the collinear solution is 131 GPa, which is in good agreement with the experimental value of 151 GPa [65], and the calculated magnetic moment distribution displays a behavior consistent with the experiment Ref. [10]. Nevertheless, a detailed comparison with these calculations is difficult since the experimental magnetic moments strongly depend on the choice of the form factors [66]. Interestingly, we also find another collinear solution at a larger volume, with a bulk modulus equal to 68 GPa. The magnetic distribution of this metastable solution is ferrimagnetic with an average moment of  $0.11 \mu_B$  per Mn atom. Moreover, charge distribution of this solution involves manganese atoms in six different electronic configurations with charge differences of about  $0.4 e$ /atom.

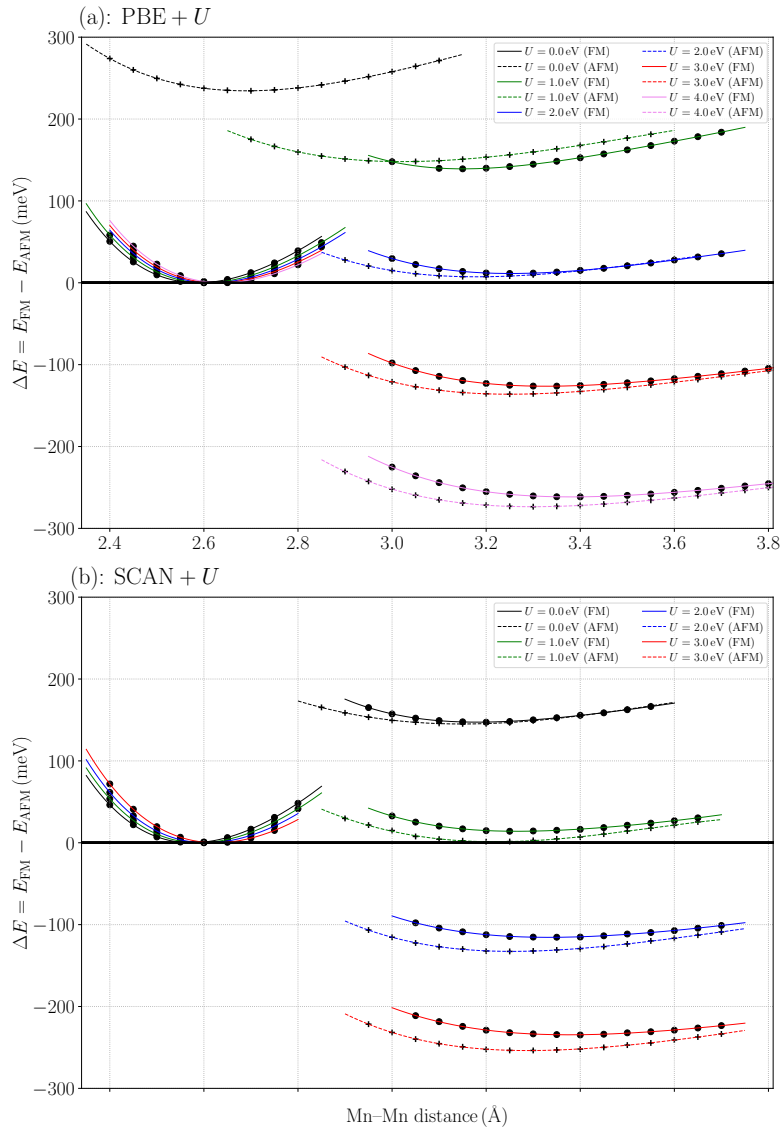


Figure 4.2: Energetics of the FM and AFM configurations of the Mn dimer. (a): PBE +  $U$  and (b): SCAN +  $U$ . Two long bond length solutions are obtained for each  $U$ . Except for PBE + ( $U = 1$  eV), the long bond length AF solution is more stable than the corresponding FM solution. From Publication II.

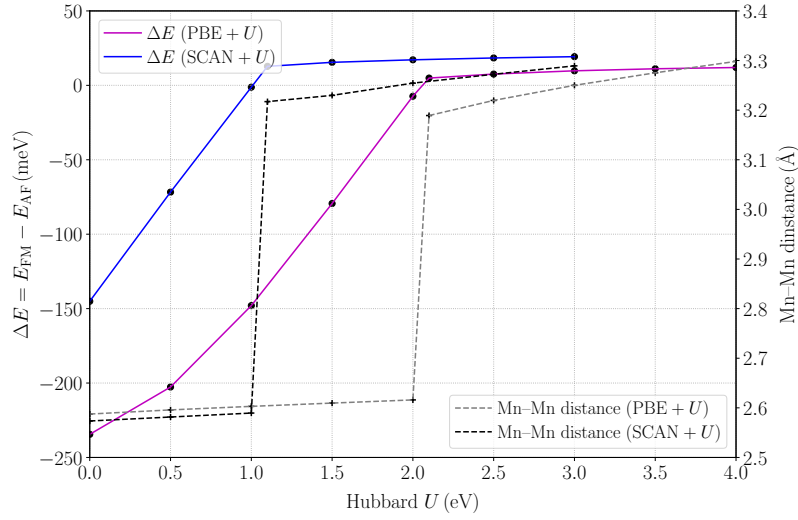


Figure 4.3:  $\Delta E = E_{\text{FM}} - E_{\text{AF}}$  and  $\text{Mn}_2$  ground state bond length as a function of Hubbard  $U$ . From Publication II.

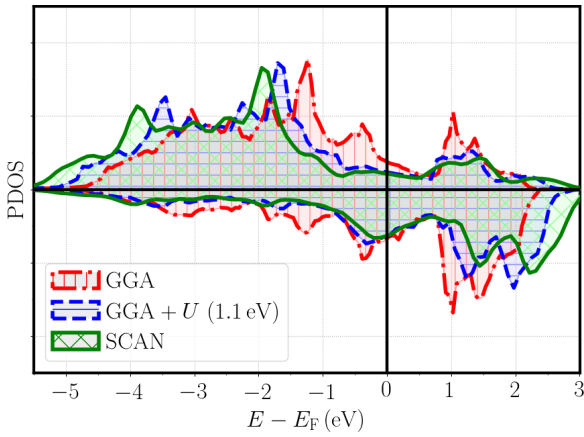


Figure 4.4: Mn  $d$ -orbital PDOS at the experimental equilibrium volume for GGA, GGA+( $U = 1.1$  eV) and SCAN. From Publication II.

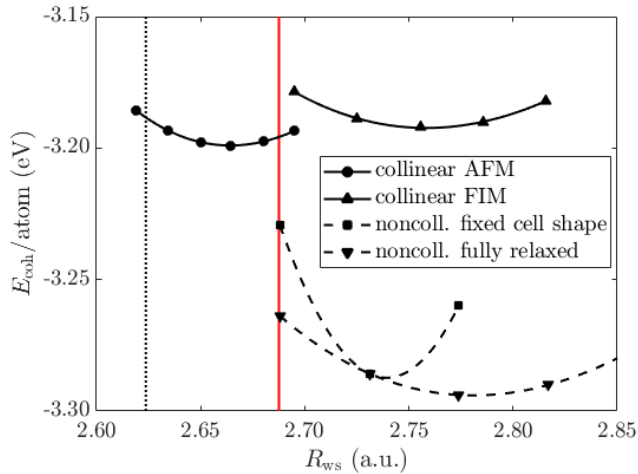


Figure 4.5: SCAN cohesive energies for  $\alpha$ -Mn as a function of  $R_{ws}$ . The solid red line denotes the experimental volume [66], and the dashed line marks the GGA  $R_{ws}$  [3]. From Publication II.

We performed two different types of noncollinear calculations. In the first one we allowed fully relaxed atomic positions with a fixed cell shape, while in the second one we fully relaxed the system. The complex magnetic structure of these simulations are illustrated in Fig. 4.6 and the energetics are contained in Fig. 4.5. The complex noncollinear spin structures appear to reduce frustration. It can be seen that the magnetic structure is noncollinear at the experimental volume, which is not the case for GGA [10]. The solution corresponding to the simulation with fixed cell shape gives a smaller equilibrium volume. Fully relaxing the structure gives  $R_{ws} = 2.781$  a.u., which might correspond to the strained  $\alpha$ -phase described by Dedkov *et al.* [67]. Since SCAN tends to favor solutions with high magnetic moments, the stabilization of the strained  $\alpha$ -phase could be an overcorrection of SCAN [8, 68].

### 4.3 Conclusion

Both Mn dimer and  $\gamma$ -Mn calculations with GGA+ $U$  and SCAN+ $U$ , SCAN contains an effective  $U$  of about 1 eV when compared to GGA. However, in the case of Mn dimer, SCAN appears to underestimate the required amount of correlation needed to explain the long bond length and AFM ordering of the dimer. In  $\alpha$ -Mn, SCAN results considerably improve the prediction of its ground-state compared to the LSDA and GGA. In particular, SCAN successfully predicts the complex charge and noncollinear magnetic patterns. However, compared to GGA, SCAN appears to overcorrect some features in  $\alpha$ -Mn. Our previous calculations [8] have shown that in Mn-poor Heusler alloys the SCAN corrections to GGA are small. The present results for pristine manganese rationalise the substantial differences between GGA

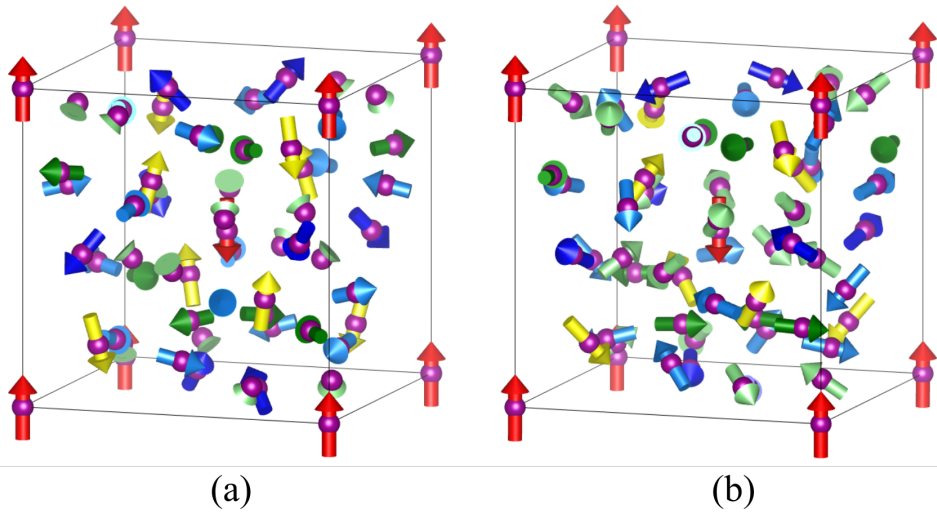


Figure 4.6: SCAN noncollinear magnetic structure in  $\alpha$ -Mn. In case (a), only the atomic positions are relaxed, while both the atomic positions and the cell shape are relaxed in case (b). Different colors correspond to the four different sublattices.

and SCAN observed in Mn-rich compounds. Clearly, the existence of spin and charge modulations in  $\alpha$ -Mn can explain the rich phase diagrams of Heusler alloys with heterogeneous phases.



# CORRELATION IN A HIGH-TEMPERATURE SUPERCONDUCTOR

## 5.1 Introduction

In Publication III, we have used SCAN to explore the electronic, structural and magnetic properties of  $\text{Bi}_2\text{Sr}_2\text{CuO}_6$  (Bi2201) and  $\text{Bi}_2\text{Sr}_2\text{CaCu}_2\text{O}_8$  (Bi2212), which are members of the Bi-Sr-Ca-Cu-O (BSCCO) high-temperature bismuth cuprate superconductor family [69–71]. BSCCO is one of the most studied cuprates, as the weak van der Waals (vdW)-like coupling between BiO planes (see Fig. 5.1) allows easy cleaving for accurate surface studies with angle-resolved photoemission spectroscopy (ARPES) [72–77] and with scanning tunneling spectroscopy (STM) [78–82]. The explanation of the high- $T_c$  superconductivity in cuprates is still one of the biggest open questions in physics. This superconductivity takes place at the half-filled quasi-two-dimensional  $\text{CuO}_2$  planes, which have been recently demonstrated to possess strong long-range AFM ordering on the Cu ions [83]. A common feature in cuprate superconductors is the existence of the superconducting dome, i.e., the trend, where  $T_c$  first increases and then decreases as a function of number of electronic holes. These holes are typically introduced to the system by oxygen doping. The oxygen doping is intimately connected to the antiferromagnetism in the  $\text{CuO}_2$  planes by diluting the highly correlated Cu magnetic moments, driving the competition between these magnetic moments and itinerant electrons. Interestingly, the belief that the cuprate superconductivity is related to spin-fluctuations in the  $\text{CuO}_2$  planes has been gaining increasing support [84–86]. Therefore, the process by which doped hole carriers are introduced into the  $\text{CuO}_2$  plane is crucial for understanding the origin of the cuprate superconductivity. However, the LDA and GGA approximations are not capable of modeling the magnetic moments on the highly correlated Cu ions [87–94] but recent SCAN results have been very promising on various cuprates [29–31].

In this Chapter, I review how we have employed SCAN as a realistic tool to accurately describe the strongly correlated electronic structure of BSCCO with the copper magnetic moments. Using SCAN, we have gone beyond the standard simplified low-energy effective models, such as the one-band Hubbard model, and studied the effects of doping in a realistic manner, taking into account the impurity and

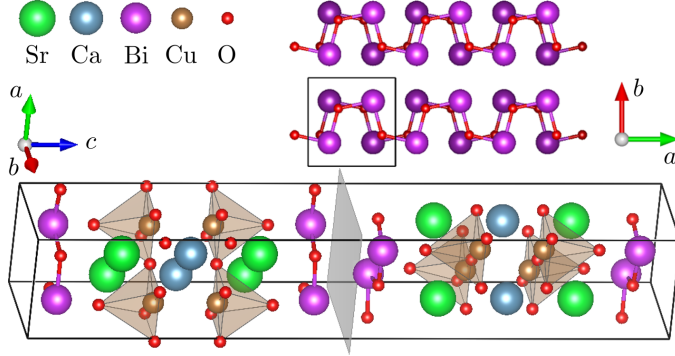


Figure 5.1: Our structural model of Bi2212 and the zigzag chains in the BiO bilayers. An orthorhombic  $\sqrt{2} \times \sqrt{2}$  supercell (SC) has been used to accommodate the AFM ordering and the BiO zigzag chains. The structure consists of two slabs shifted by a vector of  $(a/2, b/2, c/2)$  with respect to one another, and separated by a vdW layer (marked with the gray plane). The  $\sqrt{2} \times \sqrt{2}$  SC is illustrated with the black lines. From Publication III.

structural effects derived from real dopants. Our SCAN results show that the magnetic moments on the Cu ions persists when the sample is doped with oxygen, in accordance with resonant inelastic x-ray spectroscopy (RIXS) experiments [95–98].

## 5.2 Results

### 5.2.1 Pristine Bi2201 and Bi2212

As a starting point, we have considered undoped bulk Bi2201 and Bi2212. Energy cutoff was set to 550 eV. We relaxed the structures with  $k$ -mesh of  $9 \times 9 \times 2$  and analyzed the DOS and total energies with  $k$ -mesh of  $15 \times 15 \times 3$ . BSCCO can be approximated to have body-centered-tetragonal crystal structure, but it can be modeled more realistically as an orthorhombic  $\sqrt{2} \times \sqrt{2}$  supercell (SC), where the  $a$  and  $b$  axis are in 45 degree angle with respect to the Cu–O bonds. This structural model of Bi2212 is illustrated in Fig. 5.1. The BiO layers are under strong tensile stress due to a lattice mismatch, therefore the BiO layers are stretched and the Bi and O ions rearrange closer to each other, leading to formation of zigzag BiO chains or  $\text{Bi}_2\text{O}_2$  quadrilaterals [91, 99, 100]. We obtained good agreement with the experimental lattice constant especially in the case of Bi2212; our relaxed lattice parameters were  $5.35 \text{ \AA} \times 5.42 \text{ \AA} \times 31.08 \text{ \AA}$  in the  $a \times b \times c$  directions, while the experimental values are  $5.399(2) \text{ \AA} \times 5.414(1) \text{ \AA} \times 30.904(16) \text{ \AA}$  [69]. The lattice constant  $a$  is smaller than  $b$  because the bonding in the BiO layer is stronger in the  $a$ -direction than in the  $b$ -direction due to the zigzag chains. Therefore the BiO layers (which are under tensile stress) are capable of contradicting the  $a$ -axis more. For Bi2201, the lattice constants ( $5.29 \text{ \AA} \times 5.40 \text{ \AA} \times 24.82 \text{ \AA}$ ) are only in reasonable

agreement with the experimental values of  $5.376(1) \text{ \AA} \times 5.383(1) \text{ \AA} \times 24.384(7) \text{ \AA}$  [101]. Most notably the relaxed structure has stronger elongation in the  $ab$ -plane than in the experiment. This detail could be caused by the fact that the stress originating from the BiO layers disrupts the structure more in our Bi2201 model than in the Bi2212 model because the relative number of the BiO layers compared to other layers is higher in Bi2201 than in Bi2212. However, in the realistic samples some features we have not taken into account could relieve the stress in the BiO layers. Such details could be Pb doping or the incommensurate supermodulation that has an approximative period of five in the  $b$ -direction [102].

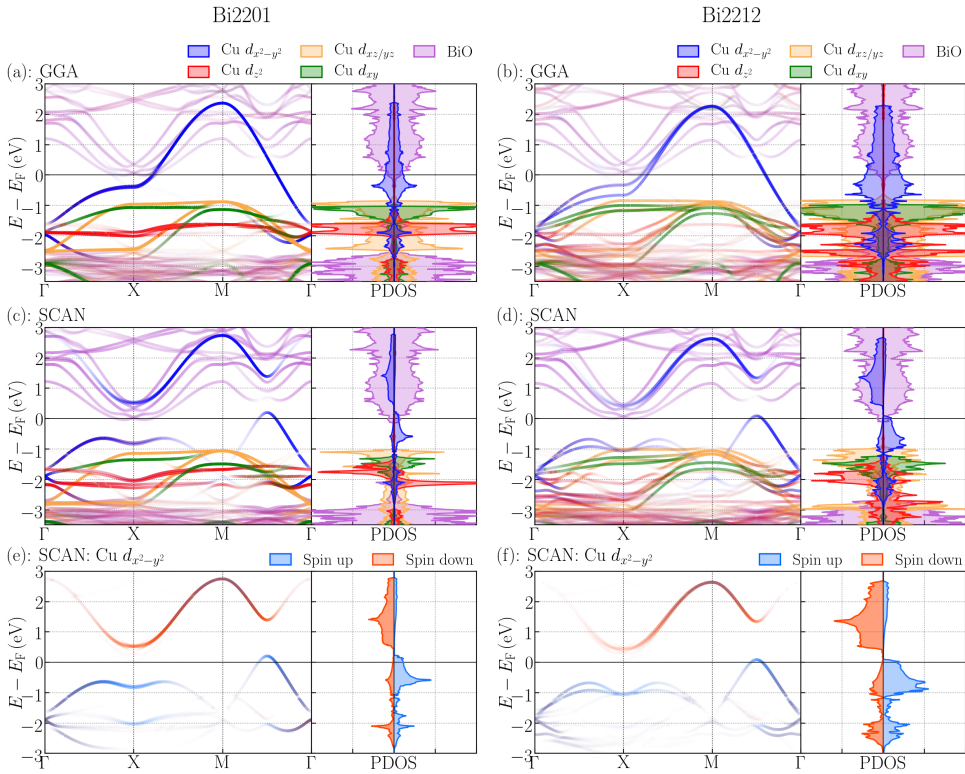


Figure 5.2: Electronic structure of Bi2201 (left) and Bi2212 (right). Panels (a) and (b) give the GGA band structure and DOS projected to Cu orbitals and BiO layers. Panels (c) and (d) contain the corresponding SCAN data. In these panels the Cu projections have been done to only those ions with positive magnetic moments in order to illustrate the spin polarization on them. However, the spin polarization is ignored in the band structure plots. Panels (e) and (f) give the SCAN band structure and DOS of the magnetic  $d_{x^2-y^2}$  orbitals. From Publication III.

Fig. 5.2 shows the results of our electronic structure calculations in the AFM  $\sqrt{2} \times \sqrt{2}$  SC, from where they have been unfolded [103, 104] to the primitive cell (PC). The special symmetry points  $X = (\pi/a, 0, 0)$  and  $M = (\pi/a, \pi/b, 0)$  have been given with respect to the PC Brillouin zone. In contrast to experimental results, GGA

[Fig. 5.2 (a)] yields spin-degenerate Cu  $d_{x^2-y^2}$  bands, which results in zero Cu magnetic moments. On the other hand, SCAN [Fig. 5.2 (b)] yields the experimentally observed AFM order over the copper atomic sites. Fig. 5.2 (c) illustrates the magnetic Cu  $d_{x^2-y^2}$  bands. The valence band (majority spin) is (partly) occupied, while the conduction band (minority spin) is unoccupied, leading to local magnetic moments of  $\pm 0.395 \mu_B$  and  $\pm 0.425 \mu_B$  per copper for Bi2201 and Bi2212, respectively. In the case of Bi2212, the electronic gap is equal to 0.33 eV in the half-filled  $d_{x^2-y^2}$  band. At  $X$  the energy gap is 1.416 eV, and at the midpoint between  $M$  and  $\Gamma$  the gap is 1.223 eV (these points are given with respect to the primitive cell Brillouin zone, and in the supercell BZ these points corresponds to the  $X$ -point and  $M$ -point, respectively). The valence band has a bilayer splitting of 0.23 eV around  $X$ , leading to two van Hove singularities in the PDOS at about  $-0.65$  eV and  $-0.85$  eV. These van Hove singularities appear stronger than logarithmic by visual inspection, in agreement with Nieminen *et al.* [81]. The results for Bi2201 are very similar, with an exception of Bi2201 not having bilayer splitting.

The  $d_{xz/yz}$  and  $d_{xy}$  bands are very similar and nearly degenerate, while the  $d_{z^2}$  bands are strongly split by Hund's splitting. The  $d_{z^2}$  bands are below the  $t_{2g}$  bands, in contrast to for example  $\text{La}_2\text{CuO}_4$ , where the  $d_{z^2}$  bands are the highest fully occupied ones [29]. This difference between Bi2212 and  $\text{La}_2\text{CuO}_4$  due to the fact that in Bi2212 the separation between the Cu ions and the apical oxygen atoms is larger (2.64–2.65 Å in our relaxed structure) than in  $\text{La}_2\text{CuO}_4$  (2.45 Å [29]). In order to estimate the on-site Hubbard potential  $U$  and the Hund's coupling  $J_H$ , we follow a scheme based on analysis of site-projected and orbitally resolved PDOS  $g_{\mu\sigma}$ . The average spin splitting,  $U$  and  $J_H$  are given by [29]

$$\bar{E}_{\mu\sigma} = \int_W E g_{\mu\sigma}(E) dE, \quad (5.1)$$

$$\bar{E}_{d_{x^2-y^2}\uparrow} - \bar{E}_{d_{x^2-y^2}\downarrow} = U(N_\uparrow - N_\downarrow), \quad (5.2)$$

$$\bar{E}_{\mu \neq d_{x^2-y^2}\uparrow} - \bar{E}_{\mu \neq d_{x^2-y^2}\downarrow} = J_H(N_\uparrow - N_\downarrow), \quad (5.3)$$

where  $N_\uparrow$  ( $N_\downarrow$ ) is the occupation of the spin-up (down)  $d_{x^2-y^2}$  state.  $W$  refers to the full bandwidth. Using these formulae,  $U$  is found to be 4.7 eV for both Bi2201 and Bi2212. The Hund's splitting is found to be and 1.35 eV by using  $\mu = d_{z^2}$ . These results are very similar to those found in  $\text{La}_2\text{CuO}_4$  [29]. The determined  $U$  is comparable to that found in 3-band Hubbard models of cuprates, but substantially larger than the  $U$  of single-band Hubbard model, for both Bi2212 [105] and Bi2201 [97]. This is due to the over-simplified nature of the single-band model; the single band of the model is composed of Cu- $d_{x^2-y^2}$  and O- $p_x, p_y$  characters, effectively representing a  $\text{CuO}_2$  molecule instead of a pure  $d$ -state. Therefore, the  $U$  estimated with this model is partially screened by the O ligands.

Using calculated values of  $U$  and by fitting a hopping parameter  $t$  to our bandstructure, we can estimate the nearest-neighbor the super-exchange coupling parameter  $J$ . Since  $J = 4t^2/U - 24t^4/U^3$ , we find the exchange coupling to be about 200 meV, if we estimate  $t \approx 500$  meV from the bandwidth. This value is in reasonable agreement with the experimental value  $J \sim 148$  meV [97]. Unlike in other undoped cuprates

such as  $\text{La}_2\text{CuO}_4$ , bulk magnetic BSCCO is weakly metallic due to self-doping [89]: the BiO bands cross below  $E_F$  near  $X$ , overlapping with the Cu  $d_{x^2-y^2}$  bands. This self-doping may be the reason it is so hard to stabilize a large magnetic gap in nominally undoped BSCCO.

In  $\text{La}_2\text{CuO}_4$ , Hund coupling leads to a substantial spin splitting of the Cu  $d_{z^2}$  orbitals, and a weaker splitting of the  $t_{2g}$  orbitals [29]. Similarly, in Bi2212 we find the main  $d_{z^2}$  weight peaks reside between  $-1.6$  and  $-2.0$  eV for the spin up channel, and between  $-2.7$  and  $-3.2$  eV for the spin down channel, whereas the  $d_{xz}/d_{yz}$  and  $d_{xy}$  bands are very similar and nearly degenerate, the highest  $d_{xz}/d_{yz}$  bands laying between  $-1.7$  eV and  $-1.0$  eV, and the highest  $d_{xy}$  bands laying between  $-2.0$  eV and  $-1.3$  eV, with very weak spin splitting. Notably, the energy ordering of the  $d$  orbitals is different from that found in of  $\text{La}_2\text{CuO}_4$  [29], where the  $d_{z^2}$  bands are the highest occupied ones, whereas in Bi2212 they are below the  $d_{xz}/d_{yz}$  and  $d_{xy}$  bands. This difference between Bi2212 and  $\text{La}_2\text{CuO}_4$  is a consequence of a larger separation between the Cu ions and the apical oxygen atoms in Bi2212 ( $2.64$ – $2.65$  Å in our relaxed structure) and  $\text{La}_2\text{CuO}_4$  ( $2.45$  Å [29]).

We also studied the dispersion in the  $z$  direction by looking along the  $(0, 0, 0) - (0, 0, \frac{\pi}{2})$  and  $(\frac{\pi}{2}, \frac{\pi}{2}, 0) - (\frac{\pi}{2}, \frac{\pi}{2}, \frac{\pi}{2})$  paths in the BZ (in the AFM  $\sqrt{2} \times \sqrt{2}$  SC) but no significant dispersion was found. Therefore Bi2212 appears to be prominently two-dimensional material, as suggested by the existence of the vdW gap between the BiO planes.

The main difference is given by a stronger self-doping than in Bi2212 since in Bi2201 the Bi/Cu ratio is twice as large.

### 5.2.2 Doping of Bi2212

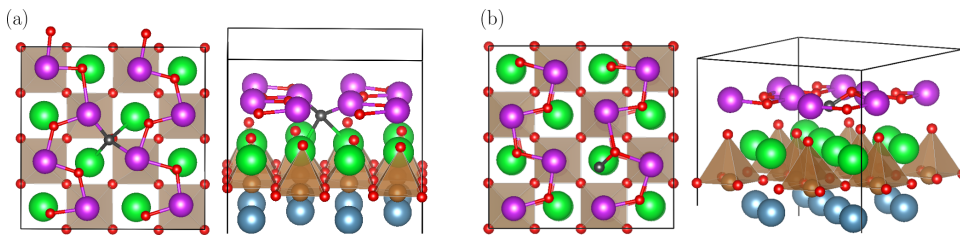


Figure 5.3: Top and side views of the relaxed slab structures of (a): type A and (b): type B interstitial oxygen atoms. From Publication III.

We have performed a realistic study of the electronic structure of doped Bi2212 by placing an interstitial oxygen atom  $\text{O}_{\text{int}}$  in a large 120-atom  $2\sqrt{2} \times 2\sqrt{2}$  SC, as illustrated in Fig. 5.3. In order to simplify the computational unit cell, we have employed a slab model with only one formula unit in the  $c$  direction (half of the unit cell pictured in Fig. 5.1), similarly with Refs. [90, 92, 106]. In order to simulate the bulk, we used only a small vacuum region of  $3.8$  Å to separate the periodic images. We verified that the band structure of the slab model closely corresponds to that of

the bulk. Our structures corresponds to a doping level of  $\delta = 1/8$ , which is close to the optimal doping. Due to the relatively complex multilayer structure of BSCCO, the oxygen impurities can occupy different sites, unlike for example in Hg–Ba–Ca–O and Y–Ba–Cu–O cuprates. The STM studies of Zeljkovic *et al.* [106, 107] and *ab initio* studies of He *et al.* [90, 91], have revealed two main interstitial impurity types labeled as “type A” and “type B”. The type A dopants reside close to the Sr layer, between the apical oxygen atoms, which enables direct interaction with the the CuO<sub>2</sub> plane. The structure used to model the type A doping is illustrated in Fig. 5.3 (a), and it is in excellent agreement with the recent scanning transmission electron microscopy (STEM) study by Song *et al.* [94]. The type B O<sub>int</sub> atoms lie within the BiO layers and combine with another O atom to form a dimer, as shown in Fig. 5.3 (b). The bond distance of this O dimer was found to be 1.467 Å, which is in good accord with the [O<sub>2</sub>]<sup>2-</sup> bond length in BaO<sub>2</sub> (1.49 Å) [108]. The total energy of the relaxed type A structure was found to be 2.25 eV lower than that of the type B structure. We also tested a structure, where the O<sub>int</sub> is placed to the vdW gap between the BiO layers, and we found its energy to be in between the type A and type B configurations. However, this position has not been discussed in the literature. A possible explanation is that these impurities disappear in the annealing process.

The electronic structure of the type A and B-doped structures is illustrated in Fig. 5.4. Comparison of the pristine case (left panels) to the type A and type B-doped cases (middle and right panels, respectively) reveals that the type A impurities explain most of the hole doping behavior, which is visible in particular in the lowering of the Fermi level. The shift in  $E_F$  is visible in particular for the  $d_{x^2-y^2}$  orbital of Cu(1), which denotes the copper ion closest to the O<sub>int</sub>, as shown in Fig. 5.4 (a). For the type B doping, the shifting of  $E_F$  is barely visible. Accordingly, the average magnitude of the Cu magnetic moments is reduced only by 0.014  $\mu_B$  in the type B configuration, whereas in the case of the type A doping,  $|\overline{M}|$  is equal to 0.347  $\mu_B$ , which corresponds to a reduction of 0.069  $\mu_B$ . There is significant difference in  $|M|$  between the two CuO<sub>2</sub> planes. Hereby, we refer to the CuO<sub>2</sub> layers with/without the dopant as “*doped/undoped CuO planes*”, respectively. On the undoped plane  $|M| = 0.363 \mu_B$ , whereas on the doped plane  $|M| = 0.331 \mu_B$ , and also the individual Cu ions have varying values of  $|M|$ . For Cu(1) this value is the highest ( $|M| = 0.343 \mu_B$ ), but the lowest magnetic moment is 0.323  $\mu_B$ .

The direct interactions between O<sub>int</sub> and Cu(1) happen through the  $p_z$  orbitals of the apical oxygen atoms O<sub>apical</sub>(1) and O<sub>apical</sub>(2). Interestingly, without doping, the interaction between Cu(1) and O<sub>apical</sub>(1) is negligible, which is evident due to lack of common features between Cu(1)  $d_{z^2}$  and O<sub>apical</sub>(1)  $p_z$  PDOSs in left panels of Figs. 5.4 (a) and 5.4 (b). This interaction is smaller in BSCCO than in other cuprates due to the larger separation between them. However, the addition of a type A interstitial decreases the Cu–O<sub>apical</sub> separation from 2.61 Å/2.65 Å to 2.479 Å/2.511 Å for O<sub>apical</sub>(1)/O<sub>apical</sub>(2), respectively. Accordingly, the coupling between these atoms experiences remarkable enhancement, which leads to interaction between O<sub>int</sub> and Cu(1) via O<sub>apical</sub>. This interaction is visible in the middle panels of Figs. 5.4 (a) and 5.4 (b), where Cu(1)  $d_{z^2}$ , O<sub>apical</sub>(1)  $p_z$  and O<sub>int</sub> all have clearly matching PDOS

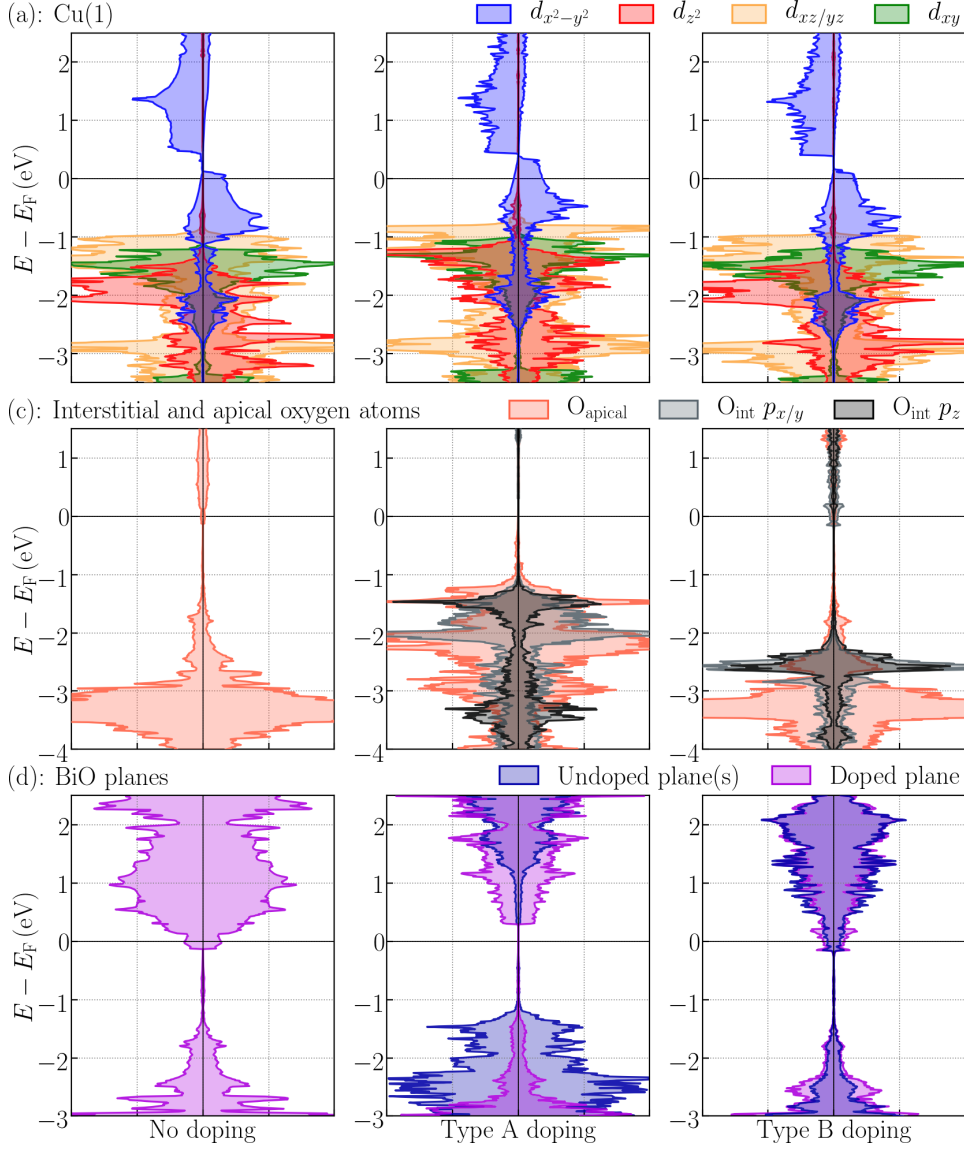


Figure 5.4: Site-resolved and orbitally projected PDOS for (a): the Cu(1) ion, i.e., the copper ion closest to the  $O_{\text{int}}$  (b): the  $O_{\text{apical}}$ (1) atom and  $O_{\text{int}}$  (c): the BiO layers. The first column presents undoped Bi2212 as a reference, the middle column contains data for type A-doped Bi2212, and the right column contains the results for type B impurities. From Publication III.

features. The effect of this interaction on the electronic structure of Cu(1) is to lift the  $d_{z^2}$  orbitals approximately 0.2 eV with respect to other  $d$  orbitals, and also substantially modify the shape of the  $d_{z^2}$  PDOS. However, the Hund's splitting (which was calculated to be 1.36 eV) is not affected. Interestingly, we observe that  $O_{\text{int}}$  PDOS features a  $p_z$  peak at  $-1.4$  eV, which coincides with the reported STM signal peak at  $-1.5$  eV [106, 107]. This observation can be explained by the  $p_{x/y}$  orbitals being orthogonal to the STM tip, leading the transmission to take place particularly through the  $O_{\text{int}}$   $p_z$  orbital [109].

The type A doping also removes the Bi pocket below  $E_F$ , as shown in Fig. 5.4 (c). This behavior has been observed before with LSDA [89], and also with GGA in a Pb-doping study in Bi2223 [93]. The BiO pockets are removed on both doped and undoped BiO planes, but the doping effects are substantially stronger for the doped BiO plane, where the BiO bands are lifted over 1 eV more than in the undoped BiO plane. In the case of type B doping, the Bi pockets are not affected as well.

We have also placed two type A  $O_{\text{int}}$  to the structure, as far as possible from each other. This doping corresponds to  $\delta = 1/4$  (heavy overdoping of Bi2212). The average magnetic moments are  $0.268 \mu_B$ , which is  $0.079 \mu_B$  less than in the case of just one impurity. Remarkably, in this case the system undergoes a transition to a ferrimagnetic ordering of the Cu ions, as the spin up (down) copper atoms have  $M = +0.307 \mu_B$  ( $M = -0.229 \mu_B$ ), respectively). Also each oxygen atom in the  $\text{CuO}_2$  planes get a magnetic moment of  $+0.010 \mu_B$ , and the whole SC obtains a macroscopic magnetization equal to  $0.059 \mu_B$  per Cu ion. Interestingly, the onset of the macroscopic magnetization has been proposed to suppress superconductivity in overdoped cuprates [110–112].

### 5.3 Conclusion

Our results for pristine and doped BSCCO reveal persistent antiferromagnetically coupled magnetic moments on the Cu ions, in agreement with RIXS experiments. We have not introduced any external parameters such as Hubbard  $U$  to our SCAN simulations to depict this Coulomb correlation effect, while the reference GGA calculations failed to capture it. Previous SCAN investigations on cuprates have observed the same trend [29–31]. Moreover, the SCAN results yield accurate lattice geometries, as opposed to GGA results. Furthermore, our SCAN simulations verify the experimentally observed appearance of macroscopic magnetization in overdoped samples, which is responsible for the suppression of superconductivity in this region of the BSCCO phase diagram. Our results show that the SCAN XC functional is an effective tool for modeling BSCCO and in general the family of cuprate superconductors, and can help rationalizing microscopic origin of the high-temperature superconductivity in these complex and strongly correlated materials, for example the recent observation of pressure-induced higher temperature superconductivity in BSCCO [113].

## CONCLUSION AND OUTLOOK

The DFT formalism has been widely used in computations of the electronic structure in condensed matter for more than half a century. Ideally, one would like to construct DFT implementations that include both exchange and correlation effects adequately, thus making it possible to obtain information on total energy, magnetism and other ground state properties. Nowadays, the most popular DFT scheme is GGA, in which the local exchange-correlation energy per particle at a given point depends only on the density and its gradient at that point. In some materials, the description of the interplay of local magnetic moments with itinerant electrons is a difficult test for GGA. As a matter of fact, a realistic modeling of competing phases in complex quantum materials has proven extremely challenging within the GGA. For example, much of the traditional GGA framework fails to describe the magnetic ground state of elemental manganese, which is a key ingredient in some magnetic shape memory alloys. A similar situation exists for high temperature cuprate superconductors. Beyond-DFT methods such as DFT+ $U$  are able to cure some of these problems but contain external parameters that can compromise the predictability of these methods. We have found that a parameter-free and efficient method to simulated exchange-correlation energy in complex materials is provided by SCAN meta-GGA. By deploying the new SCAN approach, I studied how landscapes of competing magnetic solutions can model nanoscale heterogeneity in materials such as decorated graphene with carbon adatoms, elemental manganese and BSCCO. Notably, our calculations confirm that Coulomb correlation effects are important in elemental manganese confirming previous DFT+ $U$  studies. I also checked that in decorated graphene with carbon adatoms the SCAN corrections are not so crucial as in strongly correlated materials like BSCCO. Moreover, I have examined the importance of charge, spin and lattice degrees of freedom to stabilize the various phases of a bismuth-based high-temperature superconductor by comparing the calculated results to highly resolved spectroscopy based on STM, ARPES and RIXS. The mastery in calculating exchange and correlation effects with the meta-GGA SCAN method encourages us to use DFT to study the nature of the electronic structure of magnetic functional materials. Therefore, this research provides not only an understanding on how magnetic phases stabilize but also form computational foundations of a better control of nanoscale hybrid devices for magnetic and superconducting quantum technologies.



## REFERENCES

- [1] A. Lichtenstein. “Chapter 5: Magnetism: From Stoner to Hubbard”. In: *Emergent Phenomena in Correlated Matter*. Deutsche Nationalbibliothek, 2013.
- [2] W. Kohn, *Rev. Mod. Phys.*, **71**, 1253–1266, (1999).
- [3] J. P. Perdew, K. Burke, and M. Ernzerhof, *Phys. Rev. Lett.*, **77**, 3865–3868, (1996).
- [4] J. Sun, A. Ruzsinszky, and J. P. Perdew, *Phys. Rev. Lett.*, **115**, 036402, (2015).
- [5] C. Gong and X. Zhang, *Science*, **363**, (2019).
- [6] V. Shukla, *Nanoscale Adv.*, **2**, 962–990, (2020).
- [7] Y. Deng, Y. Yu, Y. Song, J. Zhang, N. Z. Wang, Z. Sun, Y. Yi, Y. Z. Wu, S. Wu, J. Zhu, et al., *Nature*, **563**, 94–99, (2018).
- [8] V. D. Buchelnikov, V. V. Sokolovskiy, O. N. Miroshkina, M. A. Zagrebin, J. Nokelainen, A. Pulkkinen, B. Barbiellini, and E. Lähderanta, *Phys. Rev. B*, **99**, 014426, (2019).
- [9] D. Hobbs and J. Hafner, *J. Phys. Condens. Matter*, **13**, L681–L688, (2001).
- [10] D. Hobbs, J. Hafner, and D. Spišák, *Phys. Rev. B*, **68**, 014407, (2003).
- [11] J. Hafner and D. Hobbs, *Phys. Rev. B*, **68**, 014408, (2003).
- [12] H. Ehteshami and P. A. Korzhavyi, *Phys. Rev. Materials*, **1**, 073803, (2017).
- [13] H. Ehteshami and A. V. Ruban, *Phys. Rev. Mater.*, **2**, 034405, (2018).
- [14] S. Lee, C. Leighton, and F. S. Bates, *PNAS*, **111**, 17723–17731, (2014).
- [15] A. I. Kolesnikov, A. Podlesnyak, R. A. Sadykov, V. E. Antonov, M. A. Kuzovnikov, G. Ehlers, and G. E. Granroth, *Phys. Rev. B*, **94**, 134301, (2016).
- [16] E. Sterpetti, J. Biscaras, A. Erb, and A. Shukla, *Nat. Commun.*, **8**, 1–8, (2017).
- [17] G. Kresse and J. Furthmüller, *Comput. Mater. Sci.*, **6**, 15–50, (1996).
- [18] G. Kresse and J. Furthmüller, *Phys. Rev. B*, **54**, 11169–11186, (1996).
- [19] J. Sun, J. W. Furness, and Y. Zhang. “Chapter 4: Density functional theory”. In: *Mathematical Physics in Theoretical Chemistry*. Ed. by S. Blinder and J. House. Developments in Physical & Theoretical Chemistry. Elsevier, 2019, pp. 119–159.
- [20] P. Hohenberg and W. Kohn, *Phys. Rev.*, **136**, B864–B871, (1964).

- [21] R. van Leeuwen. “Density Functional Approach to the Many-Body Problem: Key Concepts and Exact Functionals”. In: vol. 43. *Advances in Quantum Chemistry*. Academic Press, 2003, pp. 25–94.
- [22] Y. Yao and Y. Kanai, *J. Chem. Phys.*, **146**, 224105, (2017).
- [23] N. Troullier and J. L. Martins, *Phys. Rev. B*, **43**, 1993–2006, (1991).
- [24] G. B. Bachelet, D. R. Hamann, and M. Schlüter, *Phys. Rev. B*, **26**, 4199–4228, (1982).
- [25] S. G. Louie, S. Froyen, and M. L. Cohen, *Phys. Rev. B*, **26**, 1738–1742, (1982).
- [26] P. E. Blöchl, *Phys. Rev. B*, **50**, 17953–17979, (1994).
- [27] G. Kresse and D. Joubert, *Phys. Rev. B*, **59**, 1758–1775, (1999).
- [28] R. Car, *Nat. Chem.*, **8**, 820, (2016).
- [29] C. Lane, J. W. Furness, I. G. Buda, Y. Zhang, R. S. Markiewicz, B. Barbiellini, J. Sun, and A. Bansil, *Phys. Rev. B*, **98**, 125140, (2018).
- [30] J. W. Furness, Y. Zhang, C. Lane, I. G. Buda, B. Barbiellini, R. S. Markiewicz, A. Bansil, and J. Sun, *Commun. Phys.*, **1**, 11, (2018).
- [31] Y. Zhang, C. Lane, J. W. Furness, B. Barbiellini, J. P. Perdew, R. S. Markiewicz, A. Bansil, and J. Sun, *Proc. Natl. Acad. Sci.*, **117**, 68–72, (2020).
- [32] C. Huang, J. Zhou, K. Deng, E. Kan, and P. Jena, *J. Phys. Chem. A*, **122**, 4350–4356, (2018).
- [33] A. I. Liechtenstein, V. I. Anisimov, and J. Zaanen, *Phys. Rev. B*, **52**, R5467–R5470, (1995).
- [34] S. L. Dudarev, G. A. Botton, S. Y. Savrasov, C. J. Humphreys, and A. P. Sutton, *Phys. Rev. B*, **57**, 1505–1509, (1998).
- [35] M. Cococcioni and S. de Gironcoli, *Phys. Rev. B*, **71**, 035105, (2005).
- [36] C. Ricca, I. Timrov, M. Cococcioni, N. Marzari, and U. Aschauer, *Phys. Rev. B*, **99**, 094102, (2019).
- [37] P. O. Lehtinen, A. S. Foster, A. Ayuela, A. Krasheninnikov, K. Nordlund, and R. M. Nieminen, *Phys. Rev. Lett.*, **91**, 017202, (2003).
- [38] R. Singh and P. Kroll, *J. Phys. Condens. Matter*, **21**, 196002, (2009).
- [39] X. F. Fan, L. Liu, R. Q. Wu, G. W. Peng, H. M. Fan, Y. P. Feng, J.-L. Kuo, and Z. X. Shen, *J. Phys. Condens. Matter*, **22**, 046001, (2010).
- [40] I. C. Gerber, A. V. Krasheninnikov, A. S. Foster, and R. M. Nieminen, *New J. Phys.*, **12**, 113021, (2010).
- [41] Y. G. Zhou, Z. G. Wang, P. Yang, X. T. Zu, H. Y. Xiao, X. Sun, M. A. Khaleel, and F. Gao, *Phys. Chem. Chem. Phys.*, **13**, 16574, (2011).
- [42] C. Ataca, E. Aktürk, H. Şahin, and S. Ciraci, *J. Appl. Phys.*, **109**, 013704, (2011).

- [43] S. Kim, D. D. Kulkarni, R. Davis, S. S. Kim, R. R. Naik, A. A. Voevodin, M. Russell, S. S. Jang, V. V. Tsukruk, and A. G. Fedorov, *ACS Nano*, **8**, 6805–6813, (2014).
- [44] F. Banhart, J. Kotakoski, and A. V. Krasheninnikov, *ACS Nano*, **5**, 26–41, (2011).
- [45] H. González-Herrero, J. M. Gómez-Rodríguez, P. Mallet, M. Moaied, J. J. Palacios, C. Salgado, M. M. Ugeda, J.-Y. Veullen, F. Yndurain, and I. Brihuega, *Science*, **352**, 437–441, (2016).
- [46] E. H. Lieb, *Phys. Rev. Lett.*, **62**, 1201–1204, (1989).
- [47] S. R. Power and M. S. Ferreira, *Crystals*, **3**, 49–78, (2013).
- [48] E. Pavarini, E. Koch, and U. Schollwöck, *Emergent Phenomena in Correlated Matter*, Deutsche Nationalbibliothek, 2013.
- [49] J. Tuček, P. Błoński, J. Ugolotti, A. K. Swain, T. Enoki, and R. Zbořil, *Chem. Soc. Rev.*, **47**, 3899–3990, (2018).
- [50] K. T. Chan, H. Lee, and M. L. Cohen, *Phys. Rev. B*, **83**, 035405, (2011).
- [51] K. T. Chan, H. Lee, and M. L. Cohen, *Phys. Rev. B*, **84**, 165419, (2011).
- [52] A. M. Suarez, L. R. Radovic, E. Bar-Ziv, and J. O. Sofo, *Phys. Rev. Lett.*, **106**, 146802, (2011).
- [53] J. O. Sofo, A. M. Suarez, G. Usaj, P. S. Cornaglia, A. D. Hernández-Nieves, and C. A. Balseiro, *Phys. Rev. B*, **83**, 081411, (2011).
- [54] I. A. Pašti, A. Jovanović, A. S. Dobrota, S. V. Mentus, B. Johansson, and N. V. Skorodumova, *Appl. Surf. Sci.*, **436**, 433–440, (2018).
- [55] C. Ataca and S. Ciraci, *Phys. Rev. B*, **83**, 235417, (2011).
- [56] D. M. Edwards and M. I. Katsnelson, *J. Phys. Condens. Matter*, **18**, 7209–7225, (2006).
- [57] A. Proutt and P. Donnadieu, *Philos. Mag. Lett.*, **72**, 337–344, (1995).
- [58] J. Kübler, *Theory of itinerant electron magnetism*, International series of monographs on physics. Oxford University Press, 2009.
- [59] T. Asada and K. Terakura, *Phys. Rev. B*, **47**, 15992–15995, (1993).
- [60] Y. Endoh and Y. Ishikawa, *J. Phys. Soc. Jap.*, **30**, 1614–1627, (1971).
- [61] R. Podloucky and J. Redinger, *J. Phys. Condens. Matter*, **31**, 054001, (2018).
- [62] I. Di Marco, J. Minár, S. Chadov, M. I. Katsnelson, H. Ebert, and A. I. Lichtenstein, *Phys. Rev. B*, **79**, 115111, (2009).
- [63] I. Di Marco, J. Minár, J. Braun, M. I. Katsnelson, A. Grechnev, H. Ebert, A. I. Lichtenstein, and O. Eriksson, *Eur. Phys. J. B*, **72**, 473–478, (2009).
- [64] S. Biermann, A. Dallmeyer, C. Carbone, W. Eberhardt, C. Pampuch, O. Rader, M. I. Katsnelson, and A. I. Lichtenstein, *JETP Lett.*, **80**, 612–615, (2004).
- [65] H. Fujihisa and K. Takemura, *Phys. Rev. B*, **52**, 13257–13260, (1995).

- [66] A. C. Lawson, A. C. Larson, M. C. Aronson, S. Johnson, Z. Fisk, P. C. Canfield, J. D. Thompson, and R. B. Von Dreele, *J. Appl. Phys.*, **76**, 7049, (1994).
- [67] Y. Dedkov, E. Voloshina, and M Richter, *Phys. Rev. B*, **81**, 085404, (2010).
- [68] D. Mejía-Rodríguez and S. B. Trickey, *Phys. Rev. B*, **100**, 041113, (2019).
- [69] M. A. Subramarian, C. C. Torardi, J. C. Calabrese, J. Gopalakrishnan, K. J. Morrissey, T. R. Askew, R. B. Flippin, U. Chowdhry, and A. W. Sleight, *Science*, **239**, 1015–1017, (1988).
- [70] J. M. Tarascon, Y. LePage, L. H. Greene, B. G. Bagley, P. Barboux, D. M. Hwang, G. W. Hull, W. R. McKinnon, and M. Giroud, *Phys. Rev. B*, **38**, 2504–2508, (1988).
- [71] J. M. Tarascon, W. R. McKinnon, P. Barboux, D. M. Hwang, B. G. Bagley, L. H. Greene, G. W. Hull, Y. LePage, N. Stoffel, and M. Giroud, *Phys. Rev. B*, **38**, 8885–8892, (1988).
- [72] N. L. Saini, J. Avila, A. Bianconi, A. Lanzara, M. C. Asensio, S. Tajima, G. D. Gu, and N. Koshizuka, *Phys. Rev. Lett.*, **79**, 3467–3470, (1997).
- [73] H. Ding, J. R. Engelbrecht, Z. Wang, J. C. Campuzano, S.-C. Wang, H.-B. Yang, R. Rogan, T. Takahashi, K. Kadowaki, and D. G. Hinks, *Phys. Rev. Lett.*, **87**, 227001, (2001).
- [74] K. M. Lang, V. Madhavan, J. E. Hoffman, E. W. Hudson, H. Eisaki, S. Uchida, and J. C. Davis, *Nature*, **415**, 412–416, (2002).
- [75] A. Damascelli, Z. Hussain, and Z.-X. Shen, *Rev. Mod. Phys.*, **75**, 473–541, (2003).
- [76] T. L. Miller, M. Ärrälä, C. L. Smallwood, W. Zhang, H. Hafiz, B. Barbiellini, K. Kurashima, T. Adachi, Y. Koike, H. Eisaki, M. Lindroos, A. Bansil, D.-H. Lee, and A. Lanzara, *Phys. Rev. B*, **91**, 085109, (2015).
- [77] K. Gotlieb, C.-Y. Lin, M. Serbyn, W. Zhang, C. L. Smallwood, C. Jozwiak, H. Eisaki, Z. Hussain, A. Vishwanath, and A. Lanzara, *Science*, **362**, 1271–1275, (2018).
- [78] B. Barbiellini, O. Fischer, M. Peter, C. Renner, and M. Weger, *Physica C*, **220**, 55–60, (1994).
- [79] K. McElroy, R. W. Simmonds, J. E. Hoffman, D.-H. Lee, J. Orenstein, H. Eisaki, S. Uchida, and J. C. Davis, *Nature*, **422**, 592–596, (2003).
- [80] O. Fischer, M. Kugler, I. Maggio-Aprile, C. Berthod, and C. Renner, *Rev. Mod. Phys.*, **79**, 353–419, (2007).
- [81] J. Nieminen, I. Suominen, T. Das, R. S. Markiewicz, and A. Bansil, *Phys. Rev. B*, **85**, 214504, (2012).
- [82] P. Mistark, R. S. Markiewicz, and A. Bansil, *Phys. Rev. B*, **91**, 140501, (2015).
- [83] J. M. Tranquada, G. Xu, and I. A. Zaliznyak, *Journal of Magnetism and Magnetic Materials*, **350**, 148–160, (2014).

- [84] D. J. Scalapino, E. Loh, and J. E. Hirsch, *Phys. Rev. B*, **34**, 8190–8192, (1986).
- [85] D. J. Scalapino, *Phys. Rep.*, **250**, 329–365, (1995).
- [86] D. J. Scalapino, *Rev. Mod. Phys.*, **84**, 1383–1417, (2012).
- [87] S. Massidda, J. Yu, and A. Freeman, *Physica C: Superconductivity*, **152**, 251–258, (1988).
- [88] M. S. Hybertsen and L. F. Mattheiss, *Phys. Rev. Lett.*, **60**, 1661–1664, (1988).
- [89] H. Lin, S. Sahrakorpi, R. S. Markiewicz, and A. Bansil, *Phys. Rev. Lett.*, **96**, 097001, (2006).
- [90] Y. He, T. S. Nunner, P. J. Hirschfeld, and H.-P. Cheng, *Phys. Rev. Lett.*, **96**, 197002, (2006).
- [91] Y. He, S. Graser, P. J. Hirschfeld, and H.-P. Cheng, *Phys. Rev. B*, **77**, 220507, (2008).
- [92] K. Foyevtsova, H. C. Kandpal, H. O. Jeschke, S. Graser, H.-P. Cheng, R. Valentí, and P. J. Hirschfeld, *Phys. Rev. B*, **82**, 054514, (2010).
- [93] J. Camargo-Martínez, D. Martínez-Pieschacón, and R. Baquero, *Physica C: Superconductivity and its Applications*, **535**, 34–39, (2017).
- [94] D. Song, X. Zhang, C. Lian, H. Liu, I. Alexandrou, I. Lazić, E. G. T. Bosch, D. Zhang, L. Wang, R. Yu, Z. Cheng, C. Song, X. Ma, W. Duan, Q. Xue, and J. Zhu, *Adv. Funct. Mater.*, **29**, 1903843, (2019).
- [95] M. Guarise, B. D. Piazza, H. Berger, E. Giannini, T. Schmitt, H. M. Rønnow, G. A. Sawatzky, J. van den Brink, D. Altenfeld, I. Eremin, and M. Gioni, *Nat. Commun.*, **5**, 5760, (2014).
- [96] Y. Y. Peng, M. Salluzzo, X. Sun, A. Ponti, D. Betto, A. M. Ferretti, F. Fumagalli, K. Kummer, M. Le Tacon, X. J. Zhou, N. B. Brookes, L. Braicovich, and G. Ghiringhelli, *Phys. Rev. B*, **94**, 184511, (2016).
- [97] Y. Y. Peng, G. Della, M. Minola, M. Conni, A. Amorese, D. Di Castro, G. M. De Luca, K. Kummer, M. Salluzzo, X. Sun, X. J. Zhou, G. Balestrino, M. Le Tacon, B. Keimer, L. Braicovich, N. B. Brookes, and G. Ghiringhelli, *Nat. Phys.*, **13**, 1201–1206.
- [98] Y. Y. Peng, E. W. Huang, R. Fumagalli, M. Minola, Y. Wang, X. Sun, Y. Ding, K. Kummer, X. J. Zhou, N. B. Brookes, B. Moritz, L. Braicovich, T. P. Devereaux, and G. Ghiringhelli, *Phys. Rev. B*, **98**, 144507, (2018).
- [99] W. Fan and Z. Zeng, *Supercond. Sci. Technol.*, **24**, 105007, (2011).
- [100] I. Zeljkovic, E. J. Main, T. L. Williams, M. C. Boyer, K. Chatterjee, W. D. Wise, Y. Yin, M. Zech, A. Pivonka, T. Kondo, T. Takeuchi, H. Ikuta, J. Wen, Z. Xu, G. D. Gu, E. W. Hudson, and J. E. Hoffman, *Nat. Mater.*, **11**, 585–589, (2012).
- [101] K. Imai, I. Nakai, T. Kawashima, S. Sueno, and A. Ono, *Jpn. J. Appl. Phys.*, **27**, L1661–L1664, (1988).

- 
- [102] N. Poccia, G. Campi, M. Fratini, A. Ricci, N. L. Saini, and A. Bianconi, *Phys. Rev. B*, **84**, 100504, (2011).
- [103] P. B. Allen, T. Berlijn, D. A. Casavant, and J. M. Soler, *Phys. Rev. B*, **87**, 085322, (2013).
- [104] P. V. C. Medeiros, S. Stafström, and J. Björk, *Phys. Rev. B*, **89**, 041407(R), (2014).
- [105] S.-L. Yang, J. A. Sobota, Y. He, Y. Wang, D. Leuenberger, H. Soifer, M. Hashimoto, D. H. Lu, H. Eisaki, B. Moritz, T. P. Devereaux, P. S. Kirchmann, and Z.-X. Shen, *Phys. Rev. B*, **96**, 245112, (2017).
- [106] I. Zeljkovic, J. Nieminen, D. Huang, T.-R. Chang, Y. He, H.-T. Jeng, Z. Xu, J. Wen, G. Gu, H. Lin, R. S. Markiewicz, A. Bansil, and J. E. Hoffman, *Nano Lett.*, **14**, 6749–6753, (2014).
- [107] I. Zeljkovic, Z. Xu, J. Wen, G. Gu, R. S. Markiewicz, and J. E. Hoffman, *Science*, **337**, 320–323, (2012).
- [108] L. Sutton, *Tables of Interatomic Distances and Configuration in Molecules and Ions*, London: The Chemical Society, 1958.
- [109] I. Suominen, J. Nieminen, R. S. Markiewicz, and A. Bansil, *Phys. Rev. B*, **84**, 014528, (2011).
- [110] K. Kurashima, T. Adachi, K. M. Suzuki, Y. Fukunaga, T. Kawamata, T. Noji, H. Miyasaka, I. Watanabe, M. Miyazaki, A. Koda, R. Kadono, and Y. Koike, *Phys. Rev. Lett.*, **121**, 057002, (2018).
- [111] A. Kopp, A. Ghosal, and S. Chakravarty, *PNAS*, **104**, 6123–6127, (2007).
- [112] B. Barbiellini and T. Jarlborg, *Phys. Rev. Lett.*, **101**, 157002, (2008).
- [113] L. Deng, Y. Zheng, Z. Wu, S. Huyan, H.-C. Wu, Y. Nie, K. Cho, and C.-W. Chu, *Proc. Natl. Acad. Sci. U.S.A.*, **116**, 2004–2008, (2019).

# Publication I

J. Nokelainen, I. V. Rozhansky, B. Barbiellini, E. Lähderanta and K. Pussi  
**Gate-tunable magnetism of C adatoms on graphene**

Reprinted with permission from  
*Physical Review B*  
Vol. 99, pp. 035441, 2019  
© 2019, American Physical Society.



**Gate-tunable magnetism of C adatoms on graphene**J. Nokelainen,<sup>1,\*</sup> I. V. Rozhansky,<sup>2,1</sup> B. Barbiellini,<sup>1,3</sup> E. Lähderanta,<sup>1</sup> and K. Pussi<sup>1</sup><sup>1</sup>*LUT University, P.O. Box 20, FI-53851, Lappeenranta, Finland*<sup>2</sup>*Ioffe Institute, 194021 St. Petersburg, Russia*<sup>3</sup>*Physics Department, Northeastern University, Boston, Massachusetts 02115, USA*

(Received 15 May 2018; revised manuscript received 18 December 2018; published 29 January 2019)

We have performed density functional theory calculations of graphene decorated with carbon adatoms, which bind at the bridge site of a C–C bond. Earlier studies have shown that the C adatoms have magnetic moments and have suggested the possibility of ferromagnetism with high Curie temperature. Here we propose to use a gate voltage to fine tune the magnetic moments from zero to  $1 \mu_B$  while changing the magnetic coupling from antiferromagnetism to ferromagnetism and again to antiferromagnetism. These results are rationalized within the Stoner and Ruderman-Kittel-Kasuya-Yosida (RKKY) models. When the SCAN meta-GGA (generalized gradient approximation) correction is used, the magnetic moments for zero gate voltage are reduced and the Stoner band ferromagnetism is slightly weakened in the ferromagnetic region.

DOI: 10.1103/PhysRevB.99.035441

**I. INTRODUCTION**

A functionalization of semiconductor devices with ferromagnetic properties is one of the greatest challenges of modern spintronics [1–3]. Much research is nowadays focused on incorporating magnetic properties into semiconductor system and, in particular, into graphene [4–18]. Graphene modified by defects is very promising for such purpose. Because of the reduced coordination number in the two-dimensional system, the defect states are naturally expected to have weak coupling to graphene, thus broadening of their energy levels is expected to be small and with high density of states (DOS). If the Fermi level ( $E_F$ ) further falls inside the broadened energy level, the Stoner instability [19] removes the spin degeneracy of the impurity states, leading to the onset of magnetization. Thus graphene can magnetize even first row element adatoms [20] producing two-dimensional  $d^0$  semiconductor magnetism. This kind of scenario becomes particularly interesting for external gate voltage ( $V_g$ ) control of the Fermi energy. In fact, the impurity state can be easily occupied/drained using  $V_g$  [21–23]. Consequently, a rich phenomenology emerges from the interplay between magnetic impurities and the gate-voltage control of the interactions. As we shall see in the next sections, the description of this interplay is rather complex and it has not been carefully examined in earlier studies. Experimentally gate-voltage control has been used for producing magnetism on graphene oxide [11], N-doped graphene oxide [16], and graphene grafted with Pt-porphyrins [14], revealing the existence of ferromagnetic phases with significant magnetic moments for particular values of  $V_g$ . The magnetic impurities develop a narrow band [19,24], which has been proposed to give rise to Stoner band ferromagnetism with high Curie temperatures even for  $sp$  electron systems [25]. Moreover, the indirect exchange interaction of impurities on

graphene has been intensively studied within the Ruderman-Kittel-Kasuya-Yosida (RKKY) framework [26–32] and the recently developed extension of this approach, which takes into account a resonant hybridization between the adatoms and graphene [33].

Most of the literature considers impurities interacting with one of the two sublattices  $A$  or  $B$  of graphene. The Lieb's theorem [34] for bipartite lattice applies for these cases. As a corollary of this theorem, two impurities connected to the same sublattice interact ferromagnetically, while the interaction is antiferromagnetic for impurities connected to different sublattices. This sublattice dependence has been verified by the various computational and experimental studies [13,18,35–37]. For adatoms, the situation depicted above corresponds to the top-site binding. However, the bridge site is in general energetically more favorable than the top site [20,38], despite the fact that it has not been studied as intensively. For example, for carbon adatom, the adsorption energies to top and hollow high-symmetry sites are 0.72 and 1.36 eV higher [39]. Interestingly, the magnetic interactions for bridge-site adatoms are different since coupling with both sublattices occurs, as pointed out by Gerber *et al.* for carbon adatoms [40]. In this situation, the Lieb's theorem does not apply anymore because the lattice is no more bipartite. These conditions are therefore more favorable for ferromagnetism within the C adatom network.

The carbon adatom [39–50] can be considered as an exemplar case for the bridge-site binding. It has only one partially filled magnetic orbital at about 0.3 eV below the graphene Dirac point ( $E_D$ ). Here, we name this orbital as  $\psi_{p,\perp}$  since it has  $p$  symmetry with its symmetry axis perpendicular to the C–C bond of the bridge site, as shown in Fig. 1. The  $\psi_{p,\perp}$  orbital hybridizes only weakly with the graphene backbone, thus it has high partial DOS and it preserves the Dirac cone shape. Therefore, the ideal model considering a localized state and a Dirac cone remains valid. Taking all these considerations into account, one can conclude that C adatoms

\*johannes.nokelainen@lut.fi

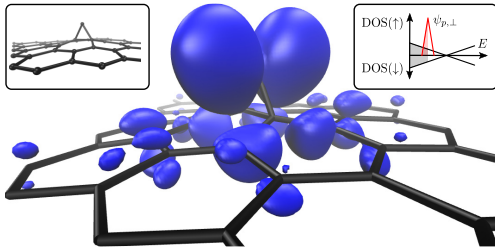


FIG. 1. Magnetization density isosurface plot for a C adatom on graphene. The isosurface is at  $0.004 e/\text{\AA}^3$ , while the corresponding negative isosurface is not visible. The  $\psi_{p,\perp}$  state (with  $p_x/p_y$  symmetry) is visible at the adatom. Its  $p_z$  character on the graphene sheet can be seen as well. (Left inset) Another view of the geometry. (Right inset) Schematic electronic structure, the occupied portion of the graphene/ $\psi_{p,\perp}$  states are in gray/red, respectively.

are interesting for both conceptual and applied purposes. Nevertheless, we must bear in mind that the controlled production of C adatom networks on graphene remains a major challenge. To address these difficulties, a recent paper by Kim *et al.* has suggested a facile pathway for the realization of this system [48]. In this study, the C adatoms have been monitored using a powerful Raman technique [51]. As documented by a recent review by Banhart *et al.* [50], another obstacle resides in the stability of the adatoms, which are mobile even at room temperature due to the rather low migration barrier of 0.35–0.60 eV [38,40,41,46,47,49,52]. Nevertheless, intrinsic weak ferromagnetism or superparamagnetism observed in graphite [53–59] implies that the defects producing this behavior couple to the both sublattices  $A$  and  $B$  as a corollary to the Lieb’s theorem. Such coupling yields magnetic properties similar to those produced by C adatoms.

The present paper provides a comprehensive theoretical study of graphene decorated with C adatoms and shows that the magnetic properties can be controlled with a gate voltage. The paper is organized as follows. Section II contains the methodology: Sec. II A gives the computational details, Sec. II B contains the used computational supercells, and Sec. II C discusses the theoretical framework. Section III reports the results of the study. Section III A focuses on effects of bias to a single adatom while Sec. III B presents the most important results of this study, which is the behavior of the magnetic interactions as a function of gate voltage for remote interaction distances and its interpretation. Section III C contains results for close interaction distances. Section III D illustrates the spatial spin polarization patterns induced in graphene by the  $\psi_{p,\perp}$  state. Section IV contains the conclusions and outlook of the present work.

## II. METHODOLOGY

### A. Computational details

The calculations were performed within the density functional theory (DFT) as implemented in the Vienna *ab initio* simulation package (VASP) [60,61]. DFT is in principle an exact many-body theory [62]. However, in practice, the

exchange-correlation (XC) functional taking into account the Pauli principle and Coulomb correlation effects contains approximations. To describe the XC functional, we used the generalized gradient approximation (GGA) in the form proposed by Perdew, Burke, and Ernzerhof (PBE) [63]. GGA is a correction to the old local density approximation, which in iron improves the stability of FM phase [64]. Moreover, a set of calculations were repeated with the strongly constrained and appropriately normed (SCAN) meta-GGA functional [65], which is a more precise XC scheme obeying the 17 known exact constraints. SCAN typically produces superior results compared to most GGA functionals [66–71] including the case of pure graphene,<sup>1</sup> and also our tests on different graphene adatoms<sup>2</sup> support this trend. Moreover, Black-Schaffer [29] has demonstrated that electron correlation effects play an important role in the coupling of magnetic impurity moments in graphene. Therefore, it is important to check the impact of correlation effect beyond the GGA. These important arguments have justified the deployment of the SCAN functional in our study.

The magnetic interactions between C adatoms were studied by placing two adatoms on a graphene supercell (SC) and by comparing the energies of the parallel and antiparallel adatom spin configurations, which we also refer to ferromagnetic (FM) and antiferromagnetic (AFM) solutions throughout the present paper. The energy difference  $\Delta E = E(\text{FM}) - E(\text{AFM})$  contains the information about magnetic interactions. The same SC methodology (using periodic boundary conditions) has been successful in describing experiments with interacting hydrogen adatoms on graphene [13].

The Kohn-Sham orbitals were expanded in a plane wave basis set with an energy cutoff of 600 eV. The electron-ion interactions were taken into account using the projector augmented wave (PAW) method [72,73] and the electronic energy minimization was performed with a tolerance of  $10^{-5}$  eV. Each structure was optimized until the residual forces became smaller than  $0.01$  eV/ $\text{\AA}$ . In these relaxation runs, we used first order Methfessel-Paxton smearing with width of 0.1 eV. The Brillouin zone was sampled with dense  $\Gamma$ -centered meshes with  $\mathbf{k}$ -point separations lower than  $0.017 \times 2\pi/\text{\AA}$ . For example, a  $4 \times 4 \times 1$  mesh was used for calculations on  $7 \times 7$  repeated graphene SCs and a  $4 \times 8 \times 1$  mesh was used for  $8 \times 4$  SCs. We found that the high  $k$ -point density is essential in describing the magnetic  $\psi_{p,\perp}$  state of the C adatom correctly. Some of these parameters were refined for the SCAN simulations (see Sec. 1.1 of Ref. [74]). To obtain more accurate total energies and DOS, the Methfessel-Paxton method was upgraded to the tetrahedron method with Blöchl corrections [75]. Moreover, the  $\mathbf{k}$ -point grids were increased to  $10 \times 10 \times 1$  mesh for  $N \times N$  SCs and  $8 \times 16 \times 1$  mesh for  $2N \times N$  SCs. As in earlier work [21,22,76,77], the gate voltage was modeled by adding  $\Delta Q/e$  electrons. In order to avoid divergence in the Ewald summation, the unit cell was

<sup>1</sup>Buda *et al.* [68] discuss the consistency between SCAN and quantum monte carlo results in the pure graphene.

<sup>2</sup>We have tested that, unlike PBE, SCAN is capable of finding the magnetic moment of F adatoms on graphene. Typically hybrid functionals are needed for this result [86].

kept charge neutral by adding a compensating jellium background charge. These computational schemes may produce errors as discussed in detail in Sec. 1.2 of Ref. [74]. Moreover, when  $\Delta Q \geq 1.5e$  and when the SCs are small, some charge spilling to the vacuum occurs. This problem was overcome by decreasing the unit cell height to 15 Å or even 13 Å from the standard value of 20 Å. The forementioned errors are increased by the decreasing of the unit cell height, but our results are not significantly affected by all these errors as explained in the Sec. 1.2 of Ref. [74].

### B. Studied configurations

We studied the magnetic interactions of the two adatoms  $C_1^{\text{ad}}$  and  $C_2^{\text{ad}}$  on a set of different geometrical configurations. These configurations are characterized by adatom orientations, graphene SCs (on which the adatoms are placed) and one-sided/two-sided adsorption sites, where the adatoms are adsorbed on the same/opposite sides of the graphene sheet. Two main configuration types were used, as explained by the following paragraphs.

In *adatom pair configurations*, the adatoms were placed close to each other. These configurations were used to model short range pairwise interactions as in the study by Gerber *et al.* [40]. The results for these pairs are discussed in Sec. III C. Eight different orientations of the adatoms were considered, labeled 1 to 8, and they are illustrated in Fig. 2. These configurations contain all the pairs that are separated at most 5.8 Å (configuration 8) and are stable for one-sided adsorption. In configuration 1, the adatoms are separated by 3.8 Å, and for shorter separations the adatoms dimerize [40,46]. The dimerized solution is further discussed in Sec. 2 of Ref. [74]. The pair configurations were studied in two supercell sizes. The first is the  $7 \times 7$  SC containing 98 graphene atoms plus the two adatoms. In this case, the separations between periodic images are at least 11.7 Å (configuration 8). As discussed in the Sec. 3.1 of Ref. [74], these separations guarantee reasonably good isolation of the adatom pairs. The SC size  $7 \times 7$  is also used by Gerber *et al.* [40], and their configurations C, D, and E correspond to our configurations 3, 2, and 6, respectively. Another SC size is  $6 \times 3$ , these SCs have 36 graphene atoms plus the two adatoms. The interactions between adatoms and their periodic images are strong. Thus the adatom pairs interact with their surroundings. These cells were intended for simulating random adatom distributions with a coverage of one adatom per 18 graphene atoms.

In *adatom array configurations*, the adatoms and their periodic images form regular and infinite arrays, which were employed in simulations involving long-range interactions. These arrays replace the isolated adatom pairs, which would have prohibitively large SCs in the case of remote interactions. The adatom array results are discussed in Sec. III B. The studied array types were labeled  $\alpha$ ,  $\beta$ , and  $\gamma$ . For  $\alpha$  arrays, a  $N \times N$  graphene SC with one adatom was repeated twice to yield two adatoms in a  $2N \times N$  SC. This operation leads to equilateral triangular array as illustrated in Fig. 2(a) for the case of  $8 \times 4$  SC. In this study, two SC sizes ( $6 \times 3$  and  $8 \times 4$ ) were used and they correspond to  $\sim 7.5$  and  $\sim 10$  Å adatom separations, respectively. For the  $\beta$  arrays,  $C_2^{\text{ad}}$  was moved

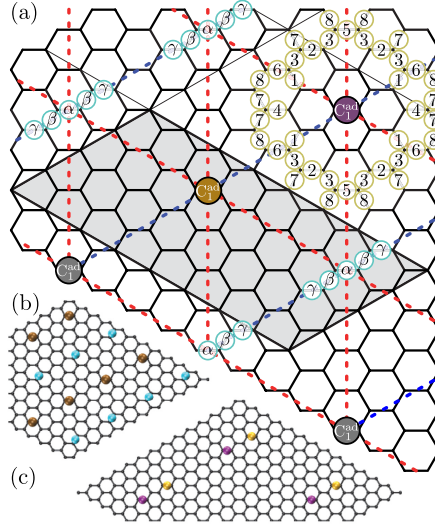


FIG. 2. (a) In the adatom pairs the purple  $C_1^{\text{ad}}$  is the first adatom and the second one is located in one of the sites labeled 1 to 8. In the adatom arrays, the ochre  $C_1^{\text{ad}}$  represents the first adatom in the unit cell (the gray area) and the other  $C_1^{\text{ad}}$  are its periodic images. The second adatom and its periodic images are located at sites  $\alpha$ ,  $\beta$ , or  $\gamma$ . The present illustration is for the SC size  $8 \times 4$ . The dashed lines indicate nearest-neighbor interactions for the  $\alpha$  array. All the symmetry-equivalent positions of  $C_2^{\text{ad}}$  are shown. (b) The  $\beta$  ( $6 \times 3$ ) array, where the unit cell is repeated  $2 \times 4$  times. (c) Configuration 6 on a  $7 \times 7$  SC, where the unit cell is repeated  $2 \times 2$  times.

to the neighboring bridge site, breaking the  $D_{3h}$  symmetry of the  $\alpha$  arrays. The  $\gamma$  arrays were obtained by further moving  $C_2^{\text{ad}}$ . In these arrays, six nearest-neighbor adatom-adatom interactions per unit cell are present. However, in interactions between an adatom and its own periodic images, the spins are parallel in both FM and AFM solutions, hence their contribution to  $\Delta E$  cancels. There are two interactions per unit cell leading to this cancellation [blue dashed lines in Fig. 2(a)], hence only four nearest-neighbor interactions [red dashed lines in Fig. 2(a)] contribute to  $\Delta E$ .

### C. Theoretical analysis

In conventional RKKY theory, the indirect exchange interaction between two adatoms mediated by delocalized electrons is described by the following Hamiltonian [78]:

$$\hat{H}_{\text{RKKY}} = J\delta(\mathbf{r} - \mathbf{R}_1)\hat{\mathbf{S}}_1 + J\delta(\mathbf{r} - \mathbf{R}_2)\hat{\mathbf{S}}_2, \quad (1)$$

where  $\hat{\mathbf{S}}$  is the spin operator of an electron mediating the exchange interaction,  $\mathbf{I}_{1,2}$  are the adatoms spins,  $J$  is the exchange constant,  $\mathbf{R}_{1,2}$  denote positions of the two adatoms. The energy of the system is obtained by treating Eq. (1) as a perturbation, the second-order correction depends on the configuration of the adatoms spins. This interaction oscillates as a function of the distance between the magnetic centers, in the case of graphene its sign also depends on the positions

of the adatoms in relation to the graphene sublattices  $A$  and  $B$ . For small adatoms separations, the alignment is FM for  $AA$  and AFM for  $AB$  configuration. This well-known result is a consequence of Lieb's theorem for bipartite lattice [34]. A completely different situation occurs if the bound adatom states at energy  $\epsilon_0$  are resonantly coupled to the graphene 2D continuum, i.e.,  $\epsilon_0$  falls in the range of occupied states of graphene ( $\epsilon_0 \ll E_F$ ) [33]. In this case, an effective resonant hybridization occurs between the bound states and the graphene states lying within a small energy range near  $\epsilon_0$ . The resonant type of hybridization makes the perturbation approach used by conventional RKKY theory inapplicable. However, the problem can be solved using a different approach [33,79,80]. This generalized theory of indirect exchange considers the following Hamiltonian:

$$\hat{H} = \hat{H}_0 + \hat{H}_T + \hat{H}_{\text{RKKY}}, \quad (2)$$

where  $\hat{H}_0$  describes the noninteracting adatoms and graphene,  $\hat{H}_T$  describes the coupling of the magnetic centers to the graphene, in particular, it incorporates the details of the coupling to the sublattices  $A$  and  $B$ .  $\hat{H}_{\text{RKKY}}$  is the exchange term of Eq. (1). The general expression (valid for an arbitrary  $E_F$ ) for the indirect exchange energy reads [33]

$$E_{\text{ex}}^{\text{RKKY}} = \int_{-\infty}^{E_F} \frac{dE}{\pi} \arctan \frac{j^2 E^2 g(E, \mathbf{R}) \text{sign } E}{[(\epsilon_0 - E)^2 - j^2]^2}. \quad (3)$$

Here,  $j$  is the exchange energy constant describing direct exchange interaction between the adatom and graphene. The

function  $g(E, \mathbf{R})$  encapsulates all the details of the coupling between two interacting adatoms and graphene and  $\mathbf{R}$  connects the adatoms. In the case of the resonant coupling ( $\epsilon_0 \ll E_F$ ), only the energy range close to  $\epsilon_0$  contributes to the interaction due to the poles of the integrand in Eq. (3). In other words, the resonant indirect exchange ( $E_{\text{ex}}^{\text{res}}$ ) is effectively mediated only by the electrons with approximately resonant energy  $\epsilon_0$  and the adsorption geometry does not play any role. Consequently, the sign of  $E_{\text{ex}}^{\text{res}}$  only depends on the position of the resonant state relative to the Dirac point:

$$\text{sign } E_{\text{ex}}^{\text{res}} = -\text{sign}(\epsilon_0 - E_D). \quad (4)$$

If the bound impurity state lies above  $E_D$ , the indirect exchange is mediated by electronlike states of graphene and the indirect exchange is FM at a small distance between the adatoms, whereas if  $\epsilon_0 < E_D$ , it is AFM at a small distance as it is mediated by graphene holelike states [33]. In the case of carbon adatoms, the  $\psi_{p,\perp}$  state is located below  $E_D$ , therefore, we expect the C adatoms to interact antiferromagnetically when  $E_F$  is tuned above  $\epsilon_0$  by gate voltage, which we refer to as the *resonant region*.

The opposite case ( $\epsilon_0 \gg E_F$ ) is the familiar conventional RKKY. Mathematically the difference stems from the poles being outside the integration limits in Eq. (3), thus the whole range of the occupied states contributes to the integral. For undoped graphene, Eq. (3) simplifies for the  $AA$ ,  $AB$ , and bridge-bridge configurations into

$$\begin{aligned} E_{\text{ex},AA}^{\text{conv}}(\mathbf{R}) &= -\frac{\tau j^2}{8\pi \epsilon_0^4} \left(\frac{\hbar v_F}{R}\right)^3 \cos^2\left(\frac{x(\mathbf{R})}{2}\right), \\ E_{\text{ex},AB}^{\text{conv}}(\mathbf{R}) &= \frac{3\tau j^2}{8\pi \epsilon_0^4} \left(\frac{\hbar v_F}{R}\right)^3 \cos^2\left(\frac{x(\mathbf{R})}{2} - \theta_{\mathbf{R}}\right), \\ E_{\text{ex},\text{bri}}^{\text{conv}}(\mathbf{R}) &\approx E_{\text{ex},AA}^{\text{conv}}(\mathbf{R}_{AA}) + E_{\text{ex},AA}^{\text{conv}}(\mathbf{R}_{BB}) + E_{\text{ex},AB}^{\text{conv}}(\mathbf{R}_{AB}) + E_{\text{ex},AB}^{\text{conv}}(\mathbf{R}_{BA}), \end{aligned} \quad (5)$$

where  $R = \|\mathbf{R}\|$ ,  $\theta_{\mathbf{R}}$  is the polar angle of  $\mathbf{R}$ ,  $x(\mathbf{R}) = (\mathbf{K} - \mathbf{K}') \cdot \mathbf{R}$ ,  $\mathbf{K}$  and  $\mathbf{K}'$  are the graphene Dirac points,  $\tau$  is the energy parameter defining the strength of the adatoms coupling to graphene, and  $\mathbf{R}_{AB}$  is the vector connecting the  $A$  sublattice basal site of the first adatom to the  $B$  sublattice basal site of the second adatom.<sup>3</sup> Equations (5) are in agreement with the conventional RKKY theory results for graphene [26–32], the difference in the prefactor is due to the details of the model where the bound state level exists also in a nonresonant case [33]. As a consequence of Eqs. (5), the  $AA$  interaction is FM, while  $AB$  is AFM. However, the sign of  $E_{\text{ex},\text{bri}}^{\text{conv}}$  depends on the relative position of the adatoms. It can be approximated by summing the four  $AA/AB$  type interaction pairs between the two basal sites of the first adatom and the two basal sites of the second adatom, as in Ref. [30] for selected configurations. As the amplitude of the AFM terms is three times larger than the FM contributions, AFM

configurations are more frequent. For example, if  $\theta_{\mathbf{R}} = \pi/2$ ,  $E_{\text{ex},\text{bri}}^{\text{conv}}$  is FM only if the separation between adatoms is  $3n$  graphene unit cells ( $n \in \mathbb{N}$ ), otherwise it is AFM. The  $n = 2$  case corresponds to configuration 5 defined in Sec. II B. For the adatom arrays,  $\Delta E$  can be approximated by summing the nearest-neighbor interactions. For example, in the  $\alpha(8 \times 4)$  array shown in Fig. 2, there are two different adatom pairs: (i)  $\theta_{\mathbf{R}} = \pi/2$ ,  $n = 4$  and (ii)  $\theta_{\mathbf{R}} = \pi/6$ ,  $n = 4$ . The sum of their contributions is AFM. The results on both conventional and resonant RKKY are summarized in Table I. The results are valid under the rigid band approximation. Effects beyond this approximation have been discussed by Shiranzai *et al.* [81].

Both RKKY theories discussed above assume the nonpolarized continuum of the mobile carriers mediating the indirect exchange interaction between the adatoms. However, in practice, the impurity states have some spatial spillover on the graphene backbone and therefore a hybridization occurs and an impurity band develops with a typical width proportional to the coupling strength [19]. A weak coupling between the impurity states leads to a narrow band with a large DOS. When the Fermi level being adjusted by  $V_g$  falls

<sup>3</sup>For doped graphene, analytical formulas have been considered in Ref. [31].

TABLE I. Dependency of the sign of  $E_{\text{ex}}^{\text{RKKY}}$  to geometry of the system and to location of  $\epsilon_0$  with respect to  $E_F$  and  $E_D$ .

Geometry	Conventional RKKY ( $E_F < \epsilon_0$ )		Resonant RKKY ( $E_F > \epsilon_0$ )	
	$\epsilon_0 < E_D$	$\epsilon_0 > E_D$	$\epsilon_0 < E_D$	$\epsilon_0 > E_D$
	AA	FM	FM	AFM
AB	AFM	AFM	AFM	FM
Bri	AFM/FM	AFM/FM	AFM	FM

inside such an impurity band, the spin polarization of the mobile carriers becomes favorable leading to the onset of ferromagnetism according to Stoner model. We refer to this region as the *intermediate region*. In order to study the onset of ferromagnetism, we consider the Hubbard Hamiltonian to account for the on-site electron-electron interaction:

$$H_U = \sum_i U n_{i\uparrow} n_{i\downarrow}, \quad (6)$$

where the summation is over all graphene and adatom sites,  $n_{i\sigma}$  is the occupation number operator for electron with spin projection  $\sigma$  at site  $i$ . Here,  $U$  is the on-site Coulomb interaction energy for the two electrons occupying carbon  $p_z$  atomic orbital. As the result of the mean-field approximation, the Hubbard model leads to the Stoner model [5,19], which typically yields ferromagnetism when the Stoner criterion is satisfied for the onset of magnetization:

$$U \text{DOS}(E_F) > 1. \quad (7)$$

For graphene without adatoms,  $\text{DOS}(E_F)$  remains at about  $1 \text{ eV}^{-1}$  for a moderate gate voltage applied. However, an impurity band induced by hybridization with the adatoms would have a substantially larger DOS. As can be seen in Fig. 3, the DOS in an impurity band induced by the hybridization of the adatoms bound states with graphene exceeds  $\sim 10 \text{ eV}^{-1}$ . As for now, there are no direct experiments which allow to extract a value for the model parameter  $U$  to adequately reflect the Coulomb electron-electron interactions in graphene. In some works, it is reported to be  $U \sim t$ , where  $t \approx 2.7 \text{ eV}$  is the tight-binding hopping parameter of graphene [82]. Other experiments indicate that the strength of the Coulomb interaction in graphene is about an order of magnitude smaller [83]. Even with this lower estimate  $U \sim 0.1 \text{ eV}$  the Stoner criterion (7) is fulfilled when  $E_F$  adjusted by the gate voltage falls in the impurity band. At that the FM solution becomes energetically favorable in the intermediate region as our DFT calculations confirm.

### III. RESULTS

#### A. One C adatom per unit cell

We first focus on effects of gate voltage to the magnetic and geometrical properties of a single C adatom on  $N \times N$  supercells, which leads to a periodic adatom coverage due to the periodic boundary conditions. Figure 3 illustrates the DOS of such system with a  $4 \times 4$  SC, as well as  $l, m$  quantum number decomposed partial DOS (PDOS) projected to the adatom for

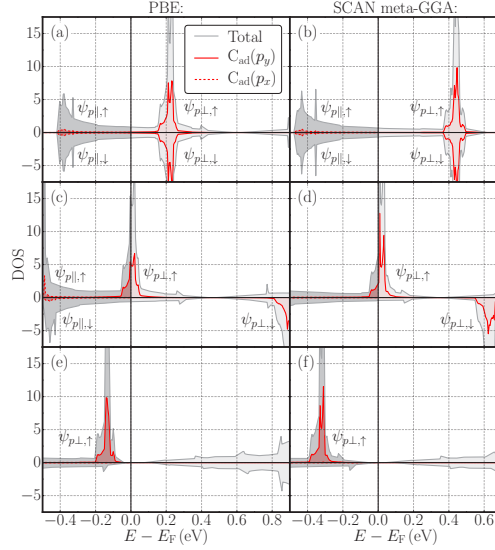


FIG. 3. Total DOS and  $lm$ -decomposed PDOS projected to the adatom for  $\Delta Q$  values of (a)  $-0.5 e$  (PBE), (b)  $-0.5 e$  (SCAN), (c)  $0 e$  (PBE), (d)  $0 e$  (SCAN), (e)  $1 e$  (PBE), and (f)  $1 e$  (SCAN). In each case,  $E_F$  has been set to zero. Positive and negative DOS values denote  $\text{DOS}(\uparrow)$  and  $\text{DOS}(\downarrow)$ , respectively.

different  $\Delta Q$  values. In this PDOS, one can see contributions from the magnetic  $\psi_{p,\perp}$  orbitals and also from strongly hybridized lower-lying adatom states denoted as  $\psi_{p,\parallel}$ . When 0.5 electrons have been removed from the unit cell, both  $\psi_{p,\perp;\uparrow}$  and  $\psi_{p,\perp;\downarrow}$  orbitals are unoccupied and degenerate in energy [Figs. 3(a) and 3(b)]. When  $V_g = 0$  [Figs. 3(c) and 3(d)], the  $\psi_{p,\perp;\uparrow}$  orbital becomes partly occupied and the  $\psi_{p,\perp;\downarrow}$  orbital is lifted in energy by the Stoner splitting. Therefore the C adatom network magnetizes and the magnetic moment per adatom is  $M = 0.38 \mu_B$  for PBE and  $M = 0.24 \mu_B$  for SCAN. The application of a positive  $V_g$  fills the  $\psi_{p,\perp}$  impurity state completely as illustrated in Figs. 3(e) and 3(f) for the case  $\Delta Q = 1 e$ . Interestingly, at  $\Delta Q = 1 e$ , the Fermi level is exactly at  $E_D$  since the extra electron is completely absorbed by the  $\psi_{p,\perp}$  orbital. Therefore, only electrons of the graphene matrix are present at the Fermi level.

Comprehensive magnetization results are given by  $M(\Delta Q)$  curves presented in Fig. 4. For PBE, the curve is rather linear with a slope of about  $0.65 \mu_B/e$  until the magnetization saturates at  $\Delta Q = 1 e$ . This slope is rather steep because the PDOS of the  $\psi_{p,\perp}$  state is high compared to the graphene DOS. However, in the region below  $M \lesssim 0.2 \mu_B$  the curve presents a nonlinear behavior related to a breakdown of the Stoner model. For SCAN, significant differences with respect to the PBE results can be noticed. In particular, the growth of the magnetization curve is steeper. Below  $M \approx 0.5 \mu_B$  the slope is  $1.4 e/\mu_B$ , but it gradually decreases to  $0.8 e/\mu_B$  before saturation. Interestingly, the magnetization

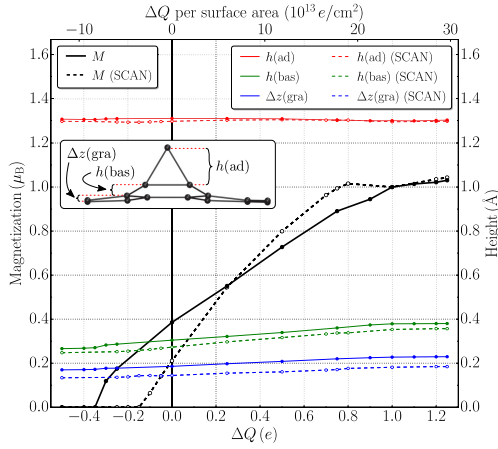


FIG. 4. Magnetization  $M$ , height of the adatom  $h(\text{ad})$ , height of the basal atoms  $h(\text{bas})$ , and buckling of the graphene sheet  $\Delta z(\text{gra})$  as functions of  $\Delta Q$  for a  $4 \times 4$  SC with one adatom. Also  $\Delta Q$  per surface area is given in the upper x axis. (Inset) Side view of the PBE structure for  $\Delta Q = 1.25 e$  and the definitions for the geometrical parameters.

slope is larger than  $1 \mu_B/e$  for most of the curve, which implies that  $\psi_{p,\perp}$  moves downwards in energy while being filled from the voltage bias, and therefore also attracts electrons from the graphene lattice. This feature of SCAN (which contains corrections to PBE) indicates a stronger response of magnetic moment to  $V_g$  in comparison to PBE. Another experimentally verifiable SCAN result is that at  $\Delta Q = 0 e$ , the magnetization ( $0.24 \mu_B$ ) is significantly reduced in comparison to the PBE result ( $0.38 \mu_B$ ). We have observed similar trend in simulations with other SCs. This observation can explain the fact that intrinsic carbon magnetism is observed only in rare occurrences [53–55,58,59] instead of being a common phenomenon. Moreover, our results indicate that gate voltage can be used as a control tool to enhance magnetism in various graphitic samples that are either weakly magnetic or even nonmagnetic. In fact, the same principle applies to various graphene-based magnetism, as recently experimentally demonstrated [11,14,16].

Our results with other SC sizes show that the slopes of  $M(\Delta Q)$  curves become smaller when the adatom is placed on bigger SCs. This observation can be explained as follows. For bigger SCs, there is a larger number of graphene states. Therefore, a larger  $\Delta Q$  contribution occupies the graphene states instead of the  $\psi_{p,\perp}$  band. However, smaller  $M(\Delta Q)$  slopes do not necessarily mean weaker magnetic response to the gate voltage since this response [i.e., slope of  $M(V_g)$ ] is related to the DOS peak width of the impurity state. In fact, the peak width clearly decreases with increasing SC size because the hybridization between the localized  $\psi_{p,\perp}$  state with its periodic images is reduced. The peak widths at  $\Delta Q = 0$  have the following trend for different SCs:  $3 \times 3$ : 0.23 eV;  $4 \times 4$ : 0.10 eV;  $5 \times 5$ : 0.08 eV;  $6 \times 6$ : 0.04 eV;  $7 \times 7$ : 0.03 eV;

$9 \times 9$ : 0.03 eV; and  $9 \times 9$ : 0.02 eV.<sup>4</sup> Nevertheless, more dilute adatom coverage produces also smaller magnetization per surface area and weaker magnetic coupling between adatoms.

The gate voltage affects also geometrical properties according to Fig. 4. The inset of Fig. 4 defines  $h(\text{ad})$  as the height of the adatom C with respect to the basal atoms,  $h(\text{bas})$  as the height of the basal atoms with respect to the nearest-neighbor graphene atoms and  $\Delta z(\text{gra})$  as buckling of graphene. The total height of the structure is  $\Delta z(\text{tot}) = h(\text{ad}) + h(\text{bas}) + \Delta z(\text{gra})$ . Without gate voltage, these values are for SCAN  $h(\text{ad}) = 1.30 \text{ \AA}$ ,  $h(\text{bas}) = 0.27 \text{ \AA}$ ,  $\Delta z(\text{gra}) = 0.15 \text{ \AA}$ , and  $\Delta z(\text{tot}) = 1.72 \text{ \AA}$ .  $V_g$  does not have much effect on  $h(\text{ad})$  nor in overall on the shape of the nearly equilateral triangle formed by the adatom and the basal atoms. More noticeable is the upwards movement of the triangle when  $\Delta Q$  is filled. This motion can be tracked in the increase of  $h(\text{bas})$  by  $0.08 \text{ \AA}$  and in the increase of  $\Delta z(\text{gra})$  by  $0.04 \text{ \AA}$ . The PBE values are nearly identical for  $h(\text{ad})$ , about  $0.03 \text{ \AA}$  larger for  $h(\text{bas})$  and  $0.04 \text{ \AA}$  to  $0.06 \text{ \AA}$  larger for  $\Delta z(\text{gra})$ . The upwards motion of the triangle and increase in the buckling of graphene, produced by the filling of  $\psi_{p,\perp}$  state, could be explained by the repulsive Coulomb interaction of the  $\psi_{p,\perp}$  state with the  $p_z$  orbitals of graphene. Nevertheless,  $h(\text{bas})$  and  $\Delta z(\text{gra})$  are significant even when the  $\psi_{p,\perp}$  state is emptied.

We have also verified that our binding energies are consistent with previously calculated values of  $-1.46 \text{ eV}$  [20] and  $-1.63 \text{ eV}$  [43]. Our results yield  $-1.46$ ,  $-1.52$ ,  $-1.51$ , and  $-1.52 \text{ eV}$  with  $3 \times 3$ ,  $4 \times 4$ ,  $5 \times 5$ , and  $9 \times 9$  SCs, respectively. Therefore, the binding energies are not sensitive to the SC size until at high concentrations. For SCAN, a slight decrease in binding energy was observed as for  $4 \times 4$  and  $5 \times 5$  SCs our results gave values of  $-1.44 \text{ eV}$  and  $-1.46 \text{ eV}$ , respectively. However, our PBE results for the energies of the top and hexagonal special symmetry adsorption sites are lower than in the literature, which is possibly because we let the graphene fully relax while constraining the symmetry of these adsorption sites. For the top site, we obtained an energy, which is  $0.63 \text{ eV}$  higher than for the bridge site, meanwhile the reported values are  $0.72 \text{ eV}$  [39] and  $0.86 \text{ eV}$  [45]. For the hexagonal site, our value is  $1.27 \text{ eV}$ , and the literature values are  $1.36 \text{ eV}$  [39] and  $1.81 \text{ eV}$  [45].

## B. Remote interaction adatom array configurations

This section focuses on adatom arrays  $\alpha$ ,  $\beta$ , and  $\gamma$  (see Sec. II B on their definitions). These structures have two adatoms in the unit cell and they are suitable for description of remote interactions. Both one-sided and two-sided adsorptions are considered. The long range interactions between the adatoms depend on their respective lattice positions and affect the magnetizations and energies of the FM and AFM solutions. Figures 5(a) and 5(b) illustrate the average magnetization per adatom of the FM solutions ( $\bar{M} = M(\text{FM})/2$ ) for  $6 \times 3$  and  $8 \times 4$  graphene SCs, respectively. These quantities are functions of the average added charge per adatom ( $\bar{\Delta Q} = \Delta Q/2$ ).

<sup>4</sup>The peak widths have been taken from DOS plots with  $E_F$  taken above the  $\psi_{p,\perp}$  state by positive  $\Delta Q$ .

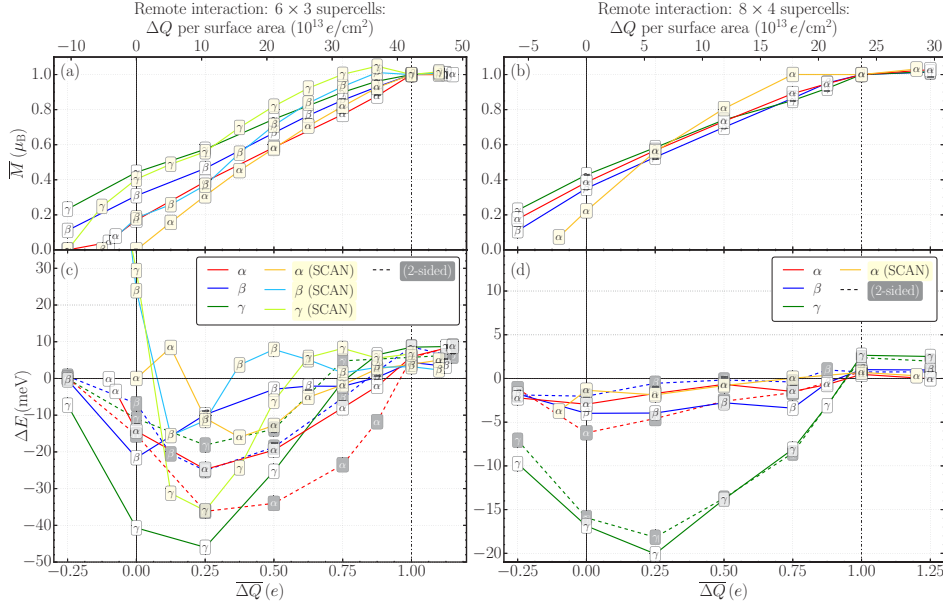


FIG. 5. Remote interaction arrays. (a) and (b) represent  $\bar{M} = M(\text{FM})/2$  for  $6 \times 3$  and  $8 \times 4$  SCs, respectively. (c) and (d) contain the  $\Delta E = E(\text{FM}) - E(\text{AFM})$  values for  $6 \times 3$  and  $8 \times 4$  SCs, respectively. Both quantities are given as a function of  $\Delta Q$  per adatom (lower axis) and  $\Delta Q$  per surface area (upper axis). The solid/dashed lines and light/dark markers correspond to one-sided/two-sided adsorption of the two adatoms. Some  $\Delta E$  data points are out of the scale, see Sec. 1.3 of Ref. [74] for details. The schematic insets label the intermediate and resonant regions.

As an example, the  $\bar{M}$  curves of  $\alpha(8 \times 4)$  are identical (but with fewer data points) to the  $M$  curves in Fig. 4 because the FM  $\alpha(8 \times 4)$  solution is equal to doubling the solution of the  $4 \times 4$  SC with one adatom. The remaining  $\bar{M}$  results are in overall similar. At  $V_g = 0$ , the SCAN magnetizations are smaller than for PBE, in fact for  $\alpha(6 \times 3)$  it is even zero. The slopes of the  $\bar{M}$  curves depend on SC size as discussed in Sec. III A, but they do not depend significantly on the array type. However, there is a dependency on the offset magnetization so that at  $V_g = 0$  the PBE magnetizations vary from  $\bar{M}(\alpha) = 0.17 \mu_B$  to  $\bar{M}(\gamma) = 0.44 \mu_B$  for  $6 \times 3$  SCs and from  $\bar{M}(\beta) = 0.35 \mu_B$  to  $\bar{M}(\gamma) = 0.43 \mu_B$  for  $8 \times 4$  SCs. The corresponding SCAN magnetizations vary from  $\bar{M}(\alpha) = 0.00 \mu_B$  to  $\bar{M}(\gamma) = 0.40 \mu_B$  for  $6 \times 3$  SCs. This variation of magnetizations can be connected to steep magnetization slopes and large DOS associated to the  $\psi_{p,\perp}$  states. In these conditions, tiny energy shift produced by interactions of adatoms change  $\psi_{p,\perp}$  occupations significantly. For this reason, the magnetization values are also sensitive to the computational details, particularly on the choice of XC functional and density of the  $k$ -point mesh. One can now understand why calculated magnetic moments vary significantly in the literature [3]. However, with positive gate voltage the differences for the magnetization values become smaller. Moreover,  $\bar{M}(\beta)$  and  $\bar{M}(\gamma)$  robustly reach the saturation magnetism at around  $\Delta Q = 1 e$ .

We turn now to discuss an important result of this study concerning the energy differences  $\Delta E = E(\text{FM}) - E(\text{AFM})$ . This quantity is plotted as a function of  $\Delta Q$  in Figs. 5(c) and 5(d) for  $6 \times 3$  and  $8 \times 4$  SCs, respectively. The differences in  $\Delta E$  between the respective one-sided and two-sided configurations are significant, but differences in the magnetization are not. We also observe very different energies in the different  $\Delta Q$  regions, which have been discussed in Sec. II C. In the intermediate region (with only partially filled  $\psi_{p,\perp}$  impurity states), PBE and SCAN behave differently, but in both cases a clear ferromagnetic valley is formed in the middle of the region for each array. Representative  $\Delta E$  maximum values are about  $-30$  and  $-5$  meV for  $6 \times 3$  and  $8 \times 4$  SCs, respectively. In the case of structures with two-sided adsorption, the energy difference magnitudes are larger for  $\alpha$  but smaller for  $\gamma$ . In most cases, the total energy was found to be lower for the two-sided adsorption configuration than for the respective one-sided one (see Sec. 2 of Ref. [74]). For  $\beta$  arrays, the ferromagnetism for two-sided adsorption is clearly weaker for the  $8 \times 4$  SCs but for the  $6 \times 3$  SCs there is no clear difference in the maximum  $\Delta E$  magnitude. In general, the  $\gamma$  arrays yield the most robust ferromagnetism, especially for the  $8 \times 4$  SCs. Also the total energies are lower for the  $\gamma$  arrays (see Sec. 2 of Ref. [74]). The most stable FM solution depends on the occupation of the  $\psi_{p,\perp}$  state. Regardless of the SC size or the XC functional, this solution corresponds to  $\bar{M} = (0.40 \pm 0.05) \mu_B$ ,  $(0.35 \pm 0.10) \mu_B$ , and

$(0.55 \pm 0.05) \mu_B$  for  $\alpha$ ,  $\beta$ , and  $\gamma$  arrays, respectively. These results can be understood within the Stoner model. In the AFM solution, there is no hybridization between  $\psi_{p,\perp;\uparrow}^1$  and  $\psi_{p,\perp;\downarrow}^2$  impurity states, which are associated to  $C_1^{\text{ad}}$  and  $C_2^{\text{ad}}$  adatoms, respectively. On the contrary, in the FM solution,  $\psi_{p,\perp;\uparrow}^1$  and  $\psi_{p,\perp;\downarrow}^2$  hybridize, which reduces the magnetization of the FM solution.<sup>5</sup> The hybridization leads to a trade for potential energy by the expense of kinetic energy. The Stoner's criterion reveals whether or not the trade was beneficial. Because of the peak in the DOS, the FM solution is stabilized. This phenomenon explains also why the maximum of the FM interaction is given at  $\bar{M} \approx 0.5 \mu_B$ , since the DOS reaches its maximum around half-filling. Incidentally, the Stoner model becomes irrelevant in the resonant region, where the impurity band is completely filled. One can also visualize the present phenomenology as follows. The hybridization between  $\psi_{p,\perp;\uparrow}^1$  and  $\psi_{p,\perp;\downarrow}^2$  creates bonding and antibonding states. The filling of the bonding state ( $\bar{M} \rightarrow 0.5 \mu_B$ ) stabilizes the FM solution, while the filling of the antibonding state ( $\bar{M} \rightarrow 1 \mu_B$ ) weakens it. When SCAN and PBE  $\Delta E$  are compared, the results in the most strongly FM region look similar, suggesting that PBE captures the Stoner phenomenology rather well. However, the SCAN FM stability is systematically slightly weaker. As a matter of fact, SCAN promotes orbital localization, since SCAN is more sensitive to chemical bonds than PBE by taking into account the kinetic energy density of the electrons.

For low magnetizations, SCAN yields strong AFM excursions especially for  $\gamma(6 \times 3)$  and  $\beta(6 \times 3)$  but also for  $\alpha(6 \times 3)$ , meanwhile this phenomenon is completely absent in the PBE results. These AFM anomalies can be explained within conventional RKKY. At low magnetizations, the  $\psi_{p,\perp}$  orbitals become more localized for SCAN, but PBE cannot capture this localization. As discussed in Sec. II C, the Stoner model can break down in this dilute limit. In these conditions, the indirect exchange mediated by the conduction graphene electrons dominates. For low magnetizations, the integration of Eq. (3) has not yet reached the poles, thus  $E_{\text{ex}}^{\text{RKKY}} \approx E_{\text{ex,bri}}^{\text{conv}}$ . Now, Eq. (5) explains that  $E_{\text{ex}}^{\text{conv}}$  is slightly AFM for  $\alpha(6 \times 3)$  and  $\alpha(8 \times 4)$ , strongly AFM for  $\beta(6 \times 3)$  and even more strongly AFM for  $\gamma(6 \times 3)$ . This scenario qualitatively agrees with the SCAN results since strong AFM excursions appear for  $\gamma(6 \times 3)$  and  $\beta(6 \times 3)$  and a weaker one for  $\alpha(6 \times 3)$ . There is a small inconsistency with the conventional RKKY picture in the  $\alpha(8 \times 4)$  curve, where the expected small AFM peak is absent. However, as discussed in Sec. 1.3 of Ref. [74], in this conventional RKKY region, there is substantial numerical instability in the AFM solution, manifesting the delicateness of the underlying physics. Therefore,  $\Delta E$  is sensitive to computational details and the SCAN results for low  $\bar{M}$  may contain error in the meV range. Moreover, it should be noted that the Eq. (5) is only approximative for the bridge site and that  $\alpha(6 \times 3)$  and  $\alpha(8 \times 4)$  arrays contain competing AFM and FM interactions. Therefore, the conventional RKKY fer-

romagnetism for  $\alpha(8 \times 4)$  is not conclusive, but the AFM peaks for  $\gamma(6 \times 3)$  and  $\beta(6 \times 3)$  are robust and thus confirm the conventional RKKY model.

When the  $\psi_{p,\perp}$  orbitals become fully occupied,  $\Delta E$  reaches AFM plateaus. In this region, the impurities do not anymore interact via the Stoner's mechanism and the situation becomes similar to the Heitler-London limit for the hydrogen molecule, where electrons on different sites have opposite spins. However, the observed antiferromagnetism could be also explained by the RKKY formalism. As discussed in Sec. II C, in this  $\overline{\Delta Q}$  region, RKKY is described within the resonant RKKY model, which predicts AFM interaction energies because the impurity states lie below  $E_D$ .

### C. Close interaction adatom pair configurations

We now consider that the adatoms are in the neighborhood of each other by using close interaction pair configurations 1–8 in  $7 \times 7$  and  $6 \times 3$  SCs. A striking difference with respect to the remote interaction cases are nonlinear growths of the magnetizations curves displayed in Figs. 6(a) and 6(b). The  $\Delta E$  values shown in Figs. 6(c) and 6(d) are also substantially larger than the corresponding remote interaction energies.

Let us first focus on the  $7 \times 7$  SC structures, which represent well-isolated adatom pairs. In the region  $\overline{\Delta Q} \lesssim 0.5 e$ , the magnetizations stay roughly constant or even decrease when more electrons are added. This behavior is produced by minority spin  $\psi_{p,\parallel;\downarrow}$  orbitals. Normally, these states lie deep in energy (as shown in Fig. 3), but strong interactions between adatoms and large structural distortions raise these states to  $E_F$  (see the DOS plot in Sec. 3.2 of Ref. [74]). Upon increasing  $\overline{\Delta Q}$  both  $\psi_{p,\perp;\uparrow}$  and  $\psi_{p,\parallel;\downarrow}$  are being occupied. These fillings yield opposing contributions to the magnetization. Thus increasing  $\overline{\Delta Q}$  often results in zero or even negative magnetization slope. Moreover, the  $\psi_{p,\parallel}$  states may have different occupations at  $C_1^{\text{ad}}$  and  $C_2^{\text{ad}}$  at low  $\Delta Q$  values, leading to adatom magnetic moments with different magnitudes. Thus, in many cases, the AFM solution becomes a ferrimagnetic solution with nonzero total magnetization (see Sec. 3.2 of Ref. [74] for details about these cases). Furthermore, the  $\psi_{p,\parallel}$  states bring complication in  $\Delta E$  because the number of interacting states becomes higher and PDOS( $E_F$ ) can have both significant spin up and spin down components. Besides, the graphene Dirac cone is severely deformed. Nevertheless, the values for  $\Delta E$  reveal a preference for strong ferromagnetism with values as high as  $-104$  meV (configuration 6) but configurations 7 and 8 display antiferromagnetism (or ferrimagnetism) with maximum magnitude of 40 meV. These results suggest high Curie temperatures in many of the studied configurations.

We now discuss higher gate voltages. Beyond the limit  $\overline{\Delta Q} \gtrsim 0.5 e$ , the  $\psi_{p,\parallel}$  states become fully occupied. In this regime, the magnetization and  $\Delta E$  recover a behavior similar to the remote interaction cases discussed in the previous section. In the intermediate region ( $0.5 e \lesssim \overline{\Delta Q} \lesssim 1 e$ ), the magnetizations are linear and their values for the respective one-sided and two-sided adsorption models are almost equal. Moreover, each one stabilizes the FM solution (though some cases only weakly). Above  $\overline{\Delta Q} = 1 e$ , the close interaction configurations behave similarly with the adatom array ones. The magnetizations saturate and the antiferromagnetism is

<sup>5</sup>We have verified from our data that the magnetic moments projected to  $C_1^{\text{ad}}$  and  $C_2^{\text{ad}}$  are larger in the AFM solution than in the FM solution.

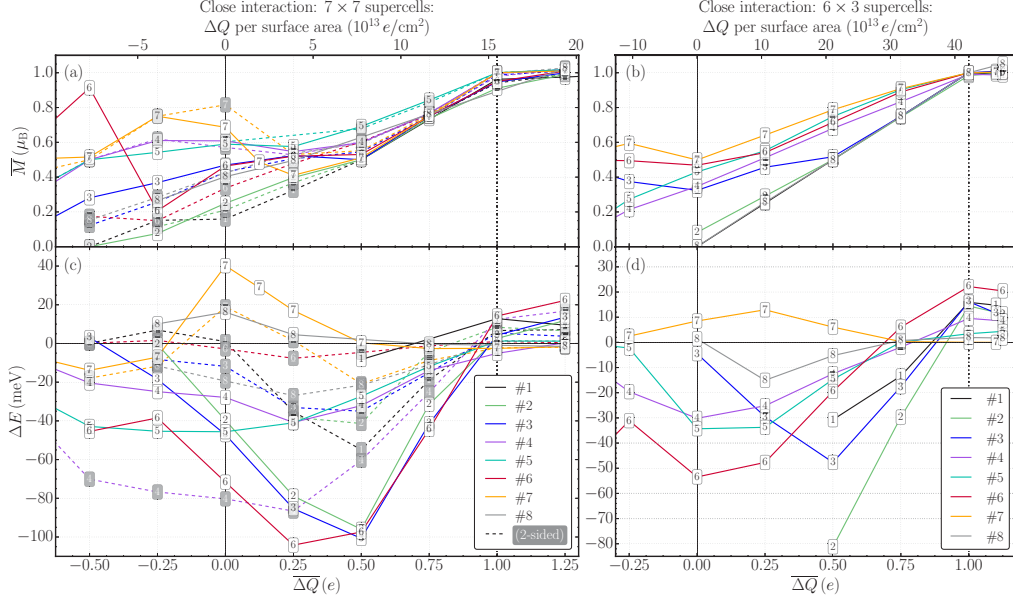


FIG. 6. Close interaction pairs. (a) and (b) represent  $\bar{M}$  for  $6 \times 3$  and  $8 \times 4$  SCs, respectively. (c) and (d) contain the  $\Delta E = E(\text{FM}) - E(\text{AFM})$  values for  $6 \times 3$  and  $8 \times 4$  SCs, respectively. Both quantities are given as a function of  $\Delta \bar{Q}$  (lower axis) and  $\Delta Q$  per surface area (upper axis).

stabilized. In this case, the RKKY theory is inapplicable because the Dirac cone is deformed and the rigid band approximation has become invalid.

The  $6 \times 3$  SC structures have significant next-nearest-neighbor interactions between  $C_1^{\text{ad}}$  and the periodic images of  $C_2^{\text{ad}}$  and vice versa. All these interaction distances are in the range 5–10 Å, which corresponds to the remote interaction case with FM character in the region  $\Delta \bar{Q} < 1 e$ . Thus, in comparison to the  $7 \times 7$  SC results, one expects to observe stronger ferromagnetism in configurations 1–6 and weaker antiferromagnetism or even ferromagnetism in the configurations 7 and 8. Actually, configuration 8 becomes FM and 7 less AFM. On the contrary, the ferromagnetism in configurations 1–6 decreases as typical  $\Delta E$  values drop to around  $-30$  meV and are about  $-55$  meV at maximum. The reason is that the Stoner criterion is weakened because the tighter packing of the adatoms spreads the  $\psi_{p,\perp}$  energy band. The typical widths of the  $\psi_{p,\perp}$  states in PDOS are  $\sim 0.4$  eV but for the corresponding  $7 \times 7$  SC configurations, they are  $\sim 0.1$  eV. In our tests with even tighter packing, the ferromagnetism is further reduced. This behavior is consistent with Ref. [25], which argues that in band ferromagnetism with  $sp$  character the magnetization must be inhomogeneous with only a fraction of the sample ferromagnetically ordered. In the case of fully filled  $\psi_{p,\perp}$  states, the results are nearly equal with respect to the  $7 \times 7$  SC cases.

The total energies of each structure have been listed in Sec. 2 of Ref. [74]. Regardless of the SC size, the configuration

4 was found to be lowest in energy and configuration 6 the highest, with an energy difference of 337 meV between these cases for the one-sided adsorption at  $7 \times 7$  SC. Adsorbing the adatoms to the different sides of the graphene sheet rather than on one side was found to be energetically favorable in most cases, as in the case of adatom arrays. The  $7 \times 7$  SC configuration 4 was found to be 5.42 eV higher in energy with respect to the dimerized solution, suggesting the existence of strong attractive potential between the adatoms. As a matter of fact, the  $7 \times 7$  SC configuration 4 was found to have 314 meV lower energy than two individual adatoms on  $7 \times 7$  SCs. This suggests that a low temperature might be needed to stabilize the studied adatom pairs.

In summary, our close interaction results show robustness of the Stoner paradigm for the C adatom system on graphene. Even when the  $\psi_{p,\parallel}$  states are present at  $E_F$  (below  $\Delta \bar{Q} \approx 0.5 e$ ), the general trend is that the interaction energies are FM in the intermediate region, which implies that the ferromagnetism could persist in more complicated and experimentally realizable carbon systems [48]. The gate voltage can be used to further optimize FM interaction strengths. Our study also reveals that in this regard  $6 \times 3$  is roughly the optimal SC size for two adatoms, which corresponds to one adatom per 18 graphene atoms. However, our results indicate that within this concentration, it is beneficial if adatoms are scattered inhomogeneously, since stronger ferromagnetism is observed for close interaction adatom pairs than for adatom arrays within the  $6 \times 3$  SCs.

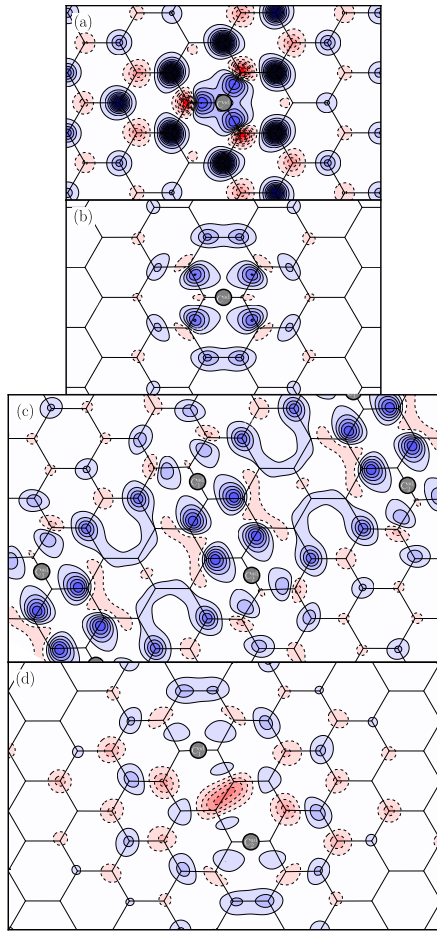


FIG. 7. Spin polarization maps with  $V_g = 0$  for (a) top site ( $7 \times 7$  SC), (b) bridge site ( $7 \times 7$  SC), (c) FM solution of configuration 2 ( $6 \times 3$  SC), and (d) FM solution of configuration 4 ( $7 \times 7$  SC). Blue with solid contour lines and red with dashed contour lines denote positive and negative magnetization densities, respectively. The isovalues are every  $0.002 e/\text{\AA}^3$  except for (a), for which this value is  $0.004 e/\text{\AA}^3$ . The data are taken at a slice about  $0.4 \text{\AA}$  below the graphene sheet (at the opposite side of the adatoms).

#### D. The spin polarization maps

Experimentally, the adatom-induced spin polarization of the graphene sheet can be probed by using the scanning tunneling microscopy (STM), as shown by González-Herrero *et al.* for hydrogen adatoms [13]. The DFT calculations also yield these spin patterns and they can be visualized as spatial spin polarization maps. Figure 7 illustrates these maps for selected C adatom configurations at  $V_g = 0$ .

Such map for a spin up C adatom fixed on the top site at A sublattice ( $M = 2.00 \mu_B$ ) is shown in Fig. 7(a). The magnetization pattern has triangular symmetry and the magnetizations at A/B sublattice sites are always positive/negative, respectively. The polarization is caused by the impurity state which extends to the graphene lattice and by the polarized graphene electrons carrying the indirect interactions. The tail of the impurity state is composed of  $p_z$  orbitals belonging to the A sublattice sites. The B sublattice  $p_z$  orbitals are not involved due to the bipartite nature of the graphene lattice. The corresponding patterns are similar for many magnetic defects coupling only to one sublattice, e.g., substitutional transition metal atoms [36,37]. The B sublattice sites are negatively polarized because the spin up impurity state at the A sublattice sites attracts spin up electrons from the B sublattice sites, thus magnetizing them negatively. In addition, another impurity state placed on the B sublattice interacts with the spin down graphene states. The resulting indirect interaction with the original A sublattice impurity is AFM in agreement with the Lieb's theorem. However, in the case of the hydrogen adatom, the magnetization pattern is inverted (the A/B sublattice sites have negative/positive magnetizations, respectively) [13,35,84] as explained by Casolo *et al.* [35].

The richness of the DFT simulations is also reflected in the case of bridge configurations. Figure 7(b) presents the magnetization density associated with a single adatom on a bridge site ( $M = 0.43 \mu_B$ ). Our simulations indicate that the corresponding magnetic patterns are general for any magnetic impurities coupled equally to the both graphene sublattices. The amplitudes are mostly positive, in particular, one can notice four blobs between the basal atoms and their nearest-neighbor graphene atoms and six smaller magnetization regions, two of which extend to two graphene sites. These regions are also visible in the spin polarization isosurface plot in Fig. 1. Further away positive and negative magnetizations alternate but positive amplitudes dominate similarly with the top-site situation. The magnitudes of the polarizations are strongly reduced when compared to the top site case for two possible reasons.<sup>6</sup> Firstly, the  $\psi_{p,\perp}$  state now spreads both to the A and B sublattices. Secondly, the magnetization of the C adatom is much higher for the top site configuration. In fact, by increasing gate voltage, we observe strengthening of the positive magnetizations and gradual disappearance of the negative magnetizations. The resulting pattern is highly asymmetric. Consequently, the direct coupling acquires a strong angular dependency to the vector connecting the adatoms. Moreover, the respective angle of the basal sites of  $C_1^{\text{ad}}$  and basal sites of  $C_2^{\text{ad}}$  (which can be  $\theta_{\text{bas}} = 0^\circ$ ,  $60^\circ$ , or  $120^\circ$ ) becomes relevant. The present results show an overall trend for stronger ferromagnetism for the  $\theta_{\text{bas}} = 0^\circ$  angle, as in the case of  $\gamma$  arrays and configurations 2, 4, 5, and 6. One might achieve adsorption with  $\theta_{\text{bas}} = 0^\circ$  by applying uniaxial strain, leading to longer bonds in one direction. The strain might also stabilize the adatom network. These properties of the strained system are of interest for future study.

<sup>6</sup>Notice that the contour isovalues are twice as large for the top site plot in Fig. 7(a) than in the bridge-site plots.

Figure 7(c) visualizes the magnetization patterns for non-isolated configuration 4 adatom pair ( $\bar{M} = 0.70 \mu_B$ ), which corresponds to a FM interaction with  $\Delta E = -30$  meV. In this case, the positive magnetizations induced to graphene by the two adatoms mutually strengthen, thus a mainly positive magnetization develops on the whole unit cell. This effect can be also pictured as a stronger delocalization of the  $\psi_{p,\perp}$  states. In this  $\Delta Q = 0$  plot, negative polarization areas are still visible, however, they gradually disappear when more charge is added.

Figure 7(d) contains magnetization patterns for isolated configuration 2 adatom pair ( $\bar{M} = 0.50 \mu_B$ ), which corresponds to a FM interaction with  $\Delta E = -40$  meV. An interesting feature is the negative excursion of the magnetization in between the adatoms, which is much stronger than any positive magnetization in the contour map, even though the positive magnetizations typically dominate in the FM solutions, as shown in Fig. 7(c).

Although magnetization patterns of hydrogen have been recently observed by González-Herrero *et al.* [13], at the moment, no experiments have yet measured the polarization maps related to bridge configurations. Since our DFT calculations predict that these maps are completely different, STM experiments probing these cases would be useful to test our present models.

#### IV. CONCLUSIONS

By using DFT first-principles simulations and various models of magnetism, we have proposed how to use gate voltage to control magnetism of carbon graphene adatoms. We have found that the voltage bias can be deployed to fine tune the magnetic moment of the adatoms from zero to  $1 \mu_B$  by emptying or filling the localized magnetic state on the adatom. Moreover, the gate voltage influences the strength and sign (FM or AFM) of the magnetic interactions between the adatoms. We find AFM behavior at both low and high adatom magnetic moment regions and ferromagnetism at intermediate adatom magnetic moments. At this intermediate region, the Fermi level falls in the band of impurity states, which have

formed by direct hybridizations between the impurity states despite the relatively large adatom separations (up to 1 nm). As a result, the adatom spins become ferromagnetically ordered since the Stoner's criterion is fulfilled. The strong low-magnetization antiferromagnetism can be explained within the RKKY mechanism. This antiferromagnetism was only found simulations within the more accurate SCAN meta-GGA framework, which is capable of confining the impurity states better, eliminating the direct exchange for low magnetic moments. The antiferromagnetism at high magnetic moments could result from an interplay between direct and RKKY interactions. In this case, the RKKY interaction is described within the novel resonant RKKY model, which predicts AFM interaction energies because the impurity states lie below  $E_D$ . The existence of different regimes which can be switched by Fermi level variation highlights that the system is more complex than previously believed. Previously only either (generalized) indirect RKKY exchange or direct exchange has been considered in the case of one system.

The DFT calculations reveal that both GGA and SCAN predict strongly FM configurations in the intermediate magnetic moment region, nevertheless there is a small reduction when SCAN is applied. Calculated spin polarization maps show highly nontrivial magnetic distributions in space, which could be probed with magnetic scanning microscopes. The present results can be generalized to other systems with magnetic defects which couple to the both *A* and *B* graphene sublattices and can explain some experimental findings concerning magnetism in systems based on graphene, useful for future spintronics applications.

#### ACKNOWLEDGMENTS

We are grateful to A. Feiguin, A. Bansil, and C. Lane for useful discussions. This work was supported by the Academy of Finland Grants No. 277829, No. 318500, and benefited from the generously allocated computer time at CSC–Finnish IT Center for Science, and Russian Foundation for Basic Research (RFBR) Grant No. 18-02-00668. PYMATGEN package [85] was employed in plotting and data analysis.

- 
- [1] S. A. Wolf, D. D. Awschalom, R. A. Buhrman, J. M. Daughton, S. von Molnár, M. L. Roukes, A. Y. Chtchelkanova, and D. M. Treger, *Science* **294**, 1488 (2001).
  - [2] I. Žutić, J. Fabian, and S. Das Sarma, *Rev. Mod. Phys.* **76**, 323 (2004).
  - [3] Y. P. Feng, L. Shen, M. Yang, A. Wang, M. Zeng, Q. Wu, S. Chintalapati, and C. Chang, *Wiley Interdiscip. Rev. Comput. Mol. Sci.* **7**, e1313 (2017).
  - [4] M. Terrones, A. R. Botello-Méndez, J. Campos-Delgado, F. López-Urías, Y. I. Vega-Cantú, F. J. Rodríguez-Macías, A. L. Elías, E. Muñoz-Sandoval, A. G. Cano-Márquez, J.-C. Charlier, and H. Terrones, *Nano Today* **5**, 351 (2010).
  - [5] J. Tuček, P. Błoński, J. Ugolotti, A. K. Swain, T. Enoki, and R. Zbořil, *Chem. Soc. Rev.* **47**, 3899 (2018).
  - [6] Y. Wang, Y. Huang, Y. Song, X. Zhang, Y. Ma, J. Liang, and Y. Chen, *Nano Lett.* **9**, 220 (2009).
  - [7] J. Zhou, Q. Wang, Q. Sun, X. S. Chen, Y. Kawazoe, and P. Jena, *Nano Lett.* **9**, 3867 (2009).
  - [8] A. J. M. Giesbers, K. Uhlřřová, M. Konečný, E. C. Peters, M. Burghard, J. Aarts, and C. F. J. Flipse, *Phys. Rev. Lett.* **111**, 166101 (2013).
  - [9] Y. Liu, N. Tang, X. Wan, Q. Feng, M. Li, Q. Xu, F. Liu, and Y. Du, *Sci. Rep.* **3**, 2566 (2013).
  - [10] S. Sarkar, K. Raul, S. Pradhan, S. Basu, and A. Nayak, *Physica E* **64**, 78 (2014).
  - [11] P. Chen, Y. Li, and W. Duan, *Phys. Rev. B* **92**, 205433 (2015).
  - [12] T. L. Makarova, A. L. Shelankov, A. A. Zyrianova, A. I. Veinger, T. V. Tisnek, E. Lähderanta, A. I. Shames, A. V. Okotrub, L. G. Bulusheva, G. N. Chekhova, D. V. Pinakov, I. P. Asanov, and Ž. Šjivančanin, *Sci. Rep.* **5**, 13382 (2015).
  - [13] H. González-Herrero, J. M. Gómez-Rodríguez, P. Mallet, M. Moaied, J. J. Palacios, C. Salgado, M. M. Ugeda, J.-Y. Veuillen, F. Yndurain, and I. Brihuega, *Science* **352**, 437 (2016).

- [14] C. Li, K. Komatsu, S. Bertrand, G. Clavé, S. Campidelli, A. Filoramo, S. Guéron, and H. Bouchiat, *Phys. Rev. B* **93**, 045403 (2016).
- [15] Q. Miao, L. Wang, Z. Liu, B. Wei, F. Xu, and W. Fei, *Sci. Rep.* **6**, 21832 (2016).
- [16] P. Błoński, J. Tuček, Z. Sofer, V. Mazánek, M. Petr, M. Pumera, M. Otyepka, and R. Zbořil, *J. Am. Chem. Soc.* **139**, 3171 (2017).
- [17] Q. Miao, L. Wang, Z. Liu, B. Wei, J. Wang, X. Liu, and W. Fei, *Sci. Rep.* **7**, 5877 (2017).
- [18] J. Tuček, K. Holá, A. B. Bourlino, P. Błoński, A. Bakandritsos, J. Ugolotti, M. Dubecký, F. Karlický, V. Ranc, K. Čépe, M. Otyepka, and R. Zbořil, *Nat. Commun.* **8**, 14525 (2017).
- [19] E. Pavarini, E. Koch, and U. Schollwöck, *Emergent Phenomena in Correlated Matter* (Deutsche Nationalbibliothek, 2013), Chap. 5.
- [20] I. A. Pašti, A. Jovanović, A. S. Dobrota, S. V. Mentus, B. Johansson, and N. V. Skorodumova, *Appl. Surf. Sci.* **436**, 433 (2018).
- [21] K. T. Chan, H. Lee, and M. L. Cohen, *Phys. Rev. B* **83**, 035405 (2011).
- [22] K. T. Chan, H. Lee, and M. L. Cohen, *Phys. Rev. B* **84**, 165419 (2011).
- [23] V. W. Brar, R. Decker, H.-M. Solowan, Y. Wang, L. Maserati, K. T. Chan, H. Lee, C. O. Girit, A. Zettl, S. G. Louie, M. L. Cohen, and M. F. Crommie, *Nat. Phys.* **7**, 43 (2011).
- [24] S. Alexander and P. W. Anderson, *Phys. Rev.* **133**, A1594 (1964).
- [25] D. M. Edwards and M. I. Katsnelson, *J. Phys. Condens. Matter* **18**, 7209 (2006).
- [26] S. R. Power and M. S. Ferreira, *Crystals* **3**, 49 (2013).
- [27] S. Saremi, *Phys. Rev. B* **76**, 184430 (2007).
- [28] L. Brey, H. A. Fertig, and S. Das Sarma, *Phys. Rev. Lett.* **99**, 116802 (2007).
- [29] A. M. Black-Schaffer, *Phys. Rev. B* **81**, 205416 (2010).
- [30] M. Sherafati and S. Satpathy, *Phys. Rev. B* **83**, 165425 (2011).
- [31] M. Sherafati and S. Satpathy, *Phys. Rev. B* **84**, 125416 (2011).
- [32] E. Kogan, *Phys. Rev. B* **84**, 115119 (2011).
- [33] I. V. Krainov, I. V. Rozhansky, N. S. Averkiev, and E. Lähderanta, *Phys. Rev. B* **92**, 155432 (2015).
- [34] E. H. Lieb, *Phys. Rev. Lett.* **62**, 1201 (1989).
- [35] S. Casolo, O. M. Løvvik, R. Martinazzo, and G. F. Tantardini, *J. Chem. Phys.* **130**, 054704 (2009).
- [36] C. B. Crook, C. Constantin, T. Ahmed, J.-X. Zhu, A. V. Balatsky, and J. T. Haraldsen, *Sci. Rep.* **5**, 12322 (2015).
- [37] J. Thakur, M. K. Kashyap, A. Taya, P. Rani, and H. S. Saini, *Indian J. Phys.* **91**, 43 (2017).
- [38] K. Nakada and A. Ishii, *Solid State Commun.* **151**, 13 (2011).
- [39] Y. G. Zhou, Z. G. Wang, P. Yang, X. T. Zu, H. Y. Xiao, X. Sun, M. A. Khaleel, and F. Gao, *Phys. Chem. Chem. Phys.* **13**, 16574 (2011).
- [40] I. C. Gerber, A. V. Krashennikov, A. S. Foster, and R. M. Nieminen, *New J. Phys.* **12**, 113021 (2010).
- [41] P. O. Lehtinen, A. S. Foster, A. Ayuela, A. Krashennikov, K. Nordlund, and R. M. Nieminen, *Phys. Rev. Lett.* **91**, 017202 (2003).
- [42] A. V. Krashennikov, K. Nordlund, P. O. Lehtinen, A. S. Foster, A. Ayuela, and R. M. Nieminen, *Phys. Rev. B* **69**, 073402 (2004).
- [43] R. Singh and P. Kroll, *J. Phys. Condens. Matter* **21**, 196002 (2009).
- [44] X. F. Fan, L. Liu, R. Q. Wu, G. W. Peng, H. M. Fan, Y. P. Feng, J.-L. Kuo, and Z. X. Shen, *J. Phys. Condens. Matter* **22**, 046001 (2010).
- [45] C. Ataca, E. Aktürk, H. Şahin, and S. Ciraci, *J. Appl. Phys.* **109**, 013704 (2011).
- [46] C. Ataca and S. Ciraci, *Phys. Rev. B* **83**, 235417 (2011).
- [47] V. O. Özgelik, H. H. Gurel, and S. Ciraci, *Phys. Rev. B* **88**, 045440 (2013).
- [48] S. Kim, D. D. Kulkarni, R. Davis, S. S. Kim, R. R. Naik, A. A. Voevodin, M. Russell, S. S. Jang, V. V. Tsukruk, and A. G. Fedorov, *ACS Nano* **8**, 6805 (2014).
- [49] Z. Hou and K. Terakura, *J. Phys. Chem. C* **119**, 4922 (2015).
- [50] F. Banhart, J. Kotakoski, and A. V. Krashennikov, *ACS Nano* **5**, 26 (2011).
- [51] A. Eckmann, A. Felten, A. Mishchenko, L. Britnell, R. Krupke, K. S. Novoselov, and C. Casiraghi, *Nano Lett.* **12**, 3925 (2012).
- [52] J. T. Obodo, I. Rungger, S. Sanvito, and U. Schwingenschlög, *Nanoscale* **8**, 10310 (2016).
- [53] Y. Kopelevich and P. Esquinazi, *J. Low Temp. Phys.* **119**, 691 (2000).
- [54] P. Esquinazi, A. Setzer, R. Höhne, C. Semmelhack, Y. Kopelevich, D. Spemann, T. Butz, B. Kohlstrunk, and M. Lösche, *Phys. Rev. B* **66**, 024429 (2002).
- [55] J. M. D. Coey, M. Venkatesan, C. B. Fitzgerald, A. P. Douvalis, and I. S. Sanders, *Nature (London)* **420**, 156 (2002).
- [56] P. Esquinazi, D. Spemann, R. Höhne, A. Setzer, K.-H. Han, and T. Butz, *Phys. Rev. Lett.* **91**, 227201 (2003).
- [57] K.-h. Han, D. Spemann, P. Esquinazi, R. Höhne, V. Riede, and T. Butz, *Adv. Mater.* **15**, 1719 (2003).
- [58] J. Červenka, M. I. Katsnelson, and C. F. J. Flipse, *Nat. Phys.* **5**, 840 (2009).
- [59] T. Saito, D. Nishio-Hamane, S. Yoshii, and T. Nojima, *Appl. Phys. Lett.* **98**, 052506 (2011).
- [60] G. Kresse and J. Furthmüller, *Comput. Mater. Sci.* **6**, 15 (1996).
- [61] G. Kresse and J. Furthmüller, *Phys. Rev. B* **54**, 11169 (1996).
- [62] W. Kohn, *Rev. Mod. Phys.* **71**, 1253 (1999).
- [63] J. P. Perdew, K. Burke, and M. Ernzerhof, *Phys. Rev. Lett.* **77**, 3865 (1996).
- [64] B. Barbiellini, E. G. Moroni, and T. Jarlborg, *J. Phys.: Condens. Matter* **2**, 7597 (1990).
- [65] J. Sun, A. Ruzsinszky, and J. P. Perdew, *Phys. Rev. Lett.* **115**, 036402 (2015).
- [66] J. Sun, R. C. Remsing, Y. Zhang, Z. Sun, A. Ruzsinszky, H. Peng, Z. Yang, A. Paul, U. Waghmare, X. Wu, M. L. Klein, and J. P. Perdew, *Nat. Chem.* **8**, 831 (2016).
- [67] R. Car, *Nat. Chem.* **8**, 820 (2016).
- [68] I. G. Buda, C. Lane, B. Barbiellini, A. Ruzsinszky, J. Sun, and A. Bansil, *Sci. Rep.* **7**, 44766 (2017).
- [69] J. W. Furness, Y. Zhang, C. Lane, I. G. Buda, B. Barbiellini, R. S. Markiewicz, A. Bansil, and J. Sun, *Commun. Phys.* **1**, 11 (2018).
- [70] C. Lane, J. W. Furness, I. G. Buda, Y. Zhang, R. S. Markiewicz, B. Barbiellini, J. Sun, and A. Bansil, *Phys. Rev. B* **98**, 125140 (2018).
- [71] Y. Zhang, C. Lane, J. W. Furness, B. Barbiellini, R. S. Markiewicz, A. Bansil, and J. Sun, *arXiv:1809.08457*.
- [72] P. E. Blöchl, *Phys. Rev. B* **50**, 17953 (1994).

- [73] G. Kresse and D. Joubert, *Phys. Rev. B* **59**, 1758 (1999).
- [74] See Supplemental Material at <http://link.aps.org/supplemental/10.1103/PhysRevB.99.035441> for further details of the results and the methodology described throughout the text.
- [75] P. E. Blöchl, O. Jepsen, and O. K. Andersen, *Phys. Rev. B* **49**, 16223 (1994).
- [76] A. M. Suarez, L. R. Radovic, E. Bar-Ziv, and J. O. Sofo, *Phys. Rev. Lett.* **106**, 146802 (2011).
- [77] J. O. Sofo, A. M. Suarez, G. Usaj, P. S. Cornaglia, A. D. Hernández-Nieves, and C. A. Balseiro, *Phys. Rev. B* **83**, 081411 (2011).
- [78] C. Kittel, *Quantum Theory of Solids*, 2nd ed. (Wiley, 1987).
- [79] I. V. Rozhansky, I. V. Krainov, N. S. Averkiev, and E. Lähderanta, *J. Magn. Magn. Mater.* **383**, 34 (2015).
- [80] I. V. Rozhansky, N. S. Averkiev, I. V. Krainov, and E. Lähderanta, *Phys. Status Solidi A* **211**, 1048 (2014).
- [81] M. Shiranzaei, J. Fransson, H. Cheraghchi, and F. Parhizgar, *Phys. Rev. B* **97**, 180402 (2018).
- [82] O. V. Yazyev, *Rep. Prog. Phys.* **73**, 056501 (2010).
- [83] J. P. Reed, B. Uchoa, Y. I. Joe, Y. Gan, D. Casa, E. Fradkin, and P. Abbamonte, *Science* **330**, 805 (2010).
- [84] J. O. Sofo, G. Usaj, P. S. Cornaglia, A. M. Suarez, A. D. Hernández-Nieves, and C. A. Balseiro, *Phys. Rev. B* **85**, 115405 (2012).
- [85] S. P. Ong, W. D. Richards, A. Jain, G. Hautier, M. Kocher, S. Cholia, D. Gunter, V. L. Chevrier, K. A. Persson, and G. Ceder, *Comput. Mater. Sci.* **68**, 314 (2013).
- [86] H.-J. Kim and J.-H. Cho, *Phys. Rev. B* **87**, 174435 (2013).



## Publication II

A. Pulkkinen, B. Barbiellini, J. Nokelainen, V. Sokolovskiy, D. Baigutlin,  
O. Miroshkina, M. Zagrebin, V. Buchelnikov, C. Lane, R. S. Markiewicz,  
A. Bansil, J. Sun, K. Pussi and E. Lähderanta

**Coulomb correlation in noncollinear antiferromagnetic  $\alpha$ -Mn**

Reprinted with permission from

*Physical Review B*

Vol. 101, pp. 075115, 2020

© 2020, American Physical Society.



**Coulomb correlation in noncollinear antiferromagnetic  $\alpha$ -Mn**

Aki Pulkkinen<sup>1,\*</sup>, Bernardo Barbiellini,<sup>1,2</sup> Johannes Nokelainen,<sup>1</sup> Vladimir Sokolovskiy,<sup>3,4</sup> Danil Baigutlin,<sup>1,3</sup> Olga Miroshkina,<sup>1,3</sup> Mikhail Zagrebin,<sup>3,5</sup> Vasily Buchelnikov,<sup>3,4</sup> Christopher Lane,<sup>2</sup> Robert S. Markiewicz,<sup>2</sup> Arun Bansil,<sup>2</sup> Jianwei Sun,<sup>6</sup> Katariina Pussi,<sup>1</sup> and Erkki Lähderanta<sup>1</sup>

<sup>1</sup>*School of Engineering Science, LUT University, 53850 Lappeenranta, Finland*

<sup>2</sup>*Department of Physics, Northeastern University, Boston, Massachusetts 02115, USA*

<sup>3</sup>*Faculty of Physics, Chelyabinsk State University, 454001 Chelyabinsk, Russia*

<sup>4</sup>*National University of Science and Technology, "MISIS", 119049 Moscow, Russia*

<sup>5</sup>*National Research South Ural State University, 454080 Chelyabinsk, Russia*

<sup>6</sup>*Department of Physics and Engineering Physics, Tulane University, New Orleans, Louisiana 70118, USA*



(Received 23 April 2019; revised manuscript received 7 November 2019; accepted 24 January 2020; published 12 February 2020)

We discuss the interplay between magnetic and structural degrees of freedom in elemental Mn. The equilibrium volume is shown to be sensitive to magnetic interactions between the Mn atoms. While the standard generalized gradient approximation underestimates the equilibrium volume, a more accurate treatment of the effects of electronic localization and magnetism is found to solve this longstanding problem. Our calculations also reveal the presence of a magnetic phase in strained  $\alpha$ -Mn that has been reported previously in experiments. This new phase of strained  $\alpha$ -Mn exhibits a noncollinear spin structure with large magnetic moments.

DOI: [10.1103/PhysRevB.101.075115](https://doi.org/10.1103/PhysRevB.101.075115)

**I. INTRODUCTION**

Manganese is one of the most complex metallic elements [1–7] that assumes many different stable crystal phases. On cooling the liquid, the sequence of crystal phases [8–10] obtained includes body-centered cubic (BCC)  $\delta$ -Mn, face-centered cubic (FCC)  $\gamma$ -Mn,  $\beta$ -Mn, and  $\alpha$ -Mn as illustrated in Fig. 1.  $\alpha$ -Mn has 58 atoms per unit cell with space group  $T_d^3$  (No. 217) [11] and it may be looked upon as an intermetallic involving Mn atoms in different electronic and magnetic configurations [12] on four crystallographic sublattices (I, II, III, and IV). Neutron diffraction experiments [13] have shown that sublattices III and IV further split into two types (IIIa, IIIb, IVa, and IVb) when the antiferromagnetic ordering is taken into account. Large, almost collinear magnetic moments reside on sites I and II, while substantially smaller and strongly canted moments are on sites III and IV [13].

Density functional theory (DFT) results by Hobbs *et al.* [1,2] using either the local-spin-density approximation (LSDA) or the generalized-gradient approximation (GGA) are not in agreement with experiments because the tendency of LSDA and GGA to overbind produces a collinear spin structure at the theoretical equilibrium volume. However, a noncollinear spin structure develops when the lattice is expanded beyond the experimental volume [2]. A semiempirical tight-binding method using Hubbard-like correlation effects [14] has predicted a noncollinear magnetic structure for  $\alpha$ -Mn at the experimental volume in qualitative agreement with

experiment, but a more recent tight-binding study failed to converge to the noncollinear solution [15].

In order to address the deficiencies of the LSDA and GGA, exchange-correlation corrections must be improved. One approach is to introduce an ad hoc Hubbard parameter  $U$  [16–20], which attempts to correct for self-interaction errors on localized  $3d$  orbitals of Mn by replacing LSDA and GGA potentials with orbital-dependent terms. An important test in this connection is the Mn<sub>2</sub> dimer [16] which is discussed in the Supplemental Material (SM) [21] (see also references [22–25] therein). Note that a DFT+ $U$  approach requires both Hubbard-repulsion  $U$  and Hund-exchange integral  $J$  as ad hoc parameters [26]. Here the strongly-constrained-and-appropriately-normed (SCAN) functional [27], which is a semi-local functional that satisfies seventeen exact constraints, provides a systematic improvement over the GGA. It should be noted that SCAN leads to overestimated magnetic moments in itinerant ferromagnetic transition metals such as iron [28–30]. However, there are many studies of antiferromagnetic materials such as the cuprates [31–33], spinel LiMn<sub>2</sub>O<sub>4</sub> cathode material [34], and  $3d$  perovskite oxides [35] where SCAN yields a good estimate of magnetic moments. This has also been shown to be the case in some Mn-rich Heusler alloys [36,37], where the  $3d$  magnetic electrons are quite localized on the Mn atoms.

In this paper, we show that SCAN significantly improves the description of the ground-state electronic and magnetic structure of  $\alpha$ -Mn with respect to the LSDA and GGA by correctly accounting for conflicting trends for maximizing the magnetic spin moment and the bond strength. In this way, SCAN successfully captures the complex charge and

\*aki.pulkkinen@lut.fi

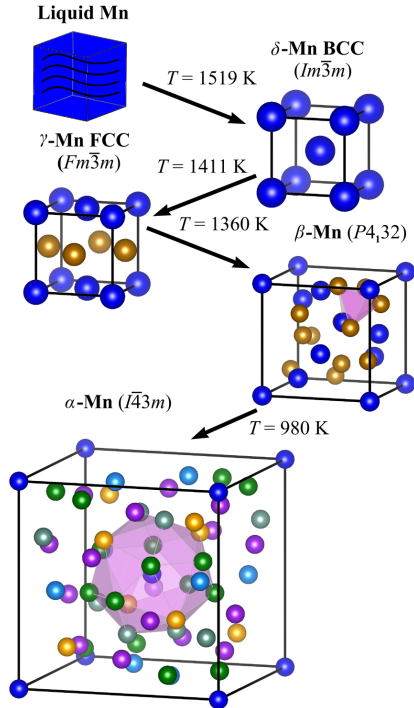


FIG. 1. A schematic illustrating the evolution of various crystal phases of Mn from liquid Mn. Colors are used to differentiate between different Mn atoms in the unit cell. The polyhedron in the  $\alpha$ -phase structure is the 17-atom cluster described by Proult & Donnadieu [10].

noncollinear magnetic ordering that occurs in  $\alpha$ -Mn at low temperatures.

## II. COMPUTATIONAL METHODS

The present DFT calculations were performed with the plane-wave method implemented in the Vienna *ab initio* simulation package (VASP) [38–40] with the projector augmented wave (PAW) method [41]. The GGA exchange-correlation functional is based on the Perdew-Burke-Ernzerhof (PBE) formulation [42] while the meta-GGA follows the SCAN implementation [27]. Structural relaxations were performed with an energy cutoff of  $\geq 550$  eV and a  $k$ -point spacing of  $< 0.02 \text{ \AA}^{-1}$ . The Methfessel-Paxton smearing method [43] was used with a width of 0.2 eV in geometry optimization runs, and the tetrahedron smearing method with Blöchl corrections [44] was used in self-consistency cycles as well as for generating the electronic density of states (DOS). Total energies were converged to  $10^{-6}$  eV. In geometry optimizations, forces on all atoms were converged to  $10^{-2} \text{ eV \AA}^{-1}$ . Spin polarization effects and the variational freedom for noncollinear spin

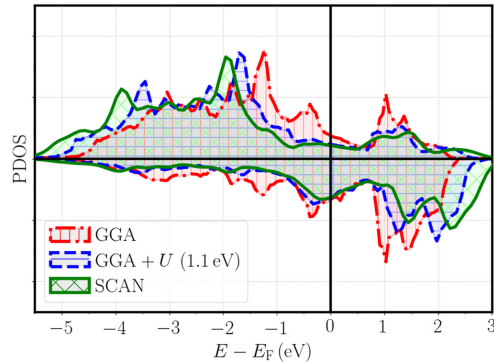


FIG. 2. Partial  $l$ -decomposed DOS (PDOS) for  $d$  electrons in  $\gamma$ -Mn at the experimental  $R_{ws} = 2.753$  a.u. for GGA, GGA+ $U$  (with  $U = 1.1$  eV), and SCAN.

arrangements were included for the  $\alpha$ -Mn structure. Note that the inclusion of noncollinearity in calculations significantly increases the computational cost as the electron density becomes a  $2 \times 2$  matrix [45,46].

## III. RESULTS

We first examine  $\gamma$ -Mn with four Mn atoms per unit cell (see SM [21] for details). Asada and Terakura [47] have shown that the LSDA underestimates the lattice constant and fails to predict the antiferromagnetic ground state. Our GGA and SCAN total energy calculations for the nonmagnetic, ferromagnetic, and antiferromagnetic AF1 and AF2 phases confirm that the ground state of  $\gamma$ -Mn is AF1, where the sign of the moment alternates between the planes stacked along the [001] direction. These phases are described by Kubler in Ref. [9]. GGA gives the Wigner-Seitz radius corresponding to the equilibrium volume [48] of  $R_{ws} = 2.635$  a.u., while SCAN gives  $R_{ws} = 2.732$  a.u., which is in better agreement with the experimental value of  $R_{ws} = 2.752$  a.u. [49]. The structure is found to be tetragonally distorted with  $c/a = 0.95$  for GGA, while SCAN produces  $c/a = 0.98$ . The calculated magnetic moments increase with the equilibrium volume, thus GGA yields  $1.74\mu_B$  whereas SCAN gives a higher value of  $3.10\mu_B$ .

In order to gauge the strength of corrections beyond the GGA captured by SCAN, we compare SCAN, GGA, and GGA+ $U$  results and extract an effective  $U$  value which reproduces the experimental equilibrium volume. In this way, we find that for  $U = 1.1$  eV, the equilibrium Wigner-Seitz radius is  $R_{ws} = 2.722$  a.u. with a Mn magnetic moment of  $2.69\mu_B$  and  $c/a = 0.98$ . These results are consistent with those reported previously by Podloucky & Redinger [50] and Di Marco *et al.* [51,52]. Figure 2 highlights the effect of  $U$  on the Mn partial DOS (PDOS) at the experimental volume. The GGA PDOS is seen to differ significantly from SCAN, but for  $U = 1.1$  eV the two Mn PDOSs becomes closer. These results

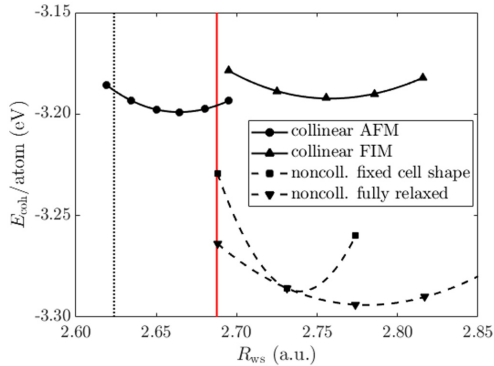


FIG. 3. SCAN-based cohesive energies for various magnetic structures of  $\alpha$ -Mn discussed in the text. The dotted vertical line corresponds to the GGA volume calculated with PBE [42] while the solid vertical line marks the experimental  $R_{ws} = 2.688$  a.u. of noncollinear  $\alpha$ -Mn [13].  $E_{coh}$  of  $\gamma$ -Mn in SCAN is  $-3.27$  eV, see also the SM [21]. The weakly ferrimagnetic (FIM) solution is compared to the AFM (collinear and noncollinear) solutions.

are also consistent with the observation of Hubbard bands in  $\gamma$ -Mn with angle-resolved photoemission spectroscopy [53].

In  $\alpha$ -Mn, sublattices I, II, and IV are occupied by close-packed polyhedra although this is not the case for sublattice III [11,54]. This close packing results in shrinking of the Wigner-Seitz radius to the experimental value [13] of  $R_{ws} = 2.688$  a.u. Figure 3 shows the cohesive energy  $E_{coh}$  as a function of  $R_{ws}$  for a collinear solution. Even with this constraint SCAN significantly corrects the GGA volume. Moreover, the calculated bulk modulus of 131 GPa is in good agreement with the experimental value of 151 GPa [55]. The computed magnetic moment distribution follows trends consistent with the experimental results given in Table II of Ref. [2]. However, exact comparisons with theory are difficult because the moments extracted from the experimental data depend sensitively on the choice of the form factors used [13,56–60]. Interestingly, our computations predict the existence of an additional collinear (metastable) solution at a higher volume with a bulk modulus of 68 GPa. The magnetic distribution for this solution becomes weakly ferrimagnetic with an average moment of  $0.11\mu_B$  per Mn atom and the corresponding charge distribution involves Mn atoms in six different electronic configurations with charge differences reaching  $0.4 e/atom$ . When spin-orbit coupling (SOC) is included in the calculations, a noncollinear magnetic structure develops to reduce frustration. We have performed two different types of noncollinear calculations in this connection. The first involved fully relaxed atomic positions with a fixed cell shape [61], while the second achieved full structural relaxation. The corresponding cohesive energies  $E_{coh}$  as a function of  $R_{ws}$  are shown in Fig. 3.

In the GGA the structure remains collinear at the experimental volume [2] but in SCAN the moments rotate out of their collinear orientations. [The SCAN-generated magnetic

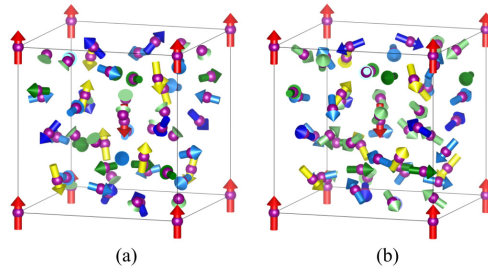


FIG. 4. SCAN-based noncollinear magnetic structure of various  $\alpha$ -Mn sublattices: I (red), II (yellow), IIIa (blue), IIIb (light blue), IVa (green), and IVb (light green). Only the atomic positions are relaxed in (a), while both the atomic positions and cell shape are relaxed in (b).

structure is noncollinear for both the calculations shown in Fig. 4.] In contrast to GGA, SCAN thus predicts noncollinear magnetic ordering at the experimental volume. In fact, as we noted above, we obtain two distinct magnetic structures, both with large collinear magnetic moments on Mn I sites, while the moments on Mn II sites are slightly smaller and canted away from the collinear direction. For the first solution, which is based on the fully-relaxed structure, we obtain  $R_{ws} = 2.781$  a.u., and this solution might correspond to the strained  $\alpha$ -phase reported experimentally by Dedkov *et al.* [62]. The second solution involves computations with a fixed cell shape. Here the determination of the equilibrium volume is more delicate since several degenerate solutions with different spin structures can coexist as is the case in  $YBa_2Cu_3O_7$  [33] cuprate high-Tc superconductor. We note, however, that since SCAN tends to favor solutions with large magnetic moments, the stabilization of the strained  $\alpha$  phase we have found might be due to the exaggerated corrections in SCAN [36,63]. Noncollinear magnetism in manganese nanostructures has been reported also within the GGA [46].

The present noncollinear implementation of VASP [45,46] neglects noncollinear correlation effects beyond the LSDA [64,65], which could possibly be the reason that SCAN yields solutions with too large equilibrium volume in  $\alpha$ -Mn [66], see Fig. 3. At the GGA level, a noncollinear spin structure stabilizes when the lattice is expanded beyond the experimental volume. In fact, in order to converge towards a noncollinear solution, Hobbs *et al.* [2] had to start their calculations with a strongly expanded initial volume ( $R_{ws} \approx 2.96$  a.u.), which however was not the final converged volume. The preceding results suggest that SCAN is a step in the right direction for stabilizing noncollinear solutions.

Overmagnetization in  $3d$  transition metals [28–30] has been found in recent SCAN calculations. This issue has been addressed with a deorbitalized potential [63]. A similar problem is present in DFT+ $U$ , where the magnetic moment changes considerably if one adopts either the fully-localized limit or the mean-field approximation [67]. Here also a deorbitalized potential for states at the Fermi level has been suggested as a possible cure [68].

#### IV. SUMMARY AND CONCLUSIONS

Our results are relevant for smart materials such as the shape-memory and magnetocaloric Mn-rich Heusler alloys [69–71] because elemental Mn and the Mn-rich Heusler alloys present phase diagrams with common features. For example, BCC  $\delta$ -Mn and FCC  $\gamma$ -Mn can be viewed as austenite and martensite phases of Heusler alloys, respectively. Although we have shown previously [36] that SCAN corrections beyond the GGA are small for Mn-poor compounds, our results here indicate that we can expect substantial differences between the GGA and SCAN in Mn-rich compounds such as  $\text{Ni}_2\text{Mn}_{1+x}(\text{Ga}, \text{Sn})_{1-x}$ . SCAN corrections should work particularly well for short Mn-Mn distances where antiferromagnetic coupling tends to suppress itinerant ferromagnetism [72]. In fact, the presence of spin- and charge-density wave like orderings in  $\alpha$ -Mn could help rationalize the complex phase diagrams of Heusler alloys and the associated phase instabilities driven by Fermi-surface nestings [73–75]. Since SCAN tends to promote complex solutions [33], future investigations of Mn-rich materials should consider large simulation cells to capture modulated phases, which could be more stable than the simple martensitic [76] phase.

Our study provides a robust self-consistent scheme to correct the overbinding in elemental Mn in LSDA and GGA. The SCAN corrections for the equilibrium volume also yield noncollinear antiferromagnetism with complex charge and

spin patterns in  $\alpha$ -Mn. These results demonstrate that the density-functional framework is capable of capturing the subtle correlation effects needed to predict technologically relevant Mn-rich materials for shape-memory, magnetocaloric, and other applications.

#### ACKNOWLEDGMENTS

It is a pleasure to acknowledge important discussions with John Perdew. The authors acknowledge CSC-IT Center for Science, Finland, for computational resources. The work of Chelyabinsk State University was supported by RSF-Russian Science Foundation project No. 17-72-20022 (calculations for  $\gamma$ - and  $\delta$ -Mn). The work at Northeastern University was supported by the U.S. Department of Energy (DOE), Office of Science, Basic Energy Sciences Grant No. DE-FG02-07ER46352 (core research), and benefited from Northeastern University's Advanced Scientific Computation Center (ASCC), the NERSC supercomputing center through DOE Grant No. DE-AC02-05CH11231, and support (testing efficacy of advanced functionals) from the DOE EFRC: Center for Complex Materials from First Principles (CCM) under Grant No. DE-SC0012575. The work at Tulane University was supported by the startup funding from Tulane University and by the U.S. DOE, Office of Science, Basic Energy Sciences Grant No. DE-SC0019350. B.B. acknowledges support from the COST Action CA16218.

- 
- [1] D. Hobbs and J. Hafner, *J. Phys.: Condens. Matter* **13**, L681 (2001).
  - [2] D. Hobbs, J. Hafner, and D. Spišák, *Phys. Rev. B* **68**, 014407 (2003).
  - [3] J. Hafner and D. Hobbs, *Phys. Rev. B* **68**, 014408 (2003).
  - [4] H. Ehteshami and P. A. Korzhavyi, *Phys. Rev. Mater.* **1**, 073803 (2017).
  - [5] H. Ehteshami and A. V. Ruban, *Phys. Rev. Mater.* **2**, 034405 (2018).
  - [6] S. Lee, C. Leighton, and F. S. Bates, *PNAS* **111**, 17723 (2014).
  - [7] A. I. Kolesnikov, A. Podlesnyak, R. A. Sadykov, V. E. Antonov, M. A. Kuzovnikov, G. Ehlers, and G. E. Granroth, *Phys. Rev. B* **94**, 134301 (2016).
  - [8] S. Bigdeli, H. Mao, and M. Selleby, *Phys. Status Solidi B* **252**, 2199 (2015).
  - [9] J. Kübler, *Theory of Itinerant Electron Magnetism*, International Series of Monographs on Physics (Oxford University Press, Chippingham, Wiltshire, UK, 2009).
  - [10] A. Proult and P. Donnadieu, *Philos. Mag. Lett.* **72**, 337 (1995).
  - [11] L. H. Bennett and R. E. Watson, *Phys. Rev. B* **35**, 845 (1987).
  - [12] J. Bradley and J. Thewlis, *Proc. R. Soc. London, Ser. A* **115**, 456 (1927).
  - [13] A. C. Lawson, A. C. Larson, M. C. Aronson, S. Johnson, Z. Fisk, P. C. Canfield, J. D. Thompson, and R. B. Von Dreele, *J. Appl. Phys.* **76**, 7049 (1994).
  - [14] K. Sasaki, H. Betsuyaku, N. Mori, and T. Ukai, *J. Magn. Magn. Mater.* **31–34**, 41 (1983).
  - [15] F. Süss and U. Krey, *J. Magn. Magn. Mater.* **125**, 351 (1993).
  - [16] C. Huang, J. Zhou, K. Deng, E. Kan, and P. Jena, *J. Phys. Chem. A* **122**, 4350 (2018).
  - [17] A. I. Liechtenstein, V. I. Anisimov, and J. Zaanen, *Phys. Rev. B* **52**, R5467(R) (1995).
  - [18] S. L. Dudarev, G. A. Botton, S. Y. Savrasov, C. J. Humphreys, and A. P. Sutton, *Phys. Rev. B* **57**, 1505 (1998).
  - [19] M. Cococcioni and S. de Gironcoli, *Phys. Rev. B* **71**, 035105 (2005).
  - [20] C. Ricca, I. Timrov, M. Cococcioni, N. Marzari, and U. Aschauer, *Phys. Rev. B* **99**, 094102 (2019).
  - [21] See Supplemental Material at <http://link.aps.org/supplemental/10.1103/PhysRevB.101.075115> for information on  $\text{Mn}_2$  dimer and  $\gamma$ -Mn.
  - [22] S. H. Vosko, L. Wilk, and M. Nusair, *Can. J. Phys.* **58**, 1200 (1980).
  - [23] U. von Barth and L. Hedin, *J. Phys. C: Solid State Phys.* **5**, 1629 (1972).
  - [24] V. L. Moruzzi, J. F. Janak, and A. R. Williams, *Calculated Electronic Properties of Metals* (Pergamon, New York, 1978).
  - [25] H. Ebert, D. Ködderitzsch, and J. Minár, *Rep. Prog. Phys.* **74**, 096501 (2011).
  - [26] I. Yang, S. Y. Savrasov, and G. Kotliar, *Phys. Rev. Lett.* **87**, 216405 (2001).
  - [27] J. Sun, A. Ruzsinszky, and J. P. Perdew, *Phys. Rev. Lett.* **115**, 036402 (2015).
  - [28] E. B. Isaacs and C. Wolverton, *Phys. Rev. Mater.* **2**, 063801 (2018).

- [29] M. Ekholm, D. Gambino, H. J. M. Jönsson, F. Tasnádi, B. Alling, and I. A. Abrikosov, *Phys. Rev. B* **98**, 094413 (2018).
- [30] Y. Fu and D. J. Singh, *Phys. Rev. Lett.* **121**, 207201 (2018).
- [31] C. Lane, J. W. Furness, I. G. Buda, Y. Zhang, R. S. Markiewicz, B. Barbiellini, J. Sun, and A. Bansil, *Phys. Rev. B* **98**, 125140 (2018).
- [32] J. W. Furness, Y. Zhang, C. Lane, I. G. Buda, B. Barbiellini, R. S. Markiewicz, A. Bansil, and J. Sun, *Commun. Phys.* **1**, 11 (2018).
- [33] Y. Zhang, C. Lane, J. W. Furness, B. Barbiellini, J. P. Perdew, R. S. Markiewicz, A. Bansil, and J. Sun, *PNAS* **117**, 68 (2019).
- [34] H. Hafiz, K. Suzuki, B. Barbiellini, Y. Orikasa, S. Kaprzyk, N. Tsuji, K. Yamamoto, A. Terasaka, K. Hoshi, Y. Uchimoto, Y. Sakurai, H. Sakurai, and A. Bansil, *Phys. Rev. B* **100**, 205104 (2019).
- [35] J. Varignon, M. Bibes, and A. Zunger, *Nat. Commun.* **10**, 1658 (2019).
- [36] V. D. Buchelnikov, V. V. Sokolovskiy, O. N. Miroshkina, M. A. Zagrebin, J. Nokelainen, A. Pulkkinen, B. Barbiellini, and E. Lähderanta, *Phys. Rev. B* **99**, 014426 (2019).
- [37] B. Barbiellini, A. Pulkkinen, J. Nokelainen, V. Buchelnikov, V. Sokolovskiy, O. N. Miroshkina, M. Zagrebin, K. Pussi, E. Lähderanta, and A. Granovsky, *MRS Adv.* **4**, 441 (2019).
- [38] G. Kresse and J. Hafner, *Phys. Rev. B* **47**, 558 (1993).
- [39] G. Kresse and J. Furthmüller, *Comput. Mater. Sci.* **6**, 15 (1996).
- [40] G. Kresse and J. Furthmüller, *Phys. Rev. B* **54**, 11169 (1996).
- [41] G. Kresse and D. Joubert, *Phys. Rev. B* **59**, 1758 (1999).
- [42] J. P. Perdew, K. Burke, and M. Ernzerhof, *Phys. Rev. Lett.* **77**, 3865 (1996).
- [43] M. Methfessel and A. T. Paxton, *Phys. Rev. B* **40**, 3616 (1989).
- [44] P. E. Blöchl, O. Jepsen, and O. K. Andersen, *Phys. Rev. B* **49**, 16223 (1994).
- [45] D. Hobbs, G. Kresse, and J. Hafner, *Phys. Rev. B* **62**, 11556 (2000).
- [46] M. Zelený, M. Šob, and J. Hafner, *Phys. Rev. B* **80**, 144414 (2009).
- [47] T. Asada and K. Terakura, *Phys. Rev. B* **47**, 15992 (1993).
- [48] The Wigner-Seitz radius  $R_{ws}$  is related to the volume per Mn atom  $V$  by:  $V = 4\pi/3R_{ws}^3$ .
- [49] Y. Endoh and Y. Ishikawa, *J. Phys. Soc. Jpn.* **30**, 1614 (1971).
- [50] R. Podloucky and J. Redinger, *J. Phys.: Condens. Matter* **31**, 054001 (2018).
- [51] I. Di Marco, J. Minár, S. Chadov, M. I. Katsnelson, H. Ebert, and A. I. Lichtenstein, *Phys. Rev. B* **79**, 115111 (2009).
- [52] I. Di Marco, J. Minár, J. Braun, M. I. Katsnelson, A. Grechnev, H. Ebert, A. I. Lichtenstein, and O. Eriksson, *Eur. Phys. J. B* **72**, 473 (2009).
- [53] S. Biermann, A. Dallmeyer, C. Carbone, W. Eberhardt, C. Pampuch, O. Rader, M. I. Katsnelson, and A. I. Lichtenstein, *JETP Lett.* **80**, 612 (2004).
- [54] F. C. Frank and J. S. Kasper, *Acta Cryst.* **11**, 184 (1958).
- [55] H. Fujihisa and K. Takemura, *Phys. Rev. B* **52**, 13257 (1995).
- [56] J. S. Kasper and B. W. Roberts, *Phys. Rev.* **101**, 537 (1956).
- [57] J. A. Oberteuffer, J. A. Marcus, L. H. Schwartz, and G. P. Felcher, *Phys. Lett. A* **28**, 267 (1968).
- [58] N. Kunitomi, T. Yamada, Y. Nakai, and Y. Fujii, *J. Appl. Phys.* **40**, 1265 (1969).
- [59] T. Yamada, N. Kunitomi, Y. Nakai, D. E. Cox, and G. Shirane, *J. Phys. Soc. Jpn.* **28**, 615 (1970).
- [60] H. Yamagata and K. Asayama, *J. Phys. Soc. Jpn.* **33**, 400 (1972).
- [61] In the fixed cell-shape calculations, the atomic positions were allowed to relax but the overall cell shape ( $c/a$  ratio) was kept fixed at the experimental value ( $c/a = 0.99955$ ). When both the cell shape and atom positions are allowed to relax, the  $c/a$  ratio becomes 1.002.
- [62] Y. S. Dedkov, E. N. Voloshina, and M. Richter, *Phys. Rev. B* **81**, 085404 (2010).
- [63] D. Mejía-Rodríguez and S. B. Trickey, *Phys. Rev. B* **100**, 041113(R) (2019).
- [64] F. G. Eich and E. K. U. Gross, *Phys. Rev. Lett.* **111**, 156401 (2013).
- [65] S. Pittalis, G. Vignale, and F. G. Eich, *Phys. Rev. B* **96**, 035141 (2017).
- [66] Interestingly, it is possible to stabilize a noncollinear solution for  $\gamma$ -Mn within SCAN. The collinear SCAN calculation yields  $R_{ws} = 2.732$  a.u. while the noncollinear calculation gives  $R_{ws} = 2.755$  a.u., which is in better agreement with the experimental value of  $R_{ws} = 2.752$  a.u. (The PBE value is  $R_{ws} = 2.635$  a.u.) Notably, the collinear SCAN result is only 3 meV/atom more stable than our noncollinear solution. Increase in the lattice constant for the noncollinear case is only 0.8%. The lattice expansion with noncollinearity in  $\gamma$ -Mn is thus not large.
- [67] N. Stojić and N. Binggeli, *J. Magn. Magn. Mater.* **320**, 100 (2008).
- [68] B. Barbiellini and A. Bansil, *J. Phys. Chem. Solids* **66**, 2192 (2005).
- [69] P. Entel, M. E. Gruner, M. Acet, A. Hucht, A. Çakır, R. Arróyave, I. Karaman, T. C. Duong, A. Talapatra, N. M. Bruno, D. Salas, S. Mankovsky, L. Sandratskii, T. Gottschall, O. Gutfleisch, S. Sahoo, S. Fähler, P. Lázpita, V. A. Chernenko, J. M. Barandiaran, V. D. Buchelnikov, V. V. Sokolovskiy, T. Lookman, and X. Ren, Probing glassiness in Heuslers via density functional theory calculations, in *Frustrated Materials and Ferroic Glasses*, edited by T. Lookman and X. Ren (Springer International Publishing, Cham, 2018), pp. 153–182.
- [70] V. D. Buchelnikov and V. V. Sokolovskiy, *Phys. Met. Metall.* **112**, 633 (2011).
- [71] A. Planes, L. Mañosa, and M. Acet, *J. Phys.: Condens. Matter* **21**, 233201 (2009).
- [72] R. Cardias, A. Szilva, A. Bergman, I. Di Marco, M. Katsnelson, A. Lichtenstein, L. Nordström, A. Klautau, O. Eriksson, and Y. O. Kvashnin, *Sci. Rep.* **7**, 4058 (2017).
- [73] C. P. Opeil, B. Mihaïla, R. K. Schulze, L. Mañosa, A. Planes, W. L. Hults, R. A. Fisher, P. S. Riseborough, P. B. Littlewood, J. L. Smith, and J. C. Lashley, *Phys. Rev. Lett.* **100**, 165703 (2008).
- [74] M. Ye, A. Kimura, Y. Miura, M. Shirai, Y. T. Cui, K. Shimada, H. Namatame, M. Taniguchi, S. Ueda, K. Kobayashi, R. Kainuma, T. Shishido, K. Fukushima, and T. Kanomata, *Phys. Rev. Lett.* **104**, 176401 (2010).
- [75] J. A. Weber, A. Bauer, P. Böni, H. Ceeh, S. B. Dugdale, D. Ernsting, W. Kreuzpaintner, M. Leitner, C. Pfleiderer, and C. Hugenschmidt, *Phys. Rev. Lett.* **115**, 206404 (2015).
- [76] B. Himmetoglu, V. M. Katukuri, and M. Cococcioni, *J. Phys.: Condens. Matter* **24**, 185501 (2012).



## Publication III

J. Nokelainen, C. Lane, R. S. Markiewicz, B. Barbiellini, A. Pulkkinen,  
B. Singh, J. Sun, K. Pussi and A. Bansil

***Ab initio* description of the  $\text{Bi}_2\text{Sr}_2\text{CaCu}_2\text{O}_{8+\delta}$  electronic structure**

Reprinted with permission from

*Physical Review B*

Vol. 101, pp. 214523, 2020

© 2020, American Physical Society.



**Ab initio description of the  $\text{Bi}_2\text{Sr}_2\text{CaCu}_2\text{O}_{8+\delta}$  electronic structure**

Johannes Nokelainen <sup>1,\*</sup> Christopher Lane,<sup>2,3,†</sup> Robert S. Markiewicz,<sup>4</sup> Bernardo Barbiellini <sup>1,4</sup> Aki Pulkkinen,<sup>5,1</sup> Bahadur Singh,<sup>4</sup> Jianwei Sun,<sup>6</sup> Katariina Pussi,<sup>1</sup> and Arun Bansil<sup>4</sup>

<sup>1</sup>Department of Physics, School of Engineering Science, LUT University, FI-53850 Lappeenranta, Finland

<sup>2</sup>Theoretical Division, Los Alamos National Laboratory, Los Alamos, New Mexico 87545, USA

<sup>3</sup>Center for Integrated Nanotechnologies, Los Alamos National Laboratory, Los Alamos, New Mexico 87545, USA

<sup>4</sup>Physics Department, Northeastern University, Boston, Massachusetts 02115, USA

<sup>5</sup>Département de Physique and Fribourg Center for Nanomaterials, Université de Fribourg, CH-1700 Fribourg, Switzerland

<sup>6</sup>Department of Physics and Engineering Physics, Tulane University, Louisiana 70118 New Orleans, USA



(Received 26 March 2020; revised manuscript received 20 May 2020; accepted 21 May 2020; published 26 June 2020)

Bi-based cuprate superconductors are important materials for both fundamental research and applications. As in other cuprates, the superconducting phase in the Bi compounds lies close to an antiferromagnetic phase. Our density functional theory calculations based on the strongly-constrained-and-appropriately-normed exchange correlation functional in  $\text{Bi}_2\text{Sr}_2\text{CaCu}_2\text{O}_{8+\delta}$  reveal the persistence of magnetic moments on the copper ions for oxygen concentrations ranging from the pristine phase to the optimally hole-doped compound. We also find the existence of ferrimagnetic solutions in the heavily doped compounds, which are expected to suppress superconductivity.

DOI: [10.1103/PhysRevB.101.214523](https://doi.org/10.1103/PhysRevB.101.214523)

**I. INTRODUCTION**

In 1986 superconductivity above 30 K was reported in  $\text{La}_2\text{CuO}_4$  by Bednorz and Müller [1], initiating an intense effort to understand its microscopic origin and gain insight into driving the  $T_c$  above the room temperature. The anomalous nature of the cuprate superconductivity is believed to originate from the quasi-two-dimensional  $\text{CuO}_2$  planes wherein a strong long-range antiferromagnetic (AFM) order is found in the parent half-filled compound [2]. On doping, the AFM order quickly disappears and gives way to a superconducting dome. From this intimate connection between antiferromagnetism and superconductivity, the view that spin-fluctuations play a central role in determining the physical properties of the cuprates has been gaining increasing support [3–5]. However, there is still no universally accepted explanation for high-temperature superconductivity.

Crucial to understanding the origin of superconductivity in the cuprates is the process by which doped hole carriers are introduced into the  $\text{CuO}_2$  planes. In simplified low-energy effective models, such as the one-band Hubbard model, only the Cu- $d$  and O- $p$  states are assumed to dominate. This view of the cuprates has been successful in describing the robust broken symmetry phases seen in experiments but it does not account for the diversity of transition temperatures at optimal doping. For example, the highest  $T_c$  obtained in  $\text{La}_{2-x}\text{Sr}_x\text{CuO}_4$  is 40 K, whereas in the single-layer Hg cuprate,  $\text{HgBa}_2\text{CuO}_4$ , the optimal  $T_c$  is almost 100 K, more than twice that of  $\text{La}_{2-x}\text{Sr}_x\text{CuO}_4$ . These variations have been accounted for by modifying the local crystal-field splittings in

the  $\text{CuO}_6$  octahedra [6], which in turn alter fine features of the Fermi surface [7]. However, these models ignore impurity and structural effects derived from real dopants. Moreover, such models do not account for interlayer coupling effects between the  $\text{CuO}_2$  planes and the charge-reservoir layers. Therefore, the doping process must be theoretically modeled in a holistic manner by treating the  $\text{CuO}_2$  plane, the surrounding layers, and the dopants on the same footing.

The bismuth-based cuprates  $\text{Bi}_2\text{Sr}_2\text{Ca}_{n-1}\text{Cu}_n\text{O}_{2n+4+\delta}$  (BSCCO) [8–12] are among the most extensively investigated superconductors. Notably, the weak van der Waals-like coupling between the layers, facilitates cleaving and makes BSCCO amenable to accurate angle resolved photoemission spectroscopy (ARPES) [13–21] and scanning-tunneling microscopy/spectroscopy (STM/STS) [22–31] studies. The two-layer compound ( $n = 2$ ) is composed of a rock-salt  $\text{SrO-BiO}_8\text{-SrO}$  charge reservoir layer stacked with two  $\text{CuO}_2\text{-Ca-CuO}_2$  layers. Unlike the mercury- or yttrium-based cuprates, the oxygen impurities in BSCCO can occupy at least three distinct sites. These sites have been extensively studied with STM, and the findings have been compared to various models [32–34].

Initial theoretical studies of cuprates using the density functional theory (DFT) missed important Coulomb correlation effects [35]. In BSCCO, the local-spin-density-approximation (LSDA) fails to produce the copper magnetic moments [36–40]. The generalized-gradient-approximation (GGA) produces only marginal corrections to the LSDA [34,41–44]. Jarlborg has suggested applying higher-order density gradient corrections to cuprates [45]. Additional studies beyond the GGA using schemes such as DFT +  $U$  [46] and DFT + DMFT [47] have been performed to stabilize the AFM ground state. However, these methods

\*johannes.nokelainen@lut.fi

†laneca@lanl.gov

require the use of external parameters such as the Hubbard  $U$ , which limits the predictive power of the theory.

Recent progress on advanced DFT schemes offers new pathways for describing the electronic structure of correlated materials from first principles. In particular, the strongly-constrained-and-appropriately-normed (SCAN) meta-GGA exchange-correlation functional [48], which obeys all known constraints applicable to meta-GGA, has been shown to accurately predict many of the key properties of pristine and doped  $\text{La}_2\text{CuO}_4$  [49–51] and  $\text{YBa}_2\text{Cu}_3\text{O}_6$  [52]. In  $\text{La}_2\text{CuO}_4$ , SCAN correctly captures the magnetic moment in magnitude and orientation, the magnetic exchange coupling parameter, and the magnetic form factor along with the electronic band gap, all in accord with the corresponding experimental results. Reference [51] compares SCAN with other meta-GGA and hybrid functionals in cuprates and shows that SCAN gives the best overall agreement with experiments. In a SCAN-based study, Ref. [52] identifies a landscape of 26 competing uniform and stripe phases in near-optimally doped  $\text{YBa}_2\text{Cu}_3\text{O}_7$ . In Ref. [52], the charge, spin and lattice degrees of freedom are treated on an equal footing in a fully self-consistent manner to show how stable stripe phases can be obtained without invoking any free parameters. These results indicate that SCAN correctly captures many key features of the electronic and magnetic structures of the cuprates and it thus provides a next-generation baseline for incorporating the missing many-body effects such as the quasiparticle lifetimes and waterfall features [53]. The applicability of SCAN to transition-metal oxides, semiconductors, and atomically thin films beyond graphene has been demonstrated in Refs. [54–62]. We note that SCAN also contains overcorrections to the GGA in dealing with itinerant ferromagnetism [63,64], but the underlying deficiencies responsible for these issues with SCAN have been identified and possible fixes have been proposed [65,66]. There is no evidence that these issues with SCAN persist outside of the ferromagnets, since SCAN clearly improves GGA in the case of antiferromagnetic  $\alpha$ -Mn [67].

In this article, we utilize the SCAN functional to explore the electronic, structural and magnetic properties of  $\text{Bi}_2\text{Sr}_2\text{CaCu}_2\text{O}_8$  ( $\text{Bi}2212$ ) on a first-principles basis. A realistic description of the phase diagram of BSCCO requires also an accurate treatment of the self-doping by the BiO layers and a precise description of the oxygen interstitials, which can occupy different sites. We will show that a robust copper magnetic moment persists even when a substantial amount of oxygen is added to the material, which is in agreement with recent resonant inelastic x-ray spectroscopy (RIXS) experiments [68–71]. The appearance of the Cu magnetic moment in SCAN continues to capture other good trends seen in the LDA and GGA computations [40]. Finally, we find that SCAN predicts ferrimagnetic solutions in overdoped BSCCO in agreement with recent experiments by Kurashima *et al.* [72].

This paper is organized as follows. Section II discusses the methodology, where Sec. II A describes the computational details and Sec. II B considers the structural models for BSCCO. Section III presents the results of this study. Here, Sec. II A focuses on pristine Bi2212 while Secs. III B and III C present the results for oxygen-doped BSCCO with O impurities located at various positions in the lattice. Section IV summarizes our conclusions and comments on future implications of our work.

## II. METHODOLOGY

### A. Computational details

*Ab initio* calculations were carried out using the projector-augmented-wave method [73,74] as implemented in the Vienna *ab initio* simulation package [75,76]. The Kohn-Sham orbitals [77] were expanded in a plane-wave basis set with an energy cutoff of 550 eV. The exchange-correlation energy is treated within the SCAN meta-GGA scheme [48]. Some calculations were also carried out within the GGA scheme of Perdew, Burke, and Ernzerhof [78] for reference. All sites in the unit cell along with the unit cell dimensions were relaxed using a quasi-Newton algorithm to minimize energy with an atomic force tolerance of 0.001 eV/Å. A  $9 \times 9 \times 2$  ( $4 \times 4 \times 1$   $k$ -mesh was used to sample the Brillouin zone of the bulk (slab) crystal structure and a denser  $15 \times 15 \times 3$   $k$ -mesh was employed to calculate the density of states (DOS). A total energy tolerance of  $10^{-5}$  eV was used to determine the self-consistent charge density. The band structure was unfolded [79,80] from the supercell into the primitive cell Brillouin zone using the PYPROCAR [81] code. Various site-resolved projections were analyzed with the PYMATGEN [82] software package.

### B. Structural model of BSCCO

An important characteristic of the cuprates is the presence of an intrinsic lattice mismatch between the various layers [83]. In BSCCO, the substantial tensile stress in the BiO layers leads to an incommensurate superlattice modulation [84] in which the  $\text{CuO}_2$  and BiO layers undergo warping and rippling with an approximate period of five unit cells along the  $b$  axis. The reported effects of this supermodulation on the electronic properties have been mixed in that ARPES finds no effect on  $T_c$  as a function of superstructure period [85], whereas STM finds the local doping level to be connected to the periodicity of the structural modulations [86]. A few theoretical studies have been performed within the DFT [34,42] but clear conclusions have been difficult to obtain due to the intrinsic limitations of the LSDA and GGA.

In this study, we neglect the superstructure modulation and focus on the electronic and magnetic properties and their evolution with doping. In this connection, we consider a  $\sqrt{2} \times \sqrt{2}$  orthorhombic supercell to accommodate the  $(\pi, \pi)$  AFM order on the copper atomic sites (see Fig. 1). After relaxing the atomic positions and unit-cell shape, we find the  $a$ ,  $b$ , and  $c$  lattice parameters to be 5.35 Å, 5.42 Å, and 31.08 Å, respectively, admitting a 1.1% orthorhombicity in the  $ab$  plane. These parameters are in good accord with the corresponding experimental results [ $a = 5.399(2)$  Å,  $b = 5.414(1)$  Å, and  $c = 30.904(16)$  Å] [8]. Interestingly, in comparison to a freestanding BiO bilayer, our computations show that the BiO bilayer in BSCCO is under a tensile strain of 9.3% due to lattice mismatch [87]. Consequently, the Bi and O ions rearrange themselves and exhibit stronger BiO bonding along the  $a$  axis compared to the  $b$  axis, yielding zig-zag BiO chains or  $\text{Bi}_2\text{O}_2$  quadrilaterals [42,88,89]. The chain formation appears to be key for stabilizing the orthorhombic ground state.

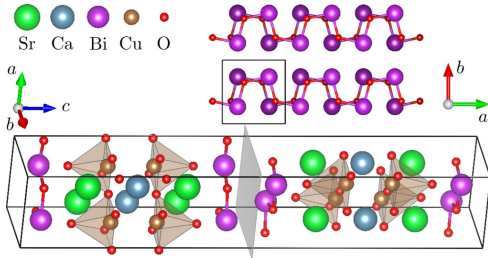


FIG. 1. A schematic of the relaxed orthorhombic  $\sqrt{2} \times \sqrt{2}$  supercell structure of Bi2212 and the zigzag chains of BiO bilayers. This zigzag stacking configuration within the BiO bilayers yielded the lowest energy. The vdW gap in the BiO layer (highlighted with the gray plane) divides the structure into two slabs. Black lines mark the computational unit cell.

In order to delineate effects of doping, we doubled the unit cell in the  $ab$  plane. Since the bulk Bi2212 crystal consists of two formula units stacked body-center-wise and separated by a van der Waals (vdW) region with very little  $k_z$  dispersion [90], we followed previous computational studies [33,41,43] and considered only one formula unit. Using a small vacuum region of 3.8 Å to separate the periodic images of these slabs, we verified that the electronic properties of this simplified model correspond well to those of the bulk.

### III. RESULTS

#### A. Electronic structure of pristine Bi2212

Figure 2 compares band structures and site-resolved partial-densities-of-states (PDOSs) of Bi2212 obtained within the GGA and SCAN schemes. Consistent with previous *ab initio* studies [40,43], GGA [Fig. 2(a)] yields a non-magnetic metal, where the spin-degenerate Cu  $d_{x^2-y^2}$  bands cross the Fermi level with an overall bandwidth of 4.0 eV. In contrast, SCAN [Fig. 2(b)] stabilizes the AFM order over the copper sublattice and produces an indirect gap of 0.33 eV in the half-filled  $d_{x^2-y^2}$ -dominated band. At the  $X$  point, the energy gap is 1.47 eV, while at the midpoint between  $M$  and  $\Gamma$  [91], the gap is 1.24 eV. When the band structure is projected onto the Cu ions with positive magnetic moments [Fig. 2(c)], the spin-polarized nature of the Cu  $d_{x^2-y^2}$  bands become visible. The valence band (majority spin) is now seen to be partially occupied, while the conduction band (minority spin) is unoccupied, leading to local Cu magnetic moments of  $\pm 0.425 \mu_B$ . Around  $X$ , the valence bands exhibit a bilayer splitting of 0.24 eV, which produces two van Hove singularities visible in the PDOS at around  $-0.65$  eV and  $-0.88$  eV. These singularities visually appear to be stronger than logarithmic, in agreement with Nieminen *et al.* [27]. The Cu  $d_{z^2}$  and  $t_{2g}$  orbitals are spin-split due to the Hund's coupling [see Fig. 2(b)]. This splitting is substantial for the  $d_{z^2}$  orbitals but weak for the  $t_{2g}$  orbitals; we find that the  $d_{z^2}$  orbitals contribute mainly between  $-1.7$  eV and  $-2.2$  eV in the spin up channel and between  $-2.7$  eV and  $-3.2$  eV in the spin down channel. In contrast, the  $t_{2g}$  majority and minority

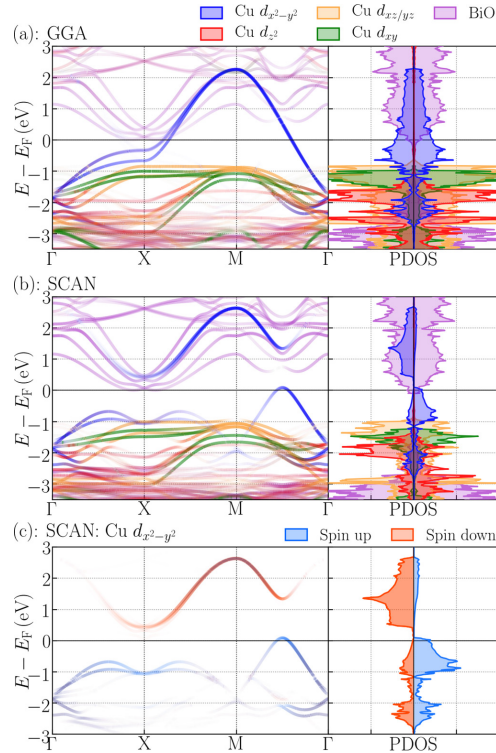


FIG. 2. [(a) and (b)] Band structure and DOS projected onto Cu  $d$  orbitals and BiO layers for GGA and SCAN. For SCAN, the Cu projections refer only to Cu ions with positive magnetic moments in order to highlight their spin polarization in PDOS (the total moment over the unit cell is zero). However, the spin polarization is not shown in the band structure plots for simplicity. (c): SCAN-based Cu  $d_{x^2-y^2}$  bands and DOS. Here, spin polarization of the band structure is shown. Band structure has been unfolded [79,80] into the primitive cell from the AFM  $\sqrt{2} \times \sqrt{2}$  supercell.  $X$  and  $M$  symmetry points are given with respect to the Brillouin zone of the primitive cell.

spin states are nearly degenerate, with the weight of  $d_{xz/yz}$  orbitals concentrated between  $-1.7$  eV and  $-1.0$  eV, and that of  $d_{xy}$  orbitals between  $-2.0$  eV and  $-1.2$  eV. Hund's coupling leads to similar orbital splitting behavior in  $\text{La}_2\text{CuO}_4$ , but with different ordering of the  $d$  orbitals [49]. Here, the  $d_{z^2}$  bands are below the  $t_{2g}$  bands, whereas in  $\text{La}_2\text{CuO}_4$  they are the highest fully occupied bands. This difference between Bi2212 and  $\text{La}_2\text{CuO}_4$  is a consequence of the larger separation between the Cu ions and the apical oxygen atoms in Bi2212; 2.67 Å in our relaxed structure compared to 2.45 Å in  $\text{La}_2\text{CuO}_4$  [49].

In order to estimate the value of on-site Hubbard potential  $U$  and the Hund's coupling  $J_H$ , we follow the approach of Lane *et al.* [49]. Using the PDOSs  $g_{\mu\sigma}$  resolved by orbitals  $\mu$  and spin  $\sigma$ , we determine the average spin-splitting

$\bar{E}_{\mu\sigma}$  of the  $d_{x^2-y^2}$  and  $d_{z^2}$  levels and then  $U$  and  $J_H$  as follows:

$$\bar{E}_{\mu\sigma} = \int_W E g_{\mu\sigma}(E) dE, \quad (1)$$

$$\bar{E}_{d_{x^2-y^2}\uparrow} - \bar{E}_{d_{x^2-y^2}\downarrow} = U(N_\uparrow - N_\downarrow), \quad (2)$$

$$\bar{E}_{\mu\neq d_{x^2-y^2}\uparrow} - \bar{E}_{\mu\neq d_{x^2-y^2}\downarrow} = J_H(N_\uparrow - N_\downarrow), \quad (3)$$

where  $N_\uparrow$  ( $N_\downarrow$ ) is the occupation of the spin-up (down)  $d_{x^2-y^2}$  orbital and the integration is over the full bandwidth  $W$ . In this way,  $U$  and  $J_H$  ( $\mu = d_{z^2}$ ) are found to be 4.7 eV and 1.35 eV, respectively. These values are very similar to those found for  $\text{La}_2\text{CuO}_4$  [49]. Also, this value of  $U$  is comparable to that found in the three-band Hubbard models of cuprates, but it is substantially larger than the  $U$  used in the single-band Hubbard model, which can be estimated through a constrained random phase approximation calculation [92] for  $\text{Bi}_2\text{212}$  [93] and  $\text{Bi}_2\text{Sr}_2\text{CuO}_6$  ( $\text{Bi}2201$ ) [70]. This difference is due to the over-simplified nature of the single-band model, where the band is composed of  $\text{Cu-}d_{x^2-y^2}$  and  $\text{O-}p_x, p_y$  characters. This band thus essentially represents a  $\text{CuO}_2$  molecule instead of a pure  $d$  state, so that the  $U$  estimated in this way involves partial screening by the O ligands.

The nearest-neighbor superexchange coupling parameter  $J$  is usually estimated by mapping to an effective Heisenberg model [49]. However, this is not possible here because we found that the ferromagnetic state in this case converges to zero magnetic moment. For this reason, we have used  $J \approx 4t^2/U - 24t^4/U^3$ , where  $t$  is the nearest-neighbor hopping parameter, which can be estimated from the  $d_{x^2-y^2}$  bandwidth  $B$  to be  $t = B/8 \approx 500$  meV. We thus estimate  $J \approx 200$  meV, which is in reasonable accord with the corresponding experimental value of  $\sim 148$  meV [70].

Unlike the other cuprates such as  $\text{La}_2\text{CuO}_4$ , pristine BSCCO is weakly metallic due to self-doping [40]: Both the BiO and Cu  $d_{x^2-y^2}$  bands cross  $E_F$  and lead to a semimetal through the removal of some electrons from the  $\text{CuO}$  plane. This self-doping effect may be the reason that it has been difficult to stabilize a large magnetic gap in nominally pristine BSCCO without rare-earth substitution [94,95]. We have also carried out computations on  $\text{Bi}2201$  (see Supplementary Materials [96,97] for comparison of  $\text{Bi}2201$  with  $\text{Bi}2212$ ). Notably, the Cu magnetic moment in  $\text{Bi}2201$  is found to be  $0.395 \mu_B$ , which is  $0.030 \mu_B$  less than in  $\text{Bi}2212$ . This reflects the effect of stronger self-doping in  $\text{Bi}2201$  where the Bi/Cu ratio is twice as large as in  $\text{Bi}2212$ .

### B. Doping of $\text{Bi}2212$

STM studies of Zeljkovic *et al.* [32,33] show that there are two different types of interstitial oxygen dopants in BSCCO. The “type B” dopants reside in the BiO layers, whereas the “type A” oxygens lie close to the apical oxygen atoms and the SrO layers and interact directly with the  $\text{CuO}_2$  planes. We have modeled both types of these dopants and found that the type A oxygen dopants explain most of the observed hole-type doping. The B oxygen dopants are discussed further in Sec. III C below. Our calculations for modeling doping effects employed a 120-atom  $2\sqrt{2} \times 2\sqrt{2}$  supercell slab (see

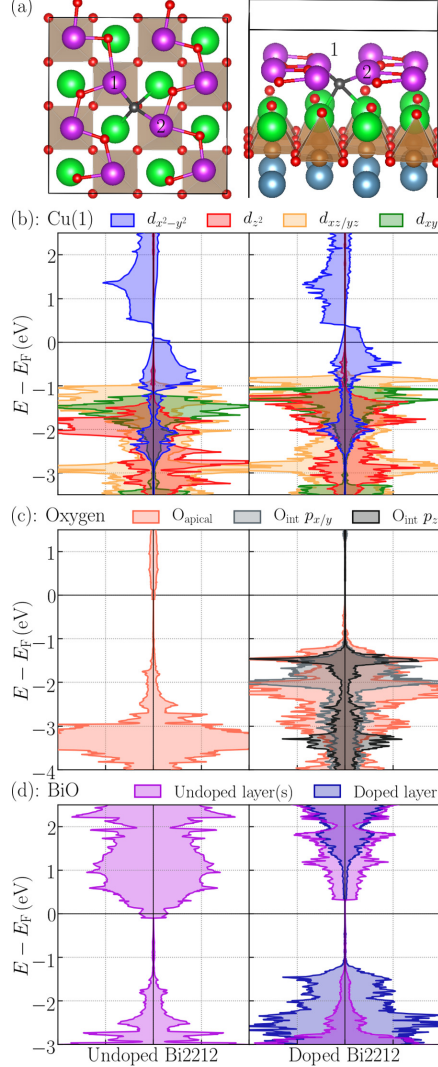


FIG. 3. (a) Top and side views of the relaxed  $\text{Bi}2212$  slab with an A-type O dopant.  $\text{O}_{\text{int}}$  is colored black. The  $\text{Cu}(1)/\text{Cu}(2)$  and the  $\text{O}_{\text{apical}}(1)/\text{O}_{\text{apical}}(1)$  atoms are located below the Bi atoms labeled 1/2. (b)  $lm$ -decomposed PDOS of the  $\text{Cu}(1)$  ion [closest to  $\text{O}_{\text{int}}$ , see panel (a)] in pristine (left) and doped (right) cases. (c)  $p$ -projected PDOS of the  $\text{O}_{\text{apical}}(1)$  atom with and without doping. For the doped case (right), the PDOS of the  $\text{O}_{\text{int}}$  is also presented. (d) PDOS projected onto the BiO layers.

Sec. II for details) with a type A interstitial oxygen atom  $\text{O}_{\text{int}}$ . This model corresponds to a doping level of  $\delta = 1/8$  (close to optimal doping), as illustrated in Fig. 3(a). In the

relaxed structure the  $O_{\text{int}}$  atom is found to reside between the SrO and BiO layers in agreement with the results of He *et al.* [41,42] and Foyevtsova *et al.* [43] as well as with a recent scanning-transmission-electron microscopy (STEM) study by Song *et al.* [34].

In Fig. 3(b), we illustrate the effects of dopant on the electronic structure by comparing the pristine and doped PDOS on Cu(1) site, which is the copper ion closest to the  $O_{\text{int}}$ . Doping leads to addition of holes resulting into a downwards shift of the Fermi level in the magnetic  $d_{x^2-y^2}$  band, along with the closing of the  $d_{x^2-y^2}$  electronic gap. The doping leads to a reduction in the average value of the Cu magnetic moment ( $|M| = 0.347 \mu_B$ ) by  $0.078 \mu_B$ . Values of  $|M|$  differ significantly between the two  $\text{CuO}_2$  planes. We will refer to the  $\text{CuO}_2$  planes with/without the dopant as “doped/undoped” planes. On the undoped plane,  $|M| = 0.363 \mu_B$ , whereas on the doped plane, the magnetic moments are on average  $0.328 \mu_B$  with significant variations on Cu sites ( $0.322 \mu_B \leq |M| \leq 0.339 \mu_B$ ). The on-site potential of about 4.8 eV, calculated from the Cu  $d_{x^2-y^2}$  PDOS, is constant for all the Cu sites and remains almost unchanged from the pristine case.

Note that the O dopant here resides between the apical oxygen atoms  $O_{\text{apical}}(1)$  and  $O_{\text{apical}}(2)$  at distances of 2.61 Å and 2.66 Å, respectively [see Fig. 3(a)]. The  $O_{\text{int}}$  interacts with the Cu(1)  $d_{z^2}$  orbitals primarily through  $O_{\text{apical}}(1)$ . However, as discussed in Sec. III A, this interaction is suppressed in BSCCO compared to other cuprates due to the larger Cu– $O_{\text{apical}}$  separation. Lack of hybridization in the pristine case can be seen by comparing the Cu(1)  $d_{z^2}$  and  $O_{\text{apical}}(1)$  PDOSs on the left sides of Figs. 3(b) and 3(c). In the doped case, the coupling between the Cu(1)/Cu(2) ions and the  $O_{\text{apical}}(1)/O_{\text{apical}}(2)$  atoms is significantly enhanced because of 0.18 Å reduction of their separations to 2.49 Å. Consequently, the  $O_{\text{apical}}(1)$  states are lifted from below  $-3$  eV to the energy interval of  $-3$  eV to  $-1$  eV, as shown in Fig. 3(c). This modified  $O_{\text{apical}}(1)$  PDOS displays strong common features with the Cu(1)  $d_{z^2}$  states as illustrated in the right side of Fig. 3(b). These results indicate substantial doping-induced interactions between these atoms. On the Cu(1) ion, the effect of these interactions is to lift the  $d_{z^2}$  orbitals by  $\sim 0.3$  eV with respect to the  $t_{2g}$  orbitals, which can be seen by comparing their average energies computed with Eq. (1). In addition, the shape of the Cu(1)  $d_{z^2}$  PDOS experiences significant modification. However, the estimated Hund’s splitting (1.38 eV) remains almost unchanged. The overall trends described above are also present on the other Cu sites in a less pronounced form.

The right side of Fig. 3(c) gives insight into the nature of  $O_{\text{int}}$  PDOS. By comparing PDOSs of  $O_{\text{int}}$  and  $O_{\text{apical}}(1)$  we see that both  $p_{x/y}$  and  $p_z$  orbitals of  $O_{\text{int}}$  couple with  $O_{\text{apical}}(1)$ , with  $p_z$  coupling around  $-1.4$  eV and  $p_{x/y}$  around  $-2.0$  eV. The  $O_{\text{int}}$   $p_z$  PDOS is especially relevant for STM experiments since the tunneling involves the  $p_z$  orbital while the  $p_x/p_y$  orbitals are orthogonal to the STM tip [98]. Indeed, STM studies by Zeljkovic *et al.* [32,33] report a peak in the scanning-tunneling spectrum at  $-1.5$  eV for the type A interstitial, which is close to the aforementioned  $O_{\text{int}}$   $p_z$  PDOS peak at  $-1.4$  eV.

Figure 3(d) shows the BiO-layer PDOS with and without the dopants. Doping is seen to lift the BiO bands above  $E_F$  in

accord with the study of Lin *et al.* [40] and Bi2223 study of Camargo-Martínez *et al.* [44] where doping was done with Pb instead of O. Note that BiO pockets are removed also from BiO layer which does not lie close to the  $O_{\text{int}}$  although effects of dopant on this “undoped” layer are relatively weak. In contrast, the dopant induces substantial effects on the electronic states from the “doped” BiO layer (i.e. the layer close to  $O_{\text{int}}$ ) where the spectral weights associated with the BiO states are lifted upwards by more than 1 eV and the BiO bands now overlap the Cu  $d$  bands in energy.

We also investigated the heavily overdoped regime ( $\delta = 1/4$ ) by introducing a second type-A dopant that was placed in the structure as far as possible from the first dopant. Compared to  $\delta = 1/8$ , the average value of  $|M|$  of the Cu ions in the overdoped case is lowered by  $0.078 \mu_B$  to  $0.268 \mu_B$ . Interestingly, the higher doping also leads to the onset of ferromagnetic order with average spin up/down moments on Cu atoms of  $0.307 \mu_B / -0.229 \mu_B$ . Moreover, the oxygen atoms in the  $\text{CuO}_2$  planes now develop a magnetic moment of  $+0.010 \mu_B$ . The total magnetization of the unit cell is  $0.059 \mu_B$  per copper. Such magnetization has been predicted to destroy superconductivity in overdoped cuprates [72,99,100].

### C. Type B oxygen dopants

Following the experimental results of Zeljkovic *et al.* [32,33] and the computational study of He *et al.* [41], we placed the-type B oxygen dopants in the middle of the approximately square Bi network (position #2 of He *et al.*). This location is quite close to one of the oxygen atoms in the BiO layer and leads to the formation of an oxygen molecule as shown in Fig. 4(a). We find the bond length of this oxygen dimer to be 1.476 Å, which is close to the  $[\text{O}_2]^{2-}$  bond length in  $\text{BaO}_2$  of 1.49 Å [101]. This  $O_{\text{int}}$  stabilizes into a position slightly below the BiO layer, while the oxygen which it is attached lies above the BiO layer, so that the dimer is tilted by an angle of  $33^\circ$  from the  $c$  axis. The total energy of the type B-doped compound was found to be 2.27 eV higher than that of the type A-doped structure.

In contrast to our results for the type A interstitial O atom, we found that the B interstitials produce only little doping, with the Cu magnetic moments being decreased only by  $0.014 \mu_B$  to  $0.402 \mu_B$ . The Cu  $d_{x^2-y^2}$  state remains nearly unchanged, as seen from the PDOS in Fig. 4(b), and the BiO pocket is not lifted above  $E_F$ , as illustrated in Fig. 4(d). In the PDOS of the  $O_{\text{int}}$ , a clear peak appears at around  $-2.6$  eV. This feature is also reflected in the PDOS of the  $O_{\text{apical}}$  [see Fig. 4(c)] and in the PDOS of the Cu  $d_{z^2}$  [see Fig. 4(b)], indicating that some interactions occur also between the type B  $O_{\text{int}}$  and the  $\text{CuO}_2$  plane.

We also tested the interstitial oxygen position in the van der Waals gap between the BiO layers. The energy of this configuration was found to be between that of type A and B oxygen atoms. To the best of our knowledge, this impurity position has not been considered in the literature. A possible explanation is that these oxygen atoms are very mobile and therefore they disappear during the annealing of the material or combine with existing oxygens in the BiO layer to become type B oxygens. Additionally, they might be more sensitive to

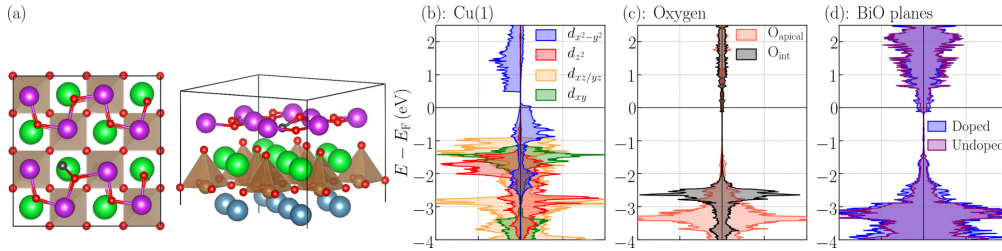


FIG. 4. (a) Structural model of a type B O-dopant in Bi2212. O<sub>int</sub> is colored black. (b) PDOS of various  $d$  orbitals of a copper atom close to the O<sub>int</sub>. (c) PDOS of the  $p$  orbitals of the O<sub>int</sub> and an apical oxygen atom close to the dopant. (d) PDOS projected onto the BiO layers with and without the dopant.

the supermodulation distortions, which are not considered in our structural model.

#### IV. SUMMARY AND CONCLUSIONS

We have discussed the electronic structure of BSCCO compounds using accurate first-principles computations based on the SCAN functional, which does not require the introduction of any arbitrary parameters (e.g., the Hubbard  $U$ ) to describe Coulomb correlation effects. As in our previous investigations of various cuprates, SCAN is found to greatly improve the description of the electronic states in the BSCCO system. In particular, our results yield accurate lattice geometries, copper magnetic moments and band structures that are in better agreement with experiments than GGA. The copper magnetic moments exhibit an antiferromagnetic coupling with and without oxygen dopants in accord with RIXS measurements, suggesting that superconductivity could be connected with quasiparticles coupled to spin fluctuations [5]. Oxygen dopants are shown to increase the coupling between the apical oxygens and the CuO<sub>2</sub> layers and modify especially the Cu  $d_{z^2}$  states. We also find the appearance of a doping-induced ferrimagnetic order that could be responsible for the suppression of superconductivity in the overdoped regime. The competition between superconductivity and ferrimagnetism hints that further studies of overdoped BSCCO could clarify important open questions such as the observation of a second dome of higher temperature superconductivity in the cuprates [102].

#### ACKNOWLEDGMENTS

It is a pleasure to acknowledge important discussions with Giacomo Ghiringhelli, Marco Moretti, and Xingjiang Zhou. The authors acknowledge CSC-IT Center for Science, Finland, for computational resources. J.N. is supported by the Finnish Cultural Foundation. The work at Northeastern University was supported by the US Department of Energy (DOE), Office of Science, Basic Energy Sciences Grant No. DE-FG02-07ER46352 (core research) and benefited from Northeastern University's Advanced Scientific Computation Center (ASCC), the NERSC supercomputing center through DOE Grant No. DE-AC02-05CH11231, and support (testing efficacy of advanced functionals) from the DOE EFRC: Center for Complex Materials from First Principles (CCM) under Grant No. DE-SC0012575. C.L. was supported by the US DOE NNSA under Contract No. 89233218CNA000001 and by the Center for Integrated Nanotechnologies, a DOE BES user facility, in partnership with the LANL Institutional Computing Program for computational resources. Additional support was provided by DOE Office of Basic Energy Sciences Program E3B5. B.B. acknowledges support from the COST Action CA16218. A.P. acknowledges the Osk. Hutunen Foundation for financial support. J.S. was supported by the US Department of Energy under EPSCoR Grant No. DE-SC0012432 with additional support from the Louisiana Board of Regents.

- [1] J. G. Bednorz and K. A. Müller, *Z. Phys. B Condens. Matter* **64**, 189 (1986).
- [2] J. M. Tranquada, G. Xu, and I. A. Zaliznyak, *J. Magn. Magn. Mater.* **350**, 148 (2014).
- [3] D. J. Scalapino, E. Loh, and J. E. Hirsch, *Phys. Rev. B* **34**, 8190 (1986).
- [4] D. J. Scalapino, *Phys. Rep.* **250**, 329 (1995).
- [5] D. J. Scalapino, *Rev. Mod. Phys.* **84**, 1383 (2012).
- [6] E. Pavarini, I. Dasgupta, T. Saha-Dasgupta, O. Jepsen, and O. K. Andersen, *Phys. Rev. Lett.* **87**, 047003 (2001).
- [7] H. Sakakibara, H. Usui, K. Kuroki, R. Arita, and H. Aoki, *Phys. Rev. Lett.* **105**, 057003 (2010).
- [8] M. A. Subramanian, C. C. Torardi, J. C. Calabrese, J. Gopalakrishnan, K. J. Morrissey, T. R. Askew, R. B. Flippin, U. Chowdhry, and A. W. Sleight, *Science* **239**, 1015 (1988).
- [9] J. M. Tarascon, Y. LePage, L. H. Greene, B. G. Bagley, P. Barboux, D. M. Hwang, G. W. Hull, W. R. McKinnon, and M. Giroud, *Phys. Rev. B* **38**, 2504 (1988).
- [10] J. M. Tarascon, W. R. McKinnon, P. Barboux, D. M. Hwang, B. G. Bagley, L. H. Greene, G. W. Hull, Y. LePage, N. Stoffel, and M. Giroud, *Phys. Rev. B* **38**, 8885 (1988).
- [11] E. Sterpetti, J. Biscaras, A. Erb, and A. Shukla, *Nat. Commun.* **8**, 2060 (2017).

- [12] S. Y. Frank Zhao, N. Poccia, M. G. Panetta, C. Yu, J. W. Johnson, H. Yoo, R. Zhong, G. D. Gu, K. Watanabe, T. Taniguchi, S. V. Postolova, V. M. Vinokur, and P. Kim, *Phys. Rev. Lett.* **122**, 247001 (2019).
- [13] P. Aebi, J. Osterwalder, P. Schwaller, L. Schlapbach, M. Shimoda, T. Mochiku, and K. Kadowaki, *Phys. Rev. Lett.* **72**, 2757 (1994).
- [14] N. L. Saini, J. Avila, A. Biaconi, A. Lanzara, M. C. Asensio, S. Tajima, G. D. Gu, and N. Koshizuka, *Phys. Rev. Lett.* **79**, 3467 (1997).
- [15] H. Ding, J. R. Engelbrecht, Z. Wang, J. C. Campuzano, S.-C. Wang, H.-B. Yang, R. Rogan, T. Takahashi, K. Kadowaki, and D. G. Hinks, *Phys. Rev. Lett.* **87**, 227001 (2001).
- [16] K. M. Lang, V. Madhavan, J. E. Hoffman, E. W. Hudson, H. Eisaki, S. Uchida, and J. C. Davis, *Nature* **415**, 412 (2002).
- [17] A. Damascelli, Z. Hussain, and Z.-X. Shen, *Rev. Mod. Phys.* **75**, 473 (2003).
- [18] T. L. Miller, M. Årriälä, C. L. Smallwood, W. Zhang, H. Hafiz, B. Barbiellini, K. Kurashima, T. Adachi, Y. Koike, H. Eisaki, M. Lindroos, A. Bansil, D.-H. Lee, and A. Lanzara, *Phys. Rev. B* **91**, 085109 (2015).
- [19] K. Gottlieb, C.-Y. Lin, M. Serbyn, W. Zhang, C. L. Smallwood, C. Jozwiak, H. Eisaki, Z. Hussain, A. Vishwanath, and A. Lanzara, *Science* **362**, 1271 (2018).
- [20] Y. Ding, L. Zhao, H.-T. Yan, Q. Gao, J. Liu, C. Hu, J.-W. Huang, C. Li, Y. Xu, Y.-Q. Cai *et al.*, *Chin. Phys. Lett.* **36**, 017402 (2019).
- [21] P. Ai, Q. Gao, J. Liu, Y. Zhang, C. Li, J. Huang, C. Song, H. Yan, L. Zhao, G.-D. Liu *et al.*, *Chin. Phys. Lett.* **36**, 067402 (2019).
- [22] B. Barbiellini, O. Fischer, M. Peter, C. Renner, and M. Weger, *Physica C* **220**, 55 (1994).
- [23] K. McElroy, R. W. Simmonds, J. E. Hoffman, D.-H. Lee, J. Orenstein, H. Eisaki, S. Uchida, and J. C. Davis, *Nature* **422**, 592 (2003).
- [24] A. C. Fang, L. Capriotti, D. J. Scalapino, S. A. Kivelson, N. Kaneko, M. Greven, and A. Kapitulnik, *Phys. Rev. Lett.* **96**, 017007 (2006).
- [25] O. Fischer, M. Kugler, I. Maggio-Aprile, C. Berthod, and C. Renner, *Rev. Mod. Phys.* **79**, 353 (2007).
- [26] L. Dudy, C. Janowitz, O. Lübben, B. Müller, A. Ariffin, A. Krapf, H. Dwelk, and R. Manzke, *J. Supercond. Nov. Magn.* **22**, 51 (2009).
- [27] J. Nieminen, I. Suominen, T. Das, R. S. Markiewicz, and A. Bansil, *Phys. Rev. B* **85**, 214504 (2012).
- [28] P. Mistark, R. S. Markiewicz, and A. Bansil, *Phys. Rev. B* **91**, 140501(R) (2015).
- [29] C.-T. Kuo, S.-C. Lin, G. Conti, S.-T. Pi, L. Moreschini, A. Bostwick, J. Meyer-Ilse, E. Gullikson, J. B. Kortright, S. Nemšák, J. E. Rault, P. Le Fèvre, F. Bertran, A. F. Santander-Syro, I. A. Vartanyants, W. E. Pickett, R. Saint-Martin, A. Taleb-Ibrahimi, and C. S. Fadley, *Phys. Rev. B* **98**, 155133 (2018).
- [30] H. Li, X. Zhou, S. Parham, T. J. Reber, H. Berger, G. B. Arnold, and D. S. Dessau, *Nat. Commun.* **9**, 1 (2018).
- [31] Y. Yu, L. Ma, P. Cai, R. Zhong, C. Ye, J. Shen, G. D. Gu, X. H. Chen, and Y. Zhang, *Nature* **575**, 156 (2019).
- [32] I. Zeljkovic, Z. Xu, J. Wen, G. Gu, R. S. Markiewicz, and J. E. Hoffman, *Science* **337**, 320 (2012).
- [33] I. Zeljkovic, J. Nieminen, D. Huang, T.-R. Chang, Y. He, H.-T. Jeng, Z. Xu, J. Wen, G. Gu, H. Lin, R. S. Markiewicz, A. Bansil, and J. E. Hoffman, *Nano Lett.* **14**, 6749 (2014).
- [34] D. Song, X. Zhang, C. Lian, H. Liu, I. Alexandrou, I. Lazić, E. G. T. Bosch, D. Zhang, L. Wang, R. Yu, Z. Cheng, C. Song, X. Ma, W. Duan, Q. Xue, and J. Zhu, *Adv. Funct. Mater.* **29**, 1903843 (2019).
- [35] W. E. Pickett, *Rev. Mod. Phys.* **61**, 433 (1989).
- [36] S. Massidda, J. Yu, and A. Freeman, *Physica C* **152**, 251 (1988).
- [37] L. F. Mattheiss and D. R. Hamann, *Phys. Rev. B* **38**, 5012 (1988).
- [38] M. S. Hybertsen and L. F. Mattheiss, *Phys. Rev. Lett.* **60**, 1661 (1988).
- [39] L. P. Chan, D. R. Harshman, K. G. Lynn, S. Massidda, and D. B. Mitzi, *Phys. Rev. Lett.* **67**, 1350 (1991).
- [40] H. Lin, S. Sahrakorpi, R. S. Markiewicz, and A. Bansil, *Phys. Rev. Lett.* **96**, 097001 (2006).
- [41] Y. He, T. S. Nunner, P. J. Hirschfeld, and H.-P. Cheng, *Phys. Rev. Lett.* **96**, 197002 (2006).
- [42] Y. He, S. Graser, P. J. Hirschfeld, and H.-P. Cheng, *Phys. Rev. B* **77**, 220507(R) (2008).
- [43] K. Foyevtsova, H. C. Kandpal, H. O. Jeschke, S. Graser, H.-P. Cheng, R. Valentí, and P. J. Hirschfeld, *Phys. Rev. B* **82**, 054514 (2010).
- [44] J. Camargo-Martínez, D. Martínez-Pieschacón, and R. Baquero, *Physica C* **535**, 34 (2017).
- [45] T. Jarlborg, *Adv. Condens. Matter Phys.* **2010**, 912067 (2009).
- [46] V. I. Anisimov, J. Zaanen, and O. K. Andersen, *Phys. Rev. B* **44**, 943 (1991).
- [47] C. Weber, *Sci. Bull.* **62**, 102 (2017).
- [48] J. Sun, A. Ruzsinszky, and J. P. Perdew, *Phys. Rev. Lett.* **115**, 036402 (2015).
- [49] C. Lane, J. W. Furness, I. G. Buda, Y. Zhang, R. S. Markiewicz, B. Barbiellini, J. Sun, and A. Bansil, *Phys. Rev. B* **98**, 125140 (2018).
- [50] J. W. Furness, Y. Zhang, C. Lane, I. G. Buda, B. Barbiellini, R. S. Markiewicz, A. Bansil, and J. Sun, *Commun. Phys.* **1**, 11 (2018).
- [51] K. Pokharel, C. Lane, J. W. Furness, R. Zhang, J. Ning, B. Barbiellini, R. S. Markiewicz, Y. Zhang, A. Bansil, and J. Sun, *arXiv:2004.08047* (2020).
- [52] Y. Zhang, C. Lane, J. W. Furness, B. Barbiellini, J. P. Perdew, R. S. Markiewicz, A. Bansil, and J. Sun, *Proc. Natl. Acad. Sci. USA* **117**, 68 (2020).
- [53] T. Das, R. Markiewicz, and A. Bansil, *Adv. Phys.* **63**, 151 (2014).
- [54] J. Varignon, M. Bibes, and A. Zunger, *Phys. Rev. B* **100**, 035119 (2019).
- [55] Y. Zhang, J. Furness, R. Zhang, Z. Wang, A. Zunger, and J. Sun, *arXiv:1906.06467* (2019).
- [56] H. Hafiz, K. Suzuki, B. Barbiellini, Y. Orikasa, S. Kaprzyk, N. Tsuji, K. Yamamoto, A. Terasaka, K. Hoshi, Y. Uchimoto, Y. Sakurai, H. Sakurai, and A. Bansil, *Phys. Rev. B* **100**, 205104 (2019).
- [57] J. Sun, R. C. Remsing, Y. Zhang, Z. Sun, A. Ruzsinszky, H. Peng, Z. Yang, A. Paul, U. Waghmare, X. Wu, M. L. Klein, and J. P. Perdew, *Nat. Chem.* **8**, 831 (2016).
- [58] R. Car, *Nat. Chem.* **8**, 820 (2016).

- [59] I. G. Buda, C. Lane, B. Barbiellini, A. Ruzsinszky, J. Sun, and A. Bansil, *Sci. Rep.* **7**, 44766 (2017).
- [60] E. B. Isaacs and C. Wolverton, *Phys. Rev. Mater.* **2**, 063801 (2018).
- [61] Y. Zhang, D. A. Kitchaev, J. Yang, T. Chen, S. T. Dacek, R. A. Sarmiento-Pérez, M. A. L. Marques, H. Peng, G. Ceder, J. P. Perdew, and J. Sun, *Npj Comput. Mater.* **4**, 9 (2018).
- [62] C. Lane, Y. Zhang, J. W. Furness, R. S. Markiewicz, B. Barbiellini, J. Sun, and A. Bansil, *Phys. Rev. B* **101**, 155110 (2020).
- [63] Y. Fu and D. J. Singh, *Phys. Rev. Lett.* **121**, 207201 (2018).
- [64] F. Tran, G. Baudesson, J. Carrete, G. K. H. Madsen, P. Blaha, K. Schwarz, and D. J. Singh, *arXiv:2004.04543* (2020).
- [65] J. W. Furness and J. Sun, *Phys. Rev. B* **99**, 041119(R) (2019).
- [66] D. Mejía-Rodríguez and S. B. Trickey, *Phys. Rev. B* **100**, 041113(R) (2019).
- [67] A. Pulkkinen, B. Barbiellini, J. Nokelainen, V. Sokolovskiy, D. Baigutlin, O. Miroshkina, M. Zagrebin, V. Buchelnikov, C. Lane, R. S. Markiewicz, A. Bansil, J. Sun, K. Pussi, and E. Lähderanta, *Phys. Rev. B* **101**, 075115 (2020).
- [68] M. Guarise, B. D. Piazza, H. Berger, E. Giannini, T. Schmitt, H. M. Rønnow, G. A. Sawatzky, J. van den Brink, D. Altenfeld, I. Eremin, and M. Griioni, *Nat. Commun.* **5**, 5760 (2014).
- [69] Y. Y. Peng, M. Salluzzo, X. Sun, A. Ponti, D. Betto, A. M. Ferretti, F. Fumagalli, K. Kummer, M. Le Tacon, X. J. Zhou, N. B. Brookes, L. Braicovich, and G. Ghiringhelli, *Phys. Rev. B* **94**, 184511 (2016).
- [70] Y. Y. Peng, G. Dellea, M. Minola, M. Conni, A. Amorese, D. Di Castro, G. M. De Luca, K. Kummer, M. Salluzzo, X. Sun, X. J. Zhou, G. Balestrino, M. Le Tacon, B. Keimer, L. Braicovich, N. B. Brookes, and G. Ghiringhelli, *Nat. Phys.* **13**, 1201 (2017).
- [71] Y. Y. Peng, E. W. Huang, R. Fumagalli, M. Minola, Y. Wang, X. Sun, Y. Ding, K. Kummer, X. J. Zhou, N. B. Brookes, B. Moritz, L. Braicovich, T. P. Devereaux, and G. Ghiringhelli, *Phys. Rev. B* **98**, 144507 (2018).
- [72] K. Kurashima, T. Adachi, K. M. Suzuki, Y. Fukunaga, T. Kawamata, T. Noji, H. Miyasaka, I. Watanabe, M. Miyazaki, A. Koda, R. Kadono, and Y. Koike, *Phys. Rev. Lett.* **121**, 057002 (2018).
- [73] P. E. Blöchl, *Phys. Rev. B* **50**, 17953 (1994).
- [74] G. Kresse and D. Joubert, *Phys. Rev. B* **59**, 1758 (1999).
- [75] G. Kresse and J. Furthmüller, *Comput. Mater. Sci.* **6**, 15 (1996).
- [76] G. Kresse and J. Furthmüller, *Phys. Rev. B* **54**, 11169 (1996).
- [77] W. Kohn, *Rev. Mod. Phys.* **71**, 1253 (1999).
- [78] J. P. Perdew, K. Burke, and M. Ernzerhof, *Phys. Rev. Lett.* **77**, 3865 (1996).
- [79] P. B. Allen, T. Berlijn, D. A. Casavant, and J. M. Soler, *Phys. Rev. B* **87**, 085322 (2013).
- [80] P. V. C. Medeiros, S. Stafström, and J. Björk, *Phys. Rev. B* **89**, 041407(R) (2014).
- [81] U. Herath, P. Tavazde, X. He, E. Bousquet, S. Singh, F. Muñoz, and A. H. Romero, *Comput. Phys. Commun.* **251**, 107080 (2020).
- [82] S. P. Ong, W. D. Richards, A. Jain, G. Hautier, M. Kocher, S. Cholia, D. Gunter, V. L. Chevrier, K. A. Persson, and G. Ceder, *Comput. Mater. Sci.* **68**, 314 (2013).
- [83] E. Dagotto, *Science* **309**, 257 (2005).
- [84] N. Poccia, G. Campi, M. Fratini, A. Ricci, N. L. Saini, and A. Bianconi, *Phys. Rev. B* **84**, 100504(R) (2011).
- [85] L. Jing, Z. Lin, G. Qiang, A. Ping, Z. Lu, X. Tao, H. Jian-Wei, D. Ying, H. Cheng, Y. Hong-Tao, S. Chun-Yao, X. Yu, L. Cong, C. Yong-Qing, R. Hong-Tao, W. Ding-Song, L. Guo-Dong, W. Qing-Yan, H. Yuan, Z. Feng-Feng, Y. Feng, P. Qin-Jun, L. Shi-Liang, Y. Huai-Xin, L. Jian-Qi, X. Zu-Yan, and X.-J. Zhou, *Chin. Phys. B* **28**, 077403 (2019).
- [86] C. Zou, Z. Hao, H. Li, X. Li, S. Ye, L. Yu, C. Lin, and Y. Wang, *Phys. Rev. Lett.* **124**, 047003 (2020).
- [87] We are not aware of experimental lattice parameters for a freestanding BiO bilayer in the literature.
- [88] W. Fan and Z. Zeng, *Supercond. Sci. Technol.* **24**, 105007 (2011).
- [89] I. Zeljkovic, E. J. Main, T. L. Williams, M. C. Boyer, K. Chatterjee, W. D. Wise, Y. Yin, M. Zech, A. Pivonka, T. Kondo, T. Takeuchi, H. Ikuta, J. Wen, Z. Xu, G. D. Gu, E. W. Hudson, and J. E. Hoffman, *Nat. Mater.* **11**, 585 (2012).
- [90] We studied the  $k_z$  dispersion of the electronic structure by looking along the  $(0, 0, 0) - (0, 0, \frac{\pi}{2})$  and  $(\frac{\pi}{2}, \frac{\pi}{2}, 0) - (\frac{\pi}{2}, \frac{\pi}{2}, \frac{\pi}{2})$  paths in the AFM BZ and we found no significant dispersion.
- [91] In the supercell BZ this point corresponds to the  $X$ -point, and the primitive cell  $X$ -point corresponds to the supercell  $M$  point.
- [92] S. W. Jang, H. Sakakibara, H. Kino, T. Kotani, K. Kuroki, and M. J. Han, *Sci. Rep.* **6**, 33397 (2016).
- [93] S.-L. Yang, J. A. Sobota, Y. He, Y. Wang, D. Leuenberger, H. Soifer, M. Hashimoto, D. H. Lu, H. Eisaki, B. Moritz, T. P. Devereaux, P. S. Kirchmann, and Z.-X. Shen, *Phys. Rev. B* **96**, 245112 (2017).
- [94] A. Moudden, L. Vasiliiu-Doloc, N. Blanchard, G. Collin, and J. Hammann, *Physica C* **235–240**, 1621 (1994).
- [95] V. P. S. Awana, L. Menon, and S. K. Malik, *Phys. Rev. B* **51**, 9379 (1995).
- [96] See Supplementary Material at <http://link.aps.org/supplemental/10.1103/PhysRevB.101.214523> for comparison of Bi2201 with Bi2212 both in the article and in the online description?
- [97] K. Imai, I. Nakai, T. Kawashima, S. Sueno, and A. Ono, *Jpn. J. Appl. Phys.* **27**, L1661 (1988).
- [98] I. Suominen, J. Nieminen, R. S. Markiewicz, and A. Bansil, *Phys. Rev. B* **84**, 014528 (2011).
- [99] A. Kopp, A. Ghosal, and S. Chakravarty, *Proc. Natl. Acad. Sci. USA* **104**, 6123 (2007).
- [100] B. Barbiellini and T. Jarlborg, *Phys. Rev. Lett.* **101**, 157002 (2008).
- [101] L. Sutton, *Tables of Interatomic Distances and Configuration in Molecules and Ions* (The Chemical Society, London, 1958).
- [102] L. Deng, Y. Zheng, Z. Wu, S. Huyan, H.-C. Wu, Y. Nie, K. Cho, and C.-W. Chu, *Proc. Natl. Acad. Sci. USA* **116**, 2004 (2019).

## ACTA UNIVERSITATIS LAPPEENRANTAENSIS

881. RAHIKAINEN, JARKKO. On the dynamic simulation of coupled multibody and hydraulic systems for real-time applications. 2019. Diss.
882. ALAPERÄ, ILARI. Grid support by battery energy storage system secondary applications. 2019. Diss.
883. TYKKYLÄINEN, SAILA. Growth for the common good? Social enterprises' growth process. 2019. Diss.
884. TUOMISALO, TEEMU. Learning and entrepreneurial opportunity development within a Finnish telecommunication International Venture. 2019. Diss.
885. OYEDEJI, SHOLA. Software sustainability by design. 2019. Diss.
886. HUTTUNEN, MANU. Optimizing the specific energy consumption of vacuum filtration. 2019. Diss.
887. LIIKANEN, MIIA. Identifying the influence of an operational environment on environmental impacts of waste management. 2019. Diss.
888. RANTALA, TERO. Operational level performance measurement in university-industry collaboration. 2019. Diss.
889. LAUKKANEN, MINTTU. Sustainable business models for advancing system-level sustainability. 2019. Diss.
890. LOHRMANN, CHRISTOPH. Heuristic similarity- and distance-based supervised feature selection methods. 2019. Diss.
891. ABDULLAH, UMMI. Novel methods for assessing and improving usability of a remote-operated off-road vehicle interface. 2019. Diss.
892. PÖLLÄNEN, ILKKA. The efficiency and damage control of a recovery boiler. 2019. Diss.
893. HEKMATMANESH, AMIN. Investigation of EEG signal processing for rehabilitation robot control. 2019. Diss.
894. HARMOKIVI-SALORANTA, PAULA. Käyttäjät liikuntapalvelujen kehittäjinä - Käyttäjälähtöisessä palveluinnovaatioprosessissa käyttäjien tuottama tieto tutkimuksen kohteena. 2020. Diss.
895. BERGMAN, JUKKA-PEKKA. Managerial cognitive structures, strategy frames, collective strategy frame and their implications for the firms. 2020. Diss.
896. POLUEKTOV, ANTON. Application of software-defined radio for power-line-communication-based monitoring. 2020. Diss.
897. JÄRVISALO, HEIKKI. Applicability of GaN high electron mobility transistors in a high-speed drive system. 2020. Diss.
898. KOPONEN, JOONAS. Energy efficient hydrogen production by water electrolysis. 2020. Diss.
899. MAMELKINA, MARIA. Treatment of mining waters by electrocoagulation. 2020. Diss.
900. AMBAT, INDU. Application of diverse feedstocks for biodiesel production using catalytic technology. 2020. Diss.

901. LAAPIO-RAPI, EMILIA. Sairaanhoidajien rajatun lääkkeenmääräämistoiminnan tuottavuuden, tehokkuuden ja kustannusvaikuttavuuden arviointi perusterveydenhuollon avohoidon palveluprosessissa. 2020. Diss.
902. DI, CHONG. Modeling and analysis of a high-speed solid-rotor induction machine. 2020. Diss.
903. AROLA, KIMMO. Enhanced micropollutant removal and nutrient recovery in municipal wastewater treatment. 2020. Diss.
904. RAHIMPOUR GOLROUDBARY, SAEED. Sustainable recycling of critical materials. 2020. Diss.
905. BURGOS CASTILLO, RUTELY CONCEPCION. Fenton chemistry beyond remediating wastewater and producing cleaner water. 2020. Diss.
906. JOHN, MIIA. Separation efficiencies of freeze crystallization in wastewater purification. 2020. Diss.
907. VUOJOLAINEN, JOUNI. Identification of magnetically levitated machines. 2020. Diss.
908. KC, RAGHU. The role of efficient forest biomass logistics on optimisation of environmental sustainability of bioenergy. 2020. Diss.
909. NEISI, NEDA. Dynamic and thermal modeling of touch-down bearings considering bearing non-idealities. 2020. Diss.
910. YAN, FANGPING. The deposition and light absorption property of carbonaceous matter in the Himalayas and Tibetan Plateau. 2020. Diss.
911. NJOCK BAYOCK, FRANCOIS MITERAND. Thermal analysis of dissimilar weld joints of high-strength and ultra-high-strength steels. 2020. Diss.
912. KINNUNEN, SINI-KAISU. Modelling the value of fleet data in the ecosystems of asset management. 2020. Diss.
913. MUSIKKA, TATU. Usability and limitations of behavioural component models in IGBT short-circuit modelling. 2020. Diss.
914. SHNAI, IULIJA. The technology of flipped classroom: assessments, resources and systematic design. 2020. Diss.
915. SAFAEI, ZAHRA. Application of differential ion mobility spectrometry for detection of water pollutants. 2020. Diss.
916. FILIMONOV, ROMAN. Computational fluid dynamics as a tool for process engineering. 2020. Diss.
917. VIRTANEN, TIINA. Real-time monitoring of membrane fouling caused by phenolic compounds. 2020. Diss.
918. AZZUNI, ABDELRAHMAN. Energy security evaluation for the present and the future on a global level. 2020. Diss.





ISBN 978-952-335-545-3  
ISBN 978-952-335-546-0 (PDF)  
ISSN-L 1456-4491  
ISSN 1456-4491  
Lappeenranta 2020